An Investigation of Iron Concentration Effects and Modelling of Flow Accelerated Corrosion

by

Michael Alexander Briggs

Master of Science in Civil Engineering
University of New Brunswick, 2006
Bachelor of Science in Civil Engineering
University of New Brunswick, 2002

A DISSERTATION SUBMITTED IN PARTIAL FULFILLMENT OF THE REQUIREMENTS FOR THE DEGREE OF

Doctor of Philosophy

In the Graduate Academic Unit of Chemical Engineering

Supervisor(s):	Derek H. Lister, PhD, Chemical Engineering
Examining Board:	William Cook, PhD, Chemical Engineering, Chair
	Huining Xiao, PhD, Chemical Engineering
	Gilles Villemure, PhD, Chemistry
External Examiner:	Paul Spekkens, PhD, Burlington, Ontario

This dissertation is accepted

Dean of Graduate Studies

THE UNIVERSITY OF NEW BRUNSWICK

May, 2017

©Michael Alexander Briggs, 2017

Abstract

Flow accelerated corrosion (FAC) is an aggressive form of degradation in power plant piping that leads to substantial wall thinning and sudden failures. An interaction of a complex series of mechanisms, FAC is difficult to detect, requiring predictive tools to identify susceptible components and guide the deployment of mitigating measures.

An experimental investigation has been carried out examining the effect of changes in iron concentration on the rate of FAC. A sampling system and process were developed to measure bulk iron concentration in concert with measured FAC rates in an experimental probe at temperature.

The UNB mechanistic model has been updated to provide an improved response to variations in bulk iron concentration. The model has also been updated to respond more effectively to mass transfer variations in order to model complex geometry and highly turbulent flow.

Acknowledgements

First and foremost, I'd like to thank my beautiful wife, Kate, for her unwavering support and patience during this challenge.

Thank you Derek for trusting me with this work and providing the support, knowledge, and sometimes, the little push needed to get things done.

Andrew Feicht for the outstanding mentoring you provided throughout this work.

A special thanks is necessary to Dr. Khatereh Mohajery, for providing so much support in the coding and model development.

And thanks to Willy Cook, Noel Kippers, Chester Morris, Miranda Jack, Adam Barnett, Adon Briggs, Keith Rollins, Rob Kirouac, Carl Murdock and all the folks at AECL/CRL/CNL (whatever) for all of the support and good times.

And finally, the Electric Power Research Institute for their financial support.

Table of Contents

Abstract ii

Acknowledgments iii

Table of Contents viii

List of Tables ix

List of Figures xiii

Abbreviations xiv

1 Introduction 1

2 Literature Review 5

2.1 Flow-Accelerated Corrosion 5

2.2 FAC Modelling 8

2.2.1 Berge 9

2.2.2 Bignold 10

2.2.3 Sanchez-Caldera 11

2.2.4 Lister 13
2.2.5 Empirical Models 16
2.2.5.1 Commercial Packages 16
2.2.5.2 Probabilistic Models 17
2.3 Mechanisms of Flow Accelerated Corrosion 18
2.3.1 Oxide Structure 18
2.3.2 Diffusion 21
2.3.3 Solubility 23
2.3.4 Hydrogen 27
2.3.5 Diffusion 28
2.3.6 Flow 31
2.3.7 Mass Transfer 33

3 Experimental **37**

3.1 Loop Experiments Overview 37
3.2 Loop Description 38
3.3 FAC Measurement Probes 43
3.4 Temperature Correlation 47
3.5 Experimental Conditions 53
3.6 Iron Effects 53
3.7 Sampling 56
3.7.1 Apparatus 57
3.7.2 Procedure 60

4 Experimental Results **65**

4.1 Loop Runs 66

4.1.1 Run 1 66

4.1.2 Run 2 69

4.1.3 Run 3 74

4.1.4 Run 4 79

4.1.5 Run 5 79

4.1.6 Runs 6 through 9 83

4.1.7 Run 10 84

5 Model Development **87**

5.1 Oxide Structure 87

5.2 Mass Balances 91

5.2.1 Metal-Passivating Interface 91

5.2.2 Passivating-Oxide Interface 93

5.2.3 Oxide-Solution Interface 94

5.3 Final Equations 95

5.3.1 Mass-Loss Rate 95

5.3.2 Oxide Thickness 96

5.3.3 Spalling 96

5.3.4 Iron Effects 100

5.4 Electrochemistry 101

5.5 Model Computation 111

6 Discussion **113**

7 Conclusions **126**

8 Future Work **129**

8.1 Model Development 129

8.2 Sampling 132

8.3 Commercialization 132

Bibliography **145**

A Appendix A Computational Code **146**

B Appendix B - Model I/O **174**

B.1 Neutral Chemistry, 140°C, 0.5 LPM, No Iron Source, 1.6 mm probe 175

B.2 Neutral Chemistry, 140°C, 0.5 LPM, 25% Iron Source, 1.6 mm probe 178

B.3 Neutral Chemistry, 140°C, 0.5 LPM, 50% Iron Source, 1.6 mm probe 181

B.4 Neutral Chemistry, 140°C, 0.5 LPM, 100% Iron Source, 1.6 mm probe 184

B.5 Neutral Chemistry, 140°C, 0.85 LPM, No Iron Source, 1.6 mm probe 187

B.6 Neutral Chemistry, 140°C, 0.85 LPM, 25% Iron Source, 1.6 mm probe 190
B.7 Neutral Chemistry, 140°C, 0.85 LPM, 50% Iron Source, 1.6 mm probe 193
B.8 Neutral Chemistry, 140°C, 0.85 LPM, 100% Iron Source, 1.6 mm probe 196
B.9 Neutral Chemistry, 200°C, 0.85 LPM, No Iron Source, 1.6 mm probe 199
B.10 Neutral Chemistry, 200°C, 0.5 LPM, No Iron Source, 1.6 mm probe 202
B.11 pH 9.2 Chemistry, 140°C, 0.85 LPM, No Iron Source, 1.6 mm probe 205
B.12 Neutral Chemistry, 140°C, 1.5 LPM, No Iron Source, 1.6 mm probe 208
B.13 Neutral Chemistry, 140°C, 1.65 LPM, No Iron Source, 2.4 mm probe 211
B.14 Neutral Chemistry, 140°C, 1.2 LPM, No Iron Source, 3.2 mm probe 214

C Appendix C - Parametric Study of EPRI Fossil FAC Advisor 217

Vita

List of Tables

2.1 Dissolution rate constant data for Fe_3O_4 with k_m=5-20 mm/s [18] 27

4.1 Experimental Run Summary with Target Conditions 66

4.2 Run 1: Target chemistry conditions 67

4.3 Run 2: Target chemistry conditions 70

4.4 Run 2 results with iron concentration and hydrazine variations 70

4.5 Run 3: Target chemistry conditions 74

4.6 Run 3 results with iron concentration variation and no hydrazine 76

4.7 Run 5 results with iron concentration measured at inlet and outlet of probe 80

4.8 Run 10: Target chemistry conditions 84

4.9 Run 10 results with iron source length variation 85

6.1 Calculated values for modelling iron effect 117

List of Figures

2.1 Relative concentration of ferrous and ferric species in saturated solution at 423 K (150°C)[16] 7

2.2 Relative concentration of ferrous and ferric species in saturated solution at 573 K (300°C)[16] 8

2.3 Experimental and predicted steady-state FAC rates with mass transfer coefficient and varying Cr contents and chemistry conditions [26] 15

2.4 Magnetite solubility in aqueous solution saturated with 799 μmole/kg H_2 [16] 24

2.5 Effect of temperature on erosion-corrosion (FAC) in deoxygenated ammoniated water[40] 25

2.6 Variation of iron diffusivity (Fe^{2+}) in water with temperature calculated with Equation2.21 30

3.1 CNER Loop 1 38

3.2 CNER Loop 1 flow diagram 39

3.3 Loop 1 75L tank 40

3.4 Loop 1 test section 42

3.5 UNB 1.6 mm ID resistance probe installed in the test section . 44
3.6 UNB 1.6 mm ID resistance probe mounted in electrically isolating modified Conax fittings 46
3.7 Example calculation of linear Υ value 51
3.8 Temperature correlation validation results: corrected radius vs. temperature 52
3.9 Iron injection system (right) and measurement probe(left) . . 54
3.10 Run 2 data showing distinct changes in FAC rate with iron source valve-in 55
3.11 Loop 1 sampling system flow diagram 58
3.12 Zirconium autoclaves mounted in laboratory oven. 60
3.13 Extrapolated solubilities of magnetite in water at various conditions 61

4.1 Run 1 probe internal radius vs. time 69
4.2 Run 2 probe internal radius vs. time 71
4.3 Variation of FAC RATE at 140°C, ∼1 ppb O_2, with increase in N_2H_4 from 0 to 100 ppb [5] 72
4.4 Relative FAC rate versus hydrazine concentration for tubular carbon steel specimens exposed to a single-phase flow at 180°C and 235°C at pH25°C = 9.0 [62] 73
4.5 Run 3 probe internal radius vs. time 75

4.6 Run 3 Test 6: probe internal radius vs. time with variation in temperature from 140°C to 200°C 77
4.7 FAC rate vs temperature; Fossil FAC Advisor model vs experimental results 78
4.8 Run 5 Probe internal radius vs. time (Refer to Table 4.7 for test conditions) 81
4.9 Run 10 FAC rate response to varying length of iron injection system (and thus the bulk iron concentration entering the measurement probe). 85

5.1 Assumed oxide structure for FAC mechanistic model [27] . . . 88
5.2 Variation of Cr/Fe ratio through the oxide film formed on 1%Cr-1/2%Mo steel at pH 9.30, 148°C[21] 89
5.3 Bouchacourt model of Cr effect on FAC rate [8] 90
5.4 Ducreux model of Cr effect on FAC. Relative FAC rate vs Cr content of carbon steel at 180°C (single phase) or 175°C (two-phase) at $pH_{25^\circ C} = 9.0$ [63] 90
5.5 Variation of corrosion rate and various hydrodynamic parameters downstream of a flow expansion [65] 99
5.6 Butler-Volmer plot relating electrochemical potential to current 103
5.7 Basic logic diagram for UNB mechanistic model computation . 112

6.1 Predicted FAC rate response to increasing iron concentration as a percentage of saturation concentration 114

6.2 Measured and predicted FAC rates with variations in bulk iron concentration 116
6.3 Sacrificial Iron Loop Section Outlet Diameters 119
6.4 Model output, predicted FAC rate for neutral conditions, 0.5L/min, at 140°C 120
6.5 Model output, predicted oxide thickness for neutral conditions, 0.5L/min, at 140°C 121
6.6 Variation of FAC rate and spalling time constant, k_{sp}, with change in mass transfer coefficient, k_m. Obtained by testing measurement probes of differing diameters (1.6 mm, 2.4 mm and 3.2 mm) 122
6.7 Measured and predicted wall profile due to FAC downstream of a nozzle 123
6.8 Predicted progression of wall thinning downstream of nozzle . 125

C.1 Variation of FAC rate with changes in flow rate 219
C.2 Variation of FAC rate with changes in $[O_2]$ 219
C.3 Variation of FAC rate with changes in temperature 220
C.4 Variation of FAC rate with changes in $pH^{25°C}$ 221
C.5 Variation of FAC rate with changes in chromium content of the steel 222
C.6 Variation of FAC rate with changes to $[N_2H_4]$ 222

Abbreviations

FAC	Flow accelerated corrosion
NACE	National Association of Corrosion Engineers
EPRI	Electric Power Research Institute
UNB	University of New Brunswick
ASTM	American Society for Testing and Materials
RPC	Research and Productivity Council
EDF	Électricité de France
CNER	Centre for Nuclear Energy Research
FFA	Fossil FAC Advisor
EPT	ethylene-propylene terpolymer rubber
psi	pounds per square inch
psig	pounds per square inch gauge
IX	ion exchange
OD	outside diameter
ID	inside diameter
PTFE	polytetrafluoroethylene
ICP-ES	inductively-coupled plasma emission spectroscopy
ICP-MS	inductively-coupled plasma mass spectroscopy
redox	reduction and oxidation

α	geometrical temperature coefficient (disambiguation) [1/mm/°C]
α, β, γ	Sherwood number correlation constants (Equation 2.29)
β	symmetry factor
β	geometrical corrector term (disambiguation) [1/mm]
δ_{OX}	thickness of oxide layer [g/cm^2, a function of oxide density]
δ_P	thickness of passivating layer [g/cm^2, a function of oxide density]
λ^0_- and λ^0_+	the cationic and anionic conductances at infinite dilution [S/equivalent]
μ	dynamic viscosity [cP]
ϕ_{OX}	oxide porosity
ϕ_P	passivating layer porosity
ρ	density [g/cm^3]
ρ	resistivity (disambiguation) [$\mu\Omega$/mm]
ρ_{OX}	density of oxide [g/cm^3]
ρ_P	density of passivating layer [g/cm^3]
ρ_{Fe}	density of iron [g/cm^3]
ϕ	porosity

υ	kinematic viscosity [cm^2/s]
ρ^*	apparent resistivity of the probe [$\mu\Omega$/mm]
τ	shear stress at the pipe wall [N/cm]
ζ_P	tortuosity of the passivating layer
ζ_{OX}	tortuosity of the oxide layer
ΔG	Gibbs energy of formation [kJ/mol]
$\Delta C/\Delta y$	concentration gradient
$a_{oxidized}$ and $a_{reduced}$	activities of species of interest
A	cross sectional area [mm^2]
C_b	bulk iron concentration [g/cm^3]
C^e_{M-P}	solubility at the metal-passivating interface [g/cm^3]
C^e_{P-O}	solubility at the passivating-oxide interface [g/cm^3]
C_{eq}	iron solubility [g/cm^3]
C_{M-P}	concentration of iron at the metal-passivating interface [g/cm^3]
C_{P-O}	concentration of iron at the passivating-oxide interface [g/cm^3]
C_{O-B}	concentration of iron at the oxide-bulk interface [g/cm^3]
C_s	surface iron concentration [g/cm^3]
C^{Sat}_{O-B}	solubility at the oxide-bulk interface [g/cm^3]
d	characteristic length [cm]
d	oxide particle diameter [cm]
$\frac{dm}{dt}$	metal loss rate [g/s]
D	mass diffusivity [cm^2/s]
D_{eff}	effective diffusivity [cm^2/s]
D_{Fe}	diffusivity of iron in water [cm^2/s]
D°_{AB}	diffusivity [cm^2/s]
D_{OX}	diffusivity of iron in water (in the oxide layer) [cm_2/s]
D_P	diffusivity of iron in water (in the passivating layer) [cm_2/s]
E^0	initial end effect [1/mm]
E_0	standard potential of the reaction [V]
E_{eq}	equilibrium potential of the reaction [V]
E_A and E_C	reaction potentials at anode and cathode [V]
E_{mixed}	mixed potential at interface [V]
F^*	surface area factor = 1.732
F	Faraday constant = 96485 [C/mol]
i	current of reaction [A]

i_0	exchange current [A]
J	diffusional mass flux [g/s-cm^2]
k_d	dissolution rate constant [cm/s]
k_m	mass transfer coefficient [cm/s]
k_{sp}	spalling time factor
L	monitored length [mm]
m	amount of iron corroded per unit area [g/cm^3]
MW	molecular weight of species of interest [g/mol]
$\frac{M_{Fe}}{M_P}$	mass fraction of iron in the passivating layer
n	number of electrons passed in the reaction
Nu	Nusselt number
Pr	Prandtl number
R	Universal Gas Constant = 8.314 [J/mol*K]
R	resistance (disambiguation for temperature correlation) [$\mu\Omega$]
Re	Reynolds number
R_d	oxide dissolution rate
R_m	mass transfer rate
R_{metal}	metal loss rate
S	super-saturation factor = 1.1
U	linear velocity of the fluid [cm/s]
z_+ and z_-	the cationic and anionic valencies
Sc	Schmidt number
Sh	Sherwood number
t_{sp}	spalling time [s]
T	temperature [°C] or [K]

Chapter 1

Introduction

Corrosion as a material degradation mechanism has a massive financial impact. Dated studies such as those completed by NACE in 2002 [1] estimate the annual cost of corrosion in the United states to be on the order of $276 billion, and an EPRI study from the same time period [2] pins the direct cost to the power production industry at approximately $17 billion. More recent anecdotal reports [3] place the figure at around $1.1 trillion for 2016 across all industries.

The conditions within the process piping systems of electricity generating stations bring with them a wide variety of component degradation mechanisms. While many are well understood and comprehensive mitigating strategies exist, excessive wear and component failures still occur.

One of the most aggressive forms of degradation is flow-accelerated corrosion (FAC). FAC occurs in both single- and two-phase water systems and is defined as a rapid wall thinning resulting from a loss of the protective oxide formed on the base metal surface. The mechanisms influencing the occurrence of FAC are generally well known, namely the solubility of magnetite, diffusion of corrosion products and mass transfer, which are described in numerous references, [4],[5],[6],[7],[8],[9],[10],[11] yet FAC remains a major problem in fossil and nuclear power plants [8]. In fossil combined cycle plants, FAC is recognized as the primary failure mechanism in the heat recovery steam generators (HRSG) [12]. Methods for controlling FAC with appropriate system chemistry or by material selection are widely employed [13],[8], but not entirely successful. Unfortunately, detection of FAC can be troublesome, and the problem often is not identified until a failure has occurred.

A fundamental rate determining mechanism of FAC is the chemical driving force that exists when the flowing coolant is undersaturated in dissolved iron species. This work focused on an experimental program to generate data to support the relations assumed between bulk iron concentration in the flowing fluid and the FAC rate. An experimental recirculating water loop was employed to obtain real-time measurements of FAC rate in a test probe with changes in bulk iron concentration. Test conditions covered a variety of secondary side chemistry conditions seen in the fossil industry, where many

FAC failures still occur [13].

A corrosion product sampling system was developed to further support the influence of dissolved iron on FAC. Apparatus and procedures to collect system fluid at temperature for analysis were designed to obtain more accurate measures of iron concentration in the coolant while measuring FAC rate during the collection of the sample. With further development, this system could be adapted to an operating plant, providing more realistic corrosion product measurements than the current industry best practice.

This study also revisits the mechanistic model developed by the University of New Brunswick Nuclear Research Group. The model equations were re-derived to more accurately represent the mass balances of the proposed oxide structure. Modifications to the model were made to more effectively account for mass transfer variations within a turbulent flow regime, and calculations of surface iron concentration were adjusted to provide an overall better fit to experimental data. The spalling effect, unique to the UNB model, was related to variations in mass transfer in a base case, and this relation was successfully applied to another, more complex analysis case. Adjustments were also carried out to the electrochemistry calculations in the model to consider the diffusion of hydrogen generated by the corrosion reaction back through the steel wall, rather than diffusion outward through the oxide layer.

The predictive capabilities of the model presented should allow for systems of

any geometry to be assessed with the appropriate inputs from computational fluid dynamic analysis. This would allow power plant operators to conduct FAC analyses on systems that were previously impossible to investigate.

Chapter 2

Literature Review

2.1 Flow-Accelerated Corrosion

The underlying process of FAC is the corrosion of metal occurring at the wetted surface of the component of interest. The corrosion of metal is a chemical process, characterized by a reduction-oxidation (redox) reaction. In the case of FAC, it is the oxidation of iron from the carbon steel piping. FAC normally occurs under reducing chemistry conditions in deoxygenated water, assuming that the water diffuses through the oxide to reach the metal surface.

The corrosion of iron is described by a reduction-oxidation reaction occurring

at the metal surface: The oxidation reaction of Fe occurring at the anode is:

$$Fe \rightarrow Fe^{2+} + 2e^{-} \tag{2.1}$$

The corresponding cathodic reaction to Equation 2.1 is the reduction of hydrogen:

$$2H^{+} + 2e^{-} \rightarrow H_2 \tag{2.2}$$

The H_2 produced in Equation 2.2 either diffuses into the base metal or toward the oxide-solution interface. An inner oxide layer is formed at the metal surface consuming ~50% of the Fe^{2+} from Equation 2.1 ([14],[15]) to form Fe_3O_4 per the generalized reaction:

$$3Fe^{2+} + 4H_2O \rightarrow Fe_3O_4 + 6H^{+} + H_2 \tag{2.3}$$

At the conditions of this study, much of the remaining Fe^{2+} is assumed to form aqueous ferrous hydroxide at the metal-oxide interface per the following reaction:

$$Fe^{2+} + 2H_2O \rightarrow Fe(OH)_2 + 2H^{+} \tag{2.4}$$

This diffuses through the oxide layer and is carried to the bulk coolant. Under FAC conditions where the bulk coolant is undersaturated with iron, magnetite precipitation from the coolant does not occur, thus a porous outer oxide layer does not form. Instead, the dissolution of the fine grained layer of magnetite against the steel surface must be considered, following Equation

2.5[14] (at neutral or elevated pH).

$$Fe_3O_4 + 8H^+ + 2e^- \rightarrow 3Fe^{2+} + 4H_2O \tag{2.5}$$

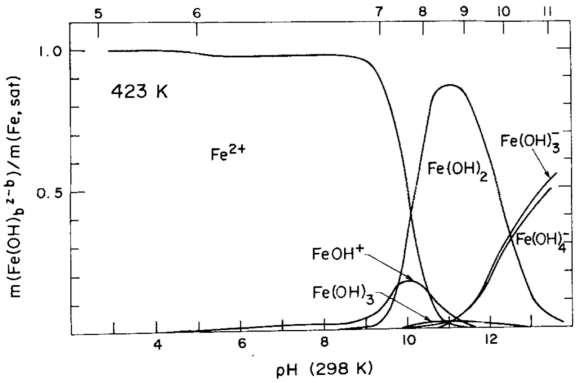

Figure 2.1: Relative concentration of ferrous and ferric species in saturated solution at 423 K (150°C)[16]

Depending on the conditions (pH and temperature), different soluble species will be present shown in Figures 2.1 and 2.2. As can be seen from both Figures 2.1 and 2.2 at the temperatures and pH typical of power plant systems (around 140°C to 300°C and $pH_{25^\circ C}$ from about 7 to 10), the dominant species of iron in solution is either Fe^{2+} at pH 7 or $Fe(OH)_2$ at pH 10. It should be noted that reactions involving ferric species (Fe^{3+}) are omitted, as they are assumed to account for only 10% of the total iron species involved in the process [17] at the conditions considered in this work. At higher pH solutions, ferric species become increasingly important in the analysis [18]. Also

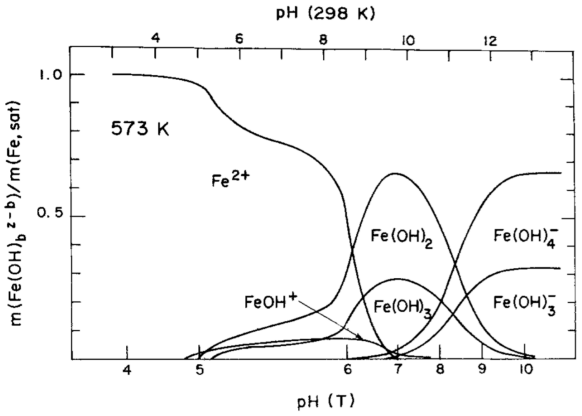

Figure 2.2: Relative concentration of ferrous and ferric species in saturated solution at 573 K (300°C)[16]

to be considered is the lower ferrous hydrolysis stability compared to that of ferric species [19], leading to the formation of magnetite being dependent only on the ferrous species in solution in normal feedwater conditions.

2.2 FAC Modelling

The capability to predict FAC mechanistically has been pursued for decades. Some of the earliest models proposed by Berge [20] and Bignold[21] laid the groundwork for the development of more complex mechanistic models offering substantial improvements on the predictive capabilities as the understanding of the mechanisms was refined. In contrast to the mechanistic approach to predicting FAC, other work has been done to develop empirical relations, using vast troves of data to draw correlations that might permit predictions

to be made.

2.2.1 Berge

In 1980, Berge et al [20] presented a mechanistic model to determine the rate of FAC. The model shown in Equation 2.6, while similar in concept to Equation 2.7 by Bignold, has often been adopted as the fundamental FAC rate equation for many predictions, with a concentration driving force for the corrosion reaction being resisted by the processes of mass transfer and dissolution kinetics.

$$R = \frac{C_{eq} - C_b}{\frac{0.5}{k_d} + \frac{1}{k_m}} \tag{2.6}$$

Where:

C_{eq} = iron solubility [g/cm^3]

C_b = bulk iron concentration [g/cm^3]

k_d = dissolution rate constant [cm/s]

k_m = mass transfer coefficient [cm/s]

The 0.5 term associated with the dissolution kinetics accounts for the assumption that approximately half of the corroded iron species precipitate as Fe_3O_4 at the metal surface while the remainder diffuse towards the coolant.

This model is accounting for system chemistry conditions within the solubility of the oxide layer. Note that the model only accounts for mass transfer of soluble iron species from the surface of the oxide, and does not account

for any flow induced mechanical degradation of the oxide layer.

2.2.2 Bignold

Bignold et al [9] presented a mechanistic approach to modelling FAC in 1983. This model is given by Equation 2.7 below, where the metal loss rate, R_{metal} is equal to the sum of the mass transfer rate, R_m and the kinetic rate of oxide dissolution, R_d.

$$\frac{1}{R_{metal}} = \frac{1}{R_m} + \frac{1}{R_d} \tag{2.7}$$

The model assumes that either mass transfer or dissolution will be the controlling process depending on the operating conditions. If a particular process is considered to be controlling, the metal loss rate can be reduced to a simple form as the other process will have little effect. For example, if mass transfer were controlling, the overall rate, R_{metal}, would be equal to the mass transfer coefficient, k_m, multiplied by the difference in iron concentration between the surface, C_s, and the bulk coolant, C_b, as the rate of diffusion, R_d, would be sufficiently great in the denominator to make the $1/R_d$ term insignificant to the combined rate R_{metal}.

$$R_{metal} = k_m(C_s - C_b) \tag{2.8}$$

It was assumed in the presentation of this model that the temperature di-

rectly influenced the controlling nature of either process, with mass transfer controlling above 130°C due to the increased kinetics of dissolution at elevated temperature, and conversely with dissolution controlling below 130°C as mass transfer would be the faster process in that range.

Many of the conditions considered by the model are accounted for in terms of the solubility of magnetite, and thus the calculation of the C_s term in Equation 2.8. Variables such as temperature, pH, hydrogen concentration and electrochemical effects all influence the oxide solubility.

2.2.3 Sanchez-Caldera

Building upon the foundation of the Berge model, Sanchez-Caldera [22] expanded the model's capabilities, as presented in Equation 2.9, to include effects of oxide morphology as a diffusional resistance to the transfer of ionic and soluble iron species from the surface of the metal to the oxide-solution interface.

$$\frac{dm}{dt} = \frac{\phi(C_{eq} - C_b)}{\frac{1}{k} + (1-f)\left(\frac{1}{k_m} + \frac{\delta_{ox}}{D_{Fe}}\right)} \tag{2.9}$$

Where:

ϕ_{OX} = oxide porosity

C_{eq} = iron solubility [g/cm^3]

C_b = bulk iron concentration [g/cm^3]

k = reaction rate constant [cm/s]

f = fraction of Fe converted to Fe_3O_4 at the M-O interface

k_m = mass transfer coefficient [cm/s]

δ_{OX} = thickness of oxide layer [g/cm^2]

D_{Fe} = diffusivity of iron in water [cm^2/s]

Noting that previous models (Berge and Bignold) were lacking in their presentation of essential variables required for benchmarking, as well as having been validated against complex geometry (bends, orifices and impinging jets, for example), this model was validated against straight, cylindrical specimens placed in the EDF Cicero loop in an attempt to relate fluid effects to reaction kinetics.

Experimental verification of this model revealed that wear rate was independent of velocity (dissolution controlled), yet the model had a strong dependence on oxide porosity (a mass transfer effect).

The Sanchez-Caldera model was revisited soon after by Bouchacourt [23] who assumed that FAC rate was proportional to mass transfer. Laboratory experiments were conducted that seemed to imply that oxide thickness had no effect on FAC rates, and that overall, reaction kinetics (oxide dissolution) would not be controlling, resulting in the simplified Equation 2.10.

$$\frac{dm}{dt} = 2k_m\phi_{OX}(C_{eq} - C_b) \tag{2.10}$$

This is not in agreement with the findings of Sanchez-Caldera, who indicated that kinetics would be controlling, but the current EDF software BRT-Cicero makes use of a version of the original Sanchez-Caldera equation, which is widely used throughout the French nuclear fleet [24].

2.2.4 Lister

In response to the discovery of advanced FAC occurring in the feeder piping at the Point Lepreau Nuclear Generating Station, Lister and Lang [25] presented a comprehensive mechanistic model based on mass transfer, dissolution and diffusion through the oxide layer. Additionally, the model incorporates the electrochemical behaviour at each interface to adjust critical parameters with each iteration of the calculations.

The model was applied to the primary heat transport system of the CANDU 6 Nuclear Reactor system at Point Lepreau, and was able to successfully predict oxide thickness and corrosion rate for a variety of coolant flow velocities under lithiated conditions.

Equation 2.11 presents the updated version of the Lister-Lang model as described by Phromwong [27]. This model expands on the previous version by incorporating terms to account for material composition, namely chromium content of the steel. Modelling results are presented in Figure 2.3 showing

reasonable results against experimental measurements.

$$\frac{dm}{dt} = \frac{S\left(C^e_{M-P} - C^e_{P-O}\right) - \frac{k_d F^* S C^e_{O-B} + k C_b}{k_d F^* + k_m}}{\frac{\delta_P \zeta_P}{\phi_P D_P \rho_P (1-\phi_P)} - \left[\left(\frac{M_{Fe}}{M_P}\right)\frac{\delta_P \zeta_P}{\phi_P D_P \rho_{Fe}} + \frac{0.467(1.101+\phi_{OX})\delta_O X \zeta_{OX}}{\phi_{OX} D_{OX} \rho_{OX}(1-\phi_{OX})} + \frac{0.667(1.101+\phi_{OX})}{k_d F^* + k_m}\right]} \tag{2.11}$$

Where:

C^e_{M-P} = solubility at the metal-passivating interface [g/cm^3]

C^e_{P-O} = solubility at the passivating-oxide interface [g/cm^3]

C_{O-B} = concentration of iron at the oxide-bulk interface [g/cm^3]

C_b = bulk iron concentration [g/cm^3]

F^* = surface area factor = 1.732

k_d & k_m = dissolution and mass transfer rate constants [cm/s]

δ_P & δ_{OX} =thickness of passivating and oxide layers [g/cm^2]

ζ_P & ζ_{OX} =tortuosity of the passivating and oxide layers

ϕ_P & ϕ_{OX} = passivating and oxide layer porosity

$\frac{M_{Fe}}{M_P}$ = mass fraction of iron in the passivating layer

D_P & D_{OX} = diffusivity of iron in water [cm^2/s]

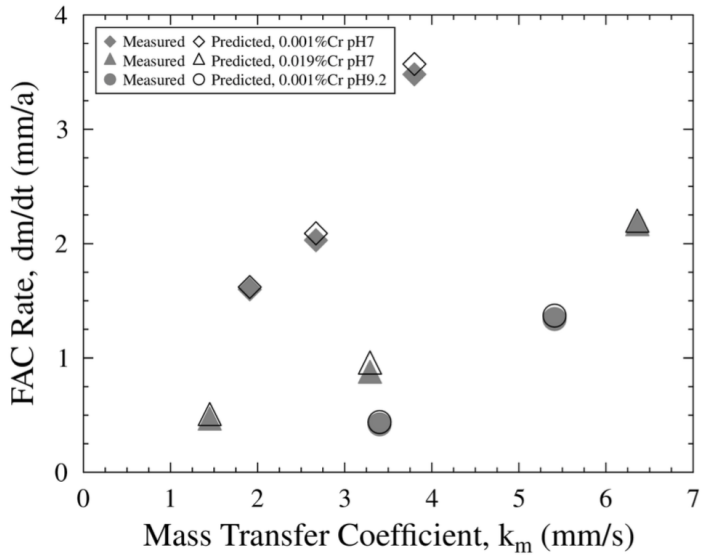

Figure 2.3: Experimental and predicted steady-state FAC rates with mass transfer coefficient and varying Cr contents and chemistry conditions [26]

2.2.5 Empirical Models

2.2.5.1 Commercial Packages

An alternative approach to the mechanistic models presented are the empirical based models that are widely used in industry, particularly the Electric Power Research Institute (EPRI) CHECWORKS algorithm [28]. This algorithm has been developed over many years and integrated into a number of software packages for industrial use.

$$E = F_1(T) * F_2(AC) * F_3(MT) * F_4(O_2) * F_5(pH) * F_6(G) * F_7(\alpha) * F_8(N_2H_4) \tag{2.12}$$

Where:

E = Wastage rate

$F_1(T)$ = Factor for temperature effect

$F_2(AC)$= Factor for alloy content

$F_3(MT)$ = Factor for mass transfer effect

$F_4(O_2)$ = Factor for dissolved oxygen effect

$F_5(pH)$ = Factor for pH effect

$F_6(G)$ = Factor for geometry effect

$F_7(\alpha)$ = Factor for void fraction effect

$F_8(N_2H_4)$ = Factor for hydrazine effect

Empirical relations such as Equation 2.12 rely on massive databases of exper-

imental and plant data. These models take input values of system conditions and geometry and apply factors based on trend-lines plotted through these data.

These models are often applied in industry, but they are not without shortcomings. Generally, these empirical models predict relative rates of wall thinning, meaning they can determine whether one of two components is corroding faster than the other. Until the models are bench-marked with field wall thickness measurements, the results are qualitative in nature only.

As part of this work, an investigation into the effectiveness of the EPRI Fossil FAC Advisor [28] was conducted, and is included in Appendix C. A simulated system was built in the software to represent the UNB experimental loop described in Section 3.2, and results were compared with experimental data to gauge the response of the empirical code to changes in various operating parameters.

2.2.5.2 Probabilistic Models

More recently, researchers have been attempting to predict wall loss due to FAC by means of probabalistic analysis [29], [30], [31], [32]. As in the CHECWORKS code, the statistical modelling relies entirely on databases of field and experimental data to obtain wall thinning rates. Thus, true predictive modelling is limited with these methods.

As Jyrkama [31] points out, reasonable results can produced, but are generally only capable of providing a timeline to replacement, and accurate results are difficult to achieve due to physical challenges with the measurements. The methods are wholly reliant on an individual plant's ability to repeatedly measure precise locations at specified intervals which, due to the variability in the occurrence of FAC at discrete locations on a component, make the predictions difficult to trust for engineering purposes.

2.3 Mechanisms of Flow Accelerated Corrosion

The primary mechanisms associated with determining the rate of flow accelerated corrosion are presented in the following sections.

2.3.1 Oxide Structure

The carbon steel piping of power plant systems is normally overlaid by a double oxide layer described by Potter and Mann [33] that forms when the coolant is saturated with dissolved iron, the inner layer against the steel being fine grained and compact and the outer layer being thicker and more porous. This double oxide layer provides substantial protection to the underlying

metal and after sustained exposure will maintain a fairly constant thickness.

The inner layer is thought to occur from direct conversion of iron corrosion products to magnetite per Equation 2.3, whereas the outer layer is oxidative precipitation of iron from solution per Equation 2.13.

$$3Fe(OH)_2 \rightarrow Fe_3O_4 + H_2 + 2H_2O \tag{2.13}$$

Under FAC conditions (under-saturation of the bulk coolant in iron), the outer layer does not precipitate, leaving only the inner layer to protect the underlying steel. It is assumed that as the metal surface is corroded, the inner layer of oxide forms to immediately fill the volume of base metal corroded [33].

Field [34] confirmed this oxide formation proposed by Potter and Mann, and determined a porosity value in the range of 8% to 15% by way of density measurements of the magnetite. Field also measured inner layer magnetite particle size in the range of 0.025 μm to 0.5μm.

Based on the assumption that the volume of corroded base metal is replaced by an equal volume of oxide (magnetite), the amount of iron that forms the inner oxide layer can be described by Equation 2.15 [35].

$$\text{Amount of iron in inner oxide} = 0.723\frac{\rho_{OX}}{\rho_{FE}}m(1-\phi) \tag{2.14}$$

which reduces to:

$$\text{Amount of iron in inner oxide} = 0.476m(1-\phi) \tag{2.15}$$

Where:

ρ_{OX} = density of oxide [g/cm^3]

ρ_{FE} = density of iron [g/cm^3]

m = amount of iron corroded per unit area [g/cm^3]

ϕ = oxide porosity

The amount of material diffusing outwards (assumed to be ferrous iron and soluble ferrous species) is given by:

$$\text{Amount of iron diffusing outwards} = (1 - 0.723\frac{\rho_{OX}}{\rho_{FE}}(1-\phi))m \tag{2.16}$$

which then reduces to:

$$\text{Amount of iron diffusing outwards} = 0.476m(1.101+\phi) \tag{2.17}$$

These equations will be key in the derivation of the overall model, when defining the mass balances at each interface of the metal, oxide and solution.

2.3.2 Diffusion

Effective transport of ionic and soluble species to and from the surface of the metal through the oxide is considered by some to be the rate limiting step in FAC [36], [37]. While some of the iron produced during the corrosion process directly converts to magnetite at the metal-oxide interface, approximately 50% of the corroded iron diffuses through the oxide via a series of interconnected pores [21]. The presence of these pores was discussed by Bignold [38], and the theory was presented that a diffusion gradient is maintained without pore blockage because the solution of hydrolyzed iron will vary in solubility as it diffuses through pores in the oxide due to variations in the stoichiometry of the oxide across the layer. Robertson [39] suggests that pore blockage by oxide formation within the pore does not occur if the activity of oxygen within the pore equals that of the surrounding oxide.

Employing the pores-solution model characterizes the oxide in terms of thickness, porosity and tortuosity. This characterization will determine the effective path that ionic and soluble species need to traverse from one side of the oxide to the other, driven by a concentration gradient across the oxide. Sanchez-Caldera [22] deduced from experimental relations that the porosity of the oxide will vary with system temperature. As temperature increases, the increased chemical kinetics controlling the formation of the oxide results in a reduced oxide porosity. This effect is not definitively quantified in the literature. Robertson [39] also commented that oxide porosity varies with

system pH.

Robertson [39] and Tomlinson [15] describe an alternative approach to describe the diffusion of various species through the oxide via grain-boundaries. This model assumes that ionic species move along the grain boundaries of the oxide as a result of a gradient of Fe^{2+} ions across the oxide, rather than through interconnected pores via a concentration gradient of aqueous species as described by the pores-solution model. Robertson cites a number of criticisms of the pores-solution model, particularly that the observed pore size is too small to account for the corrosion rates observed if the diffusion is the rate limiting step, and that the diffusion coefficient for aqueous transport through the oxide would be far too low to account for the magnitude of transport necessary.

Robertson's description of the grain boundary diffusion model argues that solid-state diffusion of protons into the oxide is a better fit as opposed to electron transfer across the oxide, which he claims is responsible for the evolution of hydrogen at the oxide-metal boundary. A case is also made for the difficulty of alloying elements, such as nickel and chromium, to diffuse through the inner oxide via the grain boundary model, leading to a concentration of these alloying concentrating within the inner oxide layer at the oxide-metal interface. This is contrary to the experimental findings of Bignold [9], who observed a chromium enrichment of the inner oxide layer, but saw higher ratios of Cr to Fe at the oxide-solution interface, rather than the oxide-metal

interface as was inferred by Robertson.

As a point to consider, the overall diffusion mechanism through the oxide may not be a case of pore-solution or grain boundary or pure solid-state at every condition. It is entirely possible that variations in pH and temperature will alter the oxide morphology to the extent that at certain conditions, a pore-solution model will be valid, yet under other conditions, grain boundary will better represent the diffusion mechanism. To complicate matters further, under some conditions, corrosion products could be diffusing under aqueous conditions via pores, whilst O^{2-} or H^{+} ions could be diffusing inward through the oxide via grain boundary or solid-state diffusion.

Regardless, Robertson's assessment of the two models neglected the electrochemical effects that influence the concentration gradients and local solubilities of the species involved in the process, which would negate the need for the larger diffusion coefficient that Robertson cites [37]. Thus, the current work considers only the pores-solution model for diffusional transport through the oxide layer as has been previously applied by Lang [37] and Phromwong [27].

2.3.3 Solubility

The occurrence of FAC is dependent on the behavior of the oxide layer under the specific conditions in the system, which is influenced by the solubility of the oxide layer in solution. The solubility of the magnetite (and thus the

FAC rate) is very sensitive to coolant pH and temperature (Figure 2.4 and Figure 2.5). Magnetite solubility is at a minimum in the pH range of $\sim$ 9 to 10.5 at 300°C, as can be seen in Figure 2.4, the commonly recommended operating range for power plant heat transport systems to minimize FAC [8].

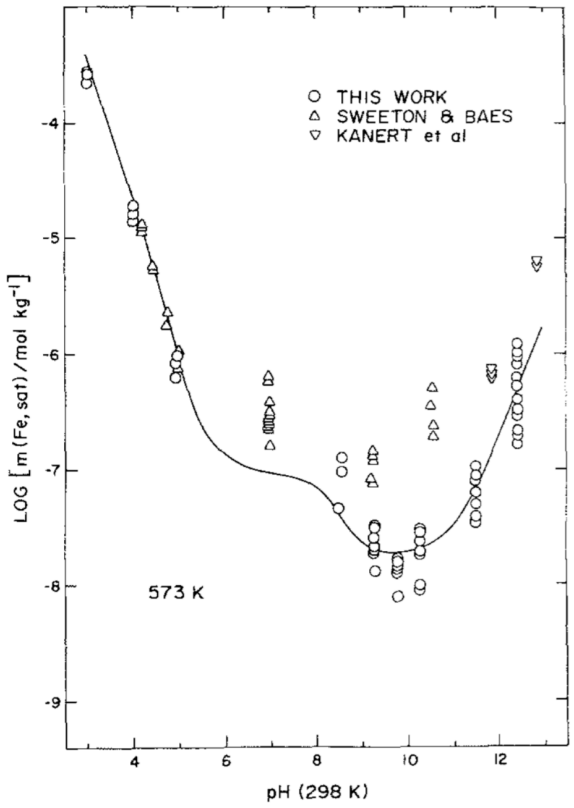

Figure 2.4: Magnetite solubility in aqueous solution saturated with 799 μmole/kg H_2 [16]

In coolant unsaturated in dissolved iron where FAC is occurring, a major con-

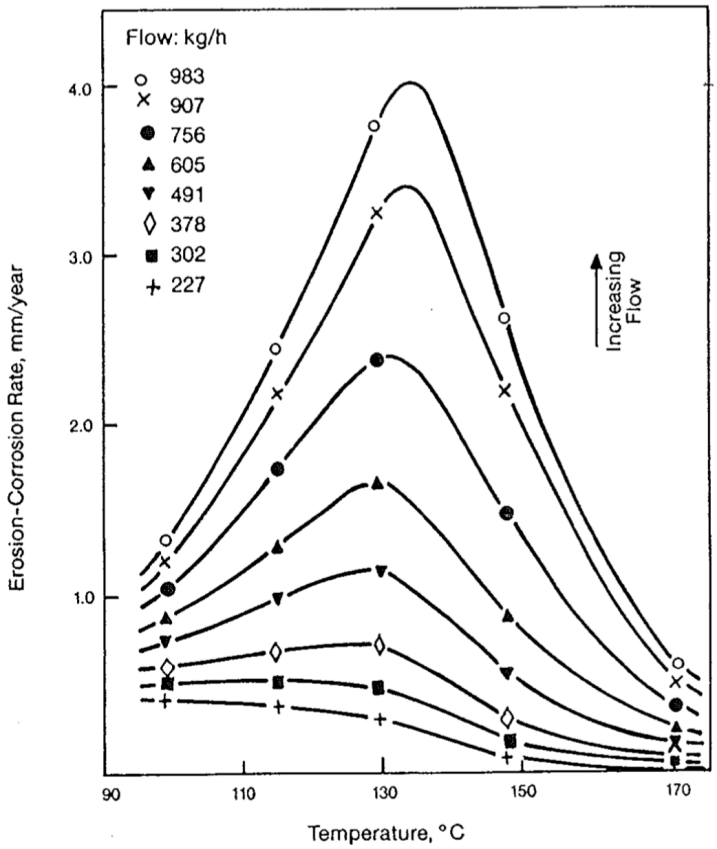

Figure 2.5: Effect of temperature on erosion-corrosion (FAC) in deoxygenated ammoniated water[40]

tributor to the process is oxide dissolution, described by Equation 2.5. The dissolution of the magnetite layer is normally the slower or rate-controlling step of the processes occurring at the oxide-solution interface, that results, at least mathematically, in typical mechanistic models exhibiting little influence of flow on the rate of metal loss.

Equation 2.18 [35] presents the dissolution rate as equal to the dissolution rate constant, k_d, and a surface area factor, F^*, multiplied by the chemical driving force, the difference between the iron saturation concentration, SC_{O-B}^{Sat}, and the surface concentration at the oxide-bulk interface, C_{O-B}.

$$\text{Dissolution Rate} = k_d F^* (SC_{O-B}^{Sat} - C_{O-B}) \tag{2.18}$$

Where:

k_d = dissolution rate constant [cm/s]

F^* = surface area factor = 1.732

S = super-saturation factor = 1.1

C_{O-B}^{Sat} = solubility at the oxide-bulk interface [g/cm^3]

C_{O-B} = concentration of iron at the oxide-bulk interface [g/cm^3]

The dissolution rate constant is an important factor in the predictions of FAC. At typical feedwater temperatures (up to 140°C), and lower pH, dissolution rate is generally higher, leading to the FAC rate being more dependent on mass transfer rate. Alternatively, at higher pH, the dissolution rate is an order of magnitude lower, placing more control of the process on dissolu-

tion kinetics[18]. Recent experiments conducted at UNB by Mohajery [18] present measured dissolution rate constants over a range of primary CANDU and nominal feed-water conditions, shown in Table 2.1.

Temp (°C)	$pH_{25°C}$	k_d(mm/s)
25	7	0.25 ± 0.05
55	7	0.85
140	7	2.20
140	7	2.05
140	$9.2(NH_3)$	0.06
140	$9.2(NH_3)$	0.03
200	$9.2(NH_3)$	0.36
310	$10.5(LiOH)$	0.44 ± 0.22

Table 2.1: Dissolution rate constant data for Fe_3O_4 with k_m=5-20 mm/s [18]

2.3.4 Hydrogen

Under the reducing conditions of deoxygenated water where FAC normally occurs, the influence of hydrogen concentration at each interface is an important consideration. Tomlinson [41] showed that up to 90% of hydrogen produced during high temperature corrosion of steel in deoxygenated water occurs at the metal-oxide interface. The production of hydrogen at the metal-oxide interface is a result of the corroding base metal as well as the direct precipitation of the inner magnetite layer.

Tomlinson [41] and Tremaine and Leblanc [16] indicate that the solubility of the magnetite oxide layer tends to increase with increasing hydrogen con-

centration. This increase in solubility would increase the FAC rate as the driving force for diffusion of corrosion products through the oxide as well as the mass transfer of corrosion products to the bulk coolant would be greater. Berge [42] showed a magnetite solubility dependance of $[H_2]^{1/3}$. Tomlinson [41] showed that high concentrations of hydrogen at the metal-oxide interface increased the corrosion rate by a factor of 3.

2.3.5 Diffusion

As noted previously, the assumption of the pores-solution model is used to describe the movement of soluble and ionic species to and from the metal surface. The diffusional mass flux, J, is defined as in Equation 2.19, with the effective diffusivity D_{eff}, defined by Equation 2.20, Geankopolis [23].

$$J = -D_{eff}\frac{\Delta C}{\Delta y} \tag{2.19}$$

Where:

J = diffusional mass flux [g/s-cm^2]

D_{eff} = effective diffusivity [cm^2/s]

$\Delta C/\Delta y$ = concentration gradient

and:

$$D_{eff} = \frac{D^{\circ}_{AB}\phi}{\zeta} \tag{2.20}$$

Where:

D°_{AB} = diffusivity of A into B [cm^2/s]

ϕ_{OX} = oxide porosity

ζ = tortuosity

The diffusivity is calculated in our application by applying the Nernst equation describing the diffusivity of electrolytes, in this case the ionic iron [43].

$$D^{\circ}_{AB} = 0.8931 * 10^{-14} * T * \frac{(\lambda^0_- * \lambda^0_+)}{(\lambda^0_- + \lambda^0_+(} * \frac{(|z_+| + |z_-|)}{(|z_+| * |z_-|)} \tag{2.21}$$

Where:

T = absolute temperature [K]

λ^0_- and λ^0_+ = the cationic and anionic conductances at infinite dilution [S/equivalent]

z_+ and z_- = cationic and anionic valences

The values for the ionic conductances are normally given only at STP, thus Walden's Rule [44] is applied when calculating diffusivities at elevated tem-

peratures, with μ equal to the dynamic viscosity of the solvent.

$$\frac{\lambda^0_{+@25^\circ\mathrm{C}}}{\lambda^0_{+@T}} = \frac{\mu_{25^\circ\mathrm{C}}}{\mu_T} \tag{2.22}$$

Where:

μ = dynamic viscosity [cP]

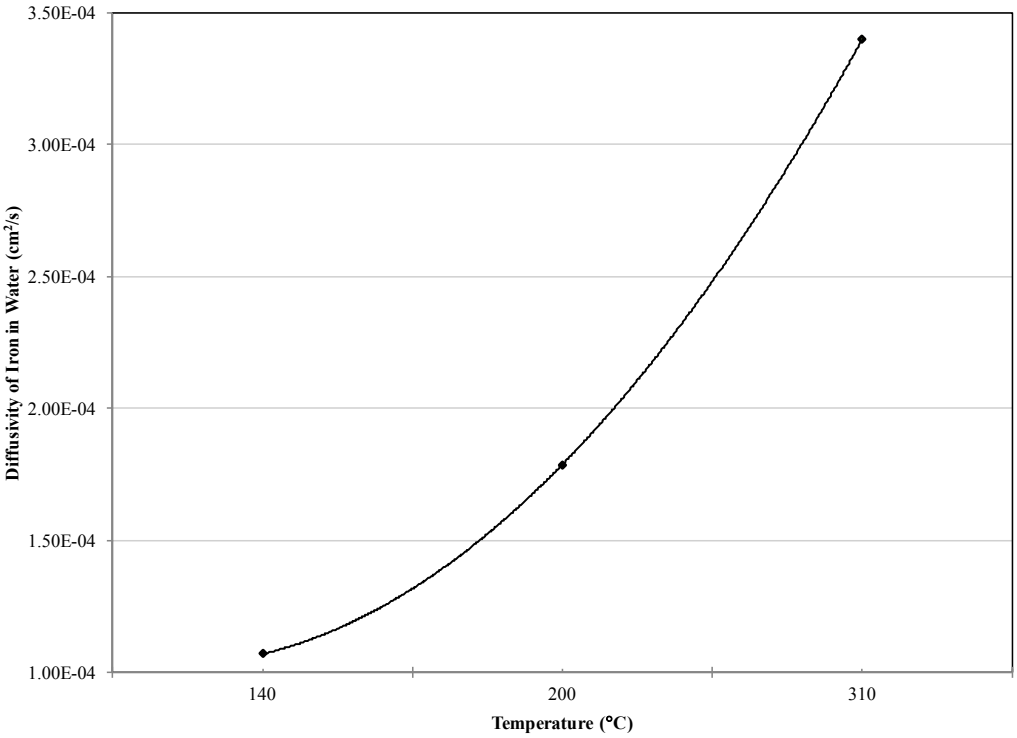

Figure 2.6: Variation of iron diffusivity (Fe^{2+}) in water with temperature calculated with Equation2.21

Figure 2.6 shows the trend of iron diffusivity in water as calculated using

Equation 2.21 through the typical range of interest for power plant systems, as used in the UNB model.

2.3.6 Flow

Fluid flow effects on FAC are often interpreted as a direct function of fluid velocity or wall shear, with the understanding that at some critical velocity/shear, particle removal leading to a breakdown of the oxide occurs [45].

Syrett [46] questioned whether the shear stresses induced at the wall by the flowing fluid were sufficient to remove the oxide layers. Heitz [47] proposed that pressure fluctuations in the turbulent flow may increase shear stress leading to oxide degradation. Nesic and Postlethwaite [48] then concluded that wall shear stress was insufficient to induce mechanical removal. Rather, near-wall turbulence was the overriding hydrodynamic force associated with oxide degradation causing FAC.

The application of shear stress directly as a means of particle removal becomes even more questionable when the flow is disturbed (by a nozzle for example) resulting in highly turbulent sections of flow, where substantial velocity and pressure differentials can be found. In these cases, another consideration in applying shear stress directly for FAC predictions is the fact that at some distance from the flow disturbance, there will be a reattachment point, where the wall shear stress will be equal to zero [49]. At this

point the fluid effects from wall shear on the FAC rates should be zero, yet experimental and plant data show that this is actually the point of highest degradation.

More recently, Schmitt [50] has suggested again that fluid dynamic forces are critical in the FAC mechanism. It is proposed that 'freak' singular events occur where intense micro-turbulent events impinge on the protective oxide perpendicular to the pipe wall. This phenomena is not unlike the 'bursts' of highly turbulent events disrupting the fluid boundary layer to detach particles that were previously described by Cleaver and Yates [51]. These forces are estimated in the mega-Pascal range, overcoming the previous studies conclusions that wall shear stresses were too low to cause mechanical damage to the oxide layer.

Ahmed [52] indicates that inspections from power plants show that components downstream of a flow disturbance (particularly flow elements like orifices, valves, elbows etc.) are the most susceptible to FAC. Inspection data were shown indicating that effects of flow disturbances could be detected on downstream components, generally resulting in higher than anticipated FAC rates, likely a result of excessive turbulence in the component.

2.3.7 Mass Transfer

The mechanism of mass transfer has a substantial influence on the severity of FAC. In the case of FAC, the mass transfer specifically refers to the transfer of ionic and soluble iron species from the surface of the oxide through the fluid boundary layer into the bulk coolant, driven by a concentration gradient between the two locations.

In some of the more complex analyses completed at UNB Nuclear, mass transfer coefficient values were determined through computational fluid dynamics analysis of the flow in a system of interest, and the mass transfer correlated with heat transfer via Equation 2.23 [26]:

$$\frac{Nu}{Pr^n} = \frac{Sh}{Sc^n} \tag{2.23}$$

Where:

Nu = Nusselt number

Pr = Prandtl number

Sh = Sherwood number

Sc = Schmidt number

n = a positive exponent less than one (fit to data [26])

Others have approached the problem of mass transfer values downstream of flow disturbances with empirical correlations as well. Coney [53] presented a distribution of Sherwood numbers downstream of an orifice, while Tagg [54]

and Rizk [55] have produced various values of maximum Sherwood number downstream of an orifice. There is significant variation between the values produced by the empirical correlations available [56]. This variation highlights the need to adopt computational fluid dynamics analysis when modelling FAC to resolve the complex nature of mass transfer in systems other than straight pipes and obtain representative predictions of actual wall loss.

More simply, mass transfer correlations relate system conditions to turbulent flow in a straight pipe [57]. Correlations to determine mass transfer calculate the dimensionless Sherwood Number, Sh, given by Equation 2.24, which represents a ratio of total mass transfer to that calculated for diffusion alone, with d equal to the characteristic length and D°_{AB} equal to the mass diffusivity (the nature of Sh is analogous to the Nusselt number in heat transfer calculations).

$$Sh = \frac{k_m d}{D^{\circ}_{AB}} \tag{2.24}$$

Where:

k_m = mass transfer coefficient [cm/s]

d = characteristic length [cm]

D°_{AB} = diffusivity [cm^2/s]

Determination of the Sherwood number is based on correlations of the general form:

$$Sh = \alpha Re^{\beta} Sc^{\gamma} \tag{2.25}$$

where Re, the Reynolds number, equals:

$$Re = \frac{\rho * U * d}{\mu} \tag{2.26}$$

with ρ equal to the density of the fluid in [g/cm^3], U equal to the linear velocity of the fluid in [cm/s], d equal to the characteristic linear dimension in [cm], and μ equal to the dynamic viscosity in [cP]. The Schmidt number, Sc, (a dimensionless number relating kinematic viscosity, υ in [cm^2/s], to mass diffusivity) is given by:

$$Sc = \frac{\upsilon}{D^{\circ}_{AB}} \tag{2.27}$$

Berger and Hau [57] presented a series of correlations to calculate the Sherwood number for a variety of conditions. The Sherwood number, Sh, is often calculated as Equation 2.28, given as Equation 8 in [57] for Nu, but according to Equation 2.23, they are equivalent.

$$Sh = 0.0165 Re^{0.86} Sc^{0.33} \tag{2.28}$$

Given the relatively low Schmidt numbers observed in the UNB loop experiments ($\sim$20), a more general version of the Berger and Hau correlation was applied to obtain mass transfer coefficients here, Equation 2.29, where

Equation 2.28 may produce inaccurate results at lower Sc numbers (Le [28])

$$Sh = 2 + (0.0165 + 0.011 * Sc * e^{-Sc}) * Re^{\left[0.86 - \left(\frac{10}{(4.7+Sc)^3}\right)\right]} * Sc^{1/3} \quad (2.29)$$

This equation is considered to provide reasonable mass transfer coefficients for a Reynolds Number range from 10^4 to 10^6 and Schmidt numbers ranging from 0.6 to 10^4.

Chapter 3

Experimental

3.1 Loop Experiments Overview

As a basis for the manipulation of the UNB mechanistic model, new data were needed to assess existing assumptions and to support new hypotheses on the behaviour of the FAC mechanisms. A series of experiments were carried out to examine the effects of iron concentration in the bulk coolant on FAC rates. The following sections will describe the experimental apparatus used and the experimental conditions examined.

3.2 Loop Description

The experimental portion of this work was carried out at the Centre for Nuclear Energy Research (CNER) on the UNB campus. The CNER Loop 1 facility, Figure 3.1 and Figure 3.2, and adjoining analytical chemistry lab were used. CNER Loop 1 is a high pressure, high temperature recirculating water loop designed to simulate power plant heat transport system operating conditions.



Figure 3.1: CNER Loop 1

The loop is constructed of stainless steel tubing and fittings, with a Hastelloy-C autoclave. The high pressure section of the loop can operate at pressures up to 9.6 MPa (1400 psig), and a maximum possible temperature of 310°C at a flow rate of 0.85 L/min. The low pressure side of the loop is limited to

between 0 and 69 kPa (10 psig) and a temperature of approximately 30°C, and contains the flow meters and online chemistry analysis instrumentation. As the construction of the loop is generally inert and robust, a wide variety of chemistry conditions can be run without significant conditioning challenges, such as degradation of valve packing materials. In recent years, both ammonium hydroxide (NH_4OH) and lithium hydroxide (LiOH) have been used for pH control. Hydrazine (N_2H_4) has also been used from time to time as an oxygen scavenger, depending on the chemistry conditions being simulated. Operational control of the loop is provided by the ACCIS^{TM} control soft-

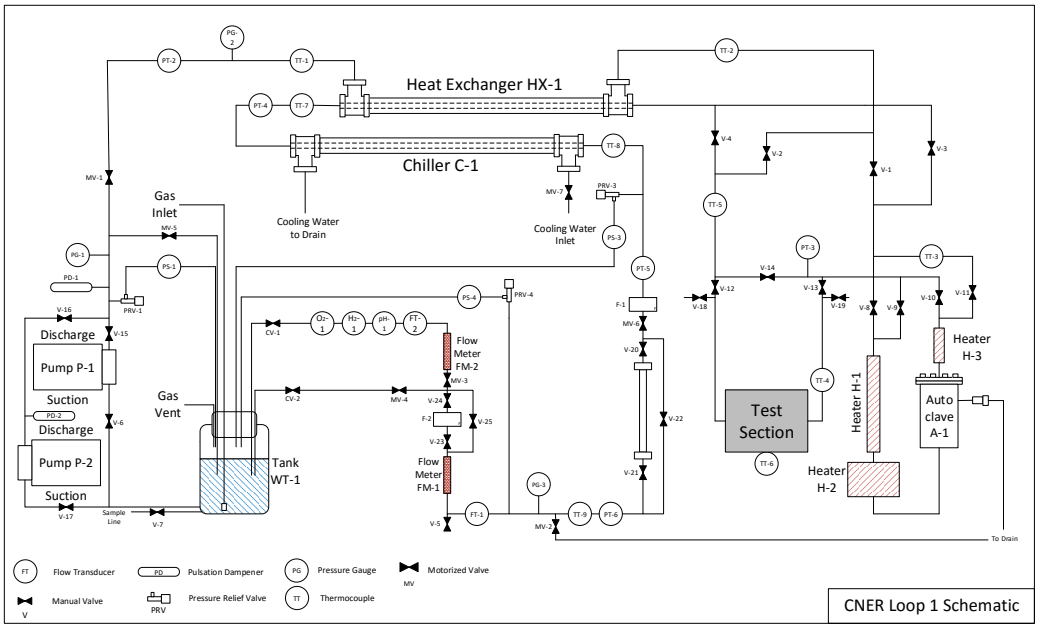

Figure 3.2: CNER Loop 1 flow diagram

ware developed by Atomic Energy of Canada Limited (AECL) for CANDU power plant systems. This control software enables Loop 1 to maintain very

strict control over flow, pressure and temperature via motorized flow control valves and temperature controllers. It also permits configuration of detailed set-points for automated safety controls to minimize over-pressurization of the system when changing configurations in the test sections or due to failures during off hours. The loop is fed from a 75 L stainless steel tank (Figure 3.3) filled with approximately 50 L of deionized water. The tank is equipped with a sight glass, argon gas purge system, vent lines, sample port, inlet/outlet loop connections and an injection port. The injection port is used to manipulate system chemistry by injecting various amines or other chemicals via a syringe.



Figure 3.3: Loop 1 75L tank

The system flow is provided by a reciprocating positive displacement pump,

a Milroyal Model C rated for 13.1 MPa (1900 psig) and flows up to 6 L/min. Flow control at the pump is manipulated by manually adjusting the pump stroke. The loop itself is constructed almost entirely from various diameters (3.2 mm (1/8") -19.0 mm (3/4")) of 316 stainless steel tubing with Swagelok Type 316 stainless fittings throughout. Flow stabilization is provided via a pulsation dampener consisting of an EPT bladder housed in a stainless steel vessel and charged with 2.75 MPa (400 psi) of nitrogen. The dampener operates on the principle that each cycle of the pump results in a flow/pressure fluctuation that is absorbed by the flexible bladder, smoothing the flow to a pressure variation of ±35 kPa (5 psi).

Temperature control is provided with three heaters constructed of various diameters of stainless steel tubing wrapped in independently controlled heat tapes to provide the appropriate fluid temperatures. A counter-current shell and tube heat exchanger is also included in the loop to recover return water heat for pre-heating. Cooling of the return water prior to its entering the chemistry section is provided by an additional counter-current shell and tube heat exchanger fed by domestic cooling water. To reach temperatures higher than approximately 240°C, additional cooling capacity must be provided with the aid of a chiller unit to meet the temperature requirements of the low pressure section.

After the cooler, the water reaches a set of parallel ion exchange (IX) columns each loaded with approximately 300 mL of Purolite NRW-37 mixed bed resin.

One IX column resin is saturated with the amine of choice while the other is unsaturated resin (ie., H^+ and OH^-) and normally valved out of the system. This permits more precise chemistry control over a single saturated column by providing a means to reduce pH quickly by passing the flow through the unsaturated column.

The chemistry section of the loop contains instrumentation to monitor parameters such as pH, dissolved oxygen concentration and in some configurations, dissolved hydrogen concentration. Orbisphere electrochemical sensors provide concentration to the ppb level for dissolved gas, and an OMEGA industrial temperature compensated pH meter provides online monitoring of relative pH although bench-top pH measurements from grab samples are used for actual chemistry control.



Figure 3.4: Loop 1 test section

The test section of the loop, Figure 3.4, is housed in a modified laboratory

oven not only to provide insulation for precision temperature control, but also as a safety precaution in the event of a pressure boundary failure of the probe assembly. The test section provides an isolated loop at temperature and pressure that can be valved in and out of the operating loop without shutting down, allowing precision chemistry conditions to be set and then introduced to the experimental probe. It also has valving for vacuum and argon purge systems to evacuate the entire test section prior to initial valve-in.

3.3 FAC Measurement Probes

To enable online measurement of FAC rates in the experimental loops, FAC resistance probes are installed in-line. As developed by Cook [14], the probe is employed to provide real time wall thickness measurements during the experiment. From these wall thickness measurements, rates of wall thinning can then be inferred.

The experimental probe, Figure 3.5, referred to as a resistance probe, is a UNB Nuclear design which allows real time evaluation of FAC rate by correlating wall thickness over the measured section to the electrical resistance. The probes are machined from a material of interest (for example, A106B low chromium steel (0.019%) harvested from spare feeder pipes obtained from the Point Lepreau Nuclear Generating Station), with a typical 6.35mm (0.25")

OD, 80 mm length and varying ID depending on the mass transfer rate required. An ID of 1.6 mm is the standard probe, but 1.0, 2.4 and 3.2 mm are used as required. A reduced wall thickness section 12.5 mm in length is machined at the centre of the probe, bounded on each end by a circumferential notch. Leads of solid silver wire are secured in the notches using silver solder to create a pathway through which a current is passed across the reduced section. The correlation of current passed to wall thickness will be described in the next section.



Figure 3.5: UNB 1.6 mm ID resistance probe installed in the test section

In this experimental program, only 1.6 mm internal diameter probes were used for FAC measurements to achieve high fluid velocity and mass transfer rates. Note that smaller diameters are not necessarily feasible as machining limits are imposed by the drill bit size. As the bit diameter gets smaller, the tendency for it to drift increases, leading to an uneven bore through the

probe.

Prior to assembly and installation of the probe into the test loop, the probe's internal diameter is chemically pickled by introducing a 10:1 solution of hydrochloric acid. The acid solution is circulated through the probe using a peristaltic pump for nine minutes, followed by five minutes of fresh de-ionized water. The process is completed by blowing the probe dry with argon. The purpose of this process is to ensure that only bare steel is present at the beginning of the tests.

The ends of the probes must be electrically isolated from the piping of the loop for the wall thickness measurement to be possible. Each end of the probe is encased in a length of polytetrafluoroethylene (PTFE) tubing. The PTFE tubing sleeve is shrink-fitted to the probe by applying heat. Prior to the current work, this was done manually with a propane torch. Investigation into erratic FAC behaviour observed during the first hours of probe exposure led to the notion that combustion products may be left behind inside of the probe bore that need to be removed prior to oxide formation. A commercial heat shrinking tool was procured that uses an electric heating element, and a jig was designed and built to accommodate various sizes of probe. The PTFE tubing is placed over the end of the probe, and then exposed to the heating element, rotating slowly by hand to ensure even heat distribution. As the PTFE increases in temperature (at a temperature far below the melting point of the silver solder), it turns translucent, propagating from the tip of

the probe toward the centre of the probe. Once approximately 75% of the length of the PTFE sleeve has become translucent, it is removed from heat and allowed to cool. Caution must be used to remove the probe from the heat at this time, else overheating will cause the PTFE to crack.

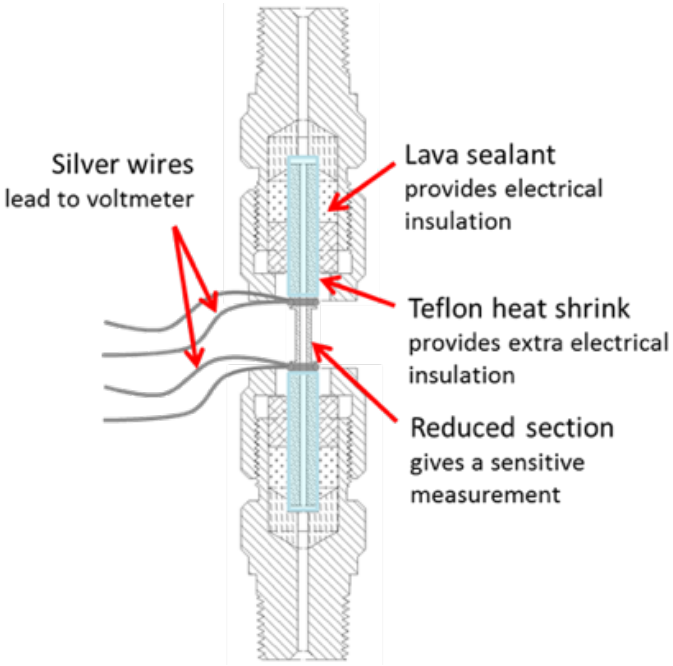

Figure 3.6: UNB 1.6 mm ID resistance probe mounted in electrically isolating modified Conax fittings

Once both ends of the probe are encased in PTFE, the probe is mounted into a customized Conax fitting assembly, where compression of Conax Lava seals onto the PTFE sleeve form the pressure boundary seal for the probe. Figure 3.6 shows the standard UNB measurement probe mounted in its pressure

fittings. A set of integral retaining plates at each end of the Conax with threaded rods connecting them form a safety cage. This cage is in place to restrain the probe assembly should a rapid change in pressure occur.

3.4 Temperature Correlation

The accuracy of the wall thinning measurements obtained from the FAC probes is highly dependent on the relationship between electrical resistance and temperature. The basic relationship used to correlate electrical resistance to wall thinning is given by Equation 3.1, and is a commonly applied calculation as described in ASTM G96-90(2001) [58] for electrical resistance techniques for corrosion monitoring.

$$R = \frac{\rho L}{A} \tag{3.1}$$

Where:

R = Resistance [Ω]

ρ = Specific Resistivity [$\frac{\Omega}{cm^2}$]

A = Cross Sectional Area [cm^2]

L = Monitored Length [cm]

A current is passed between two points on the probe, flowing through the reduced section. By measuring the voltage drop across the reduced section

length, applying Equation 3.1 allows for the calculation of the cross sectional area, and, in turn, the wall thickness.

A critical parameter in this calculation is the resistivity (ρ), a function of temperature specific to the material of interest. The resistivity is determined experimentally. In this case, a length of wire machined from the A106B probe material was mounted in a fixture and exposed to a range of temperatures, establishing a resistance to temperature correlation, Equation 3.2 [14].

$$\rho = 8.600 * 10^{-4} T^2 + 5.063 * 10^{-1} T + 1.956 * 10^2 \tag{3.2}$$

This correlation has produced reasonable results, but suffered from small inconsistencies due to minor variations in coolant temperature. Over the course of a nominally isothermal loop experiment, fluctuations in coolant temperature can be expected within +/- 1 degree. When conducting non-isothermal experiments, marked variations in absolute wall thickness measurements are observed when changing temperatures and while new temperature conditions stabilize (as there is a dwell period after changing temperatures before the probe metal temperature stabilizes).

As a result of the observed inconsistencies, Lertsurasakda [59] expanded on the simple correlation of resistivity to account for a number of other variables.

The new temperature correlation is presented in Equation 3.3.

$$R = \rho(\frac{L}{A} + \Upsilon + \alpha T + \beta) \tag{3.3}$$

Where:

Υ = end effect term (determined during calibration) [cm^{-1}]

α = geometrical temperature coefficient [$\mathrm{mm}^{-1}{}^{\circ}\mathrm{C}^{-1}$]

β = geometrical corrector term [cm^{-1}]

Of particular importance in this correlation is the introduction of the Υ parameter, Equation 3.4, which is intended to take into account subtle differences between individual probes due to fabrication and material inconsistencies. While the already established resistivity of the material provides the fundamental response of the material to temperature variations, this Υ term further expands this resistivity to account for the influence of the assembly of the probe to variations in temperature. The Υ value must be determined experimentally, through a calibration process that is completed immediately on exposing the probe to the coolant.

$$\Upsilon = \frac{L}{A}\left(\frac{\rho^*}{\rho} - 1\right) \tag{3.4}$$

Where:

$$\rho^* = \frac{R_{measured}A}{L} \tag{3.5}$$

In Equation 3.4, the ratio of $\frac{\rho^*}{\rho}$ provides a ratio of the specific resistivity of the

particular probe to the general resistivity of the material with temperature. Including this effect enables the resistance measurements to remain stable during temperature fluctuations.

The remaining factors included in Equation 3.4 are α and β, corrections for temperature effects on the geometry of the probe and fabrication geometry of the probe, respectively, given by Equations 3.6 and 3.7.

$$\alpha = 2.582 * 10^{-5} ID^2 - 5.073 * 10^{-5} ID + 1.507 * 10^{-5} \tag{3.6}$$

$$\beta = 2.937 * 10^{-2} ID^2 - 9.444 * 10^{-2} ID + 7.593 * 10^{-2} \tag{3.7}$$

Experimental validation of this correlation was completed by the author. A 1.6 mm internal diameter resistance probe was fabricated from A106B carbon steel and mounted into the experimental loop. During this test, oxygen was intentionally introduced into the coolant to stifle FAC, and thus maintain a constant wall thickness in the probe. The probe was exposed to a range of temperatures from 120°C to 200°C over the course of several days, allowing the probe temperature to completely stabilize to the coolant temperature at each interval. The resistance measured from these tests was plotted against temperature, and a correlation, specific to this probe, was established for Υ (Figure 3.7). With the correlation established, the probe was carefully removed from the loop and the internal diameter of the probe was bored out to 2.4 mm without disturbing the soldered leads. The probe was reinstalled into

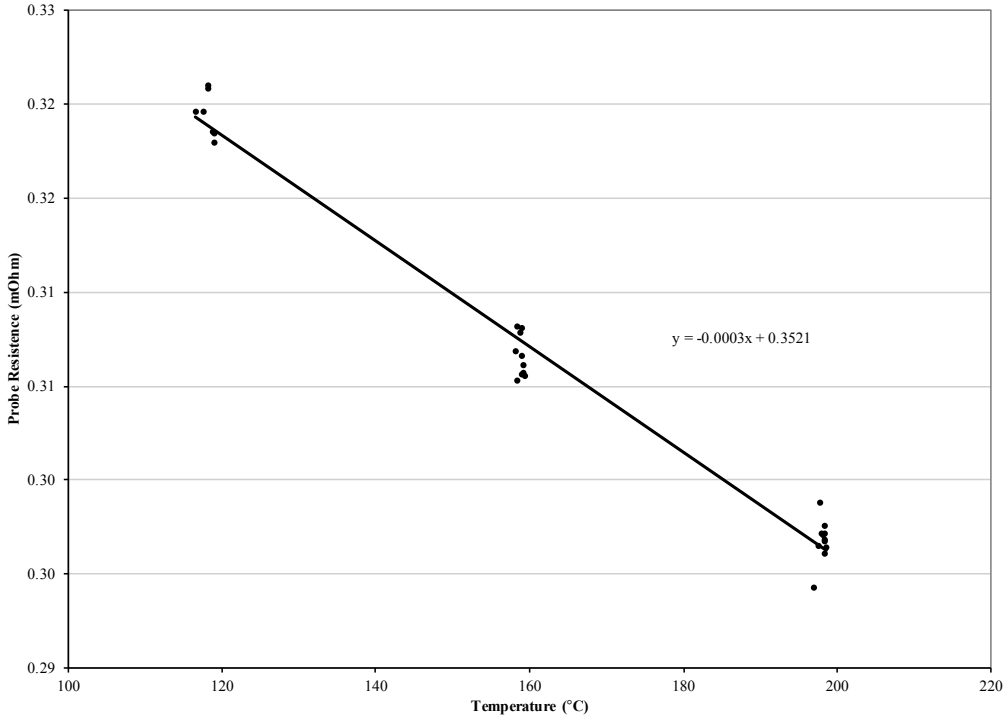

Figure 3.7: Example calculation of linear Υ value

the loop and the temperature variation was repeated with the new diameter. Plotting the results by applying the exact correlation established for the 1.6 mm internal diameter probe resulted in a measurement of 2.4 mm internal diameter at all temperatures, shown in Figure 3.8. Analysis was carried out to

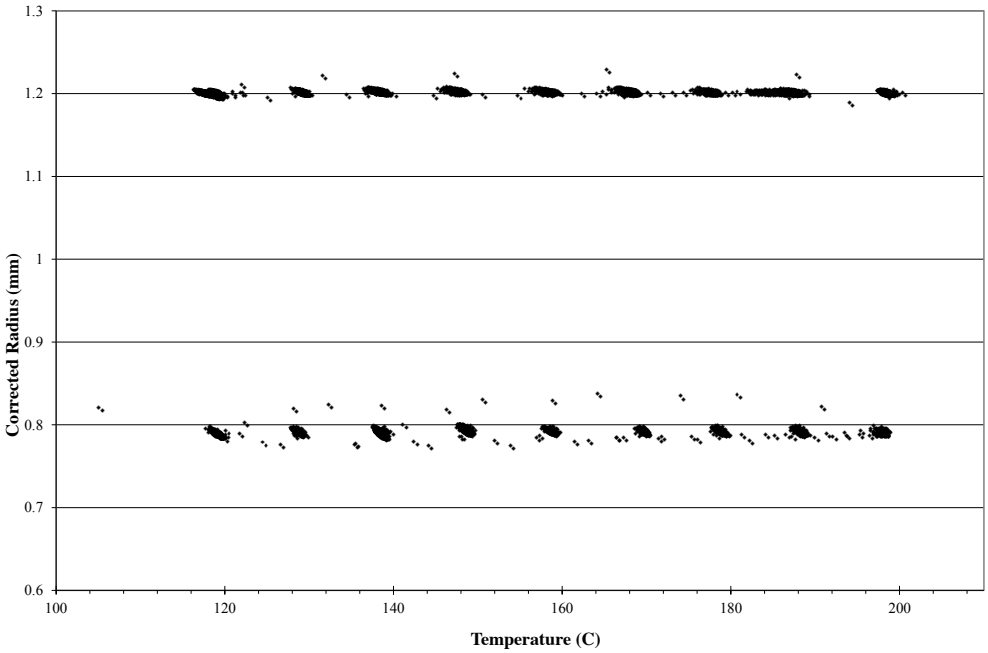

Figure 3.8: Temperature correlation validation results: corrected radius vs. temperature

determine the best technique for commissioning the probes. Multiple points were considered, but ultimately a three-point calibration was considered to be of sufficient accuracy and precision to negate the need for lengthly calibration processes spanning several days. For example, for a non-isothermal experiment running at 140°C and then at 200°C, a three point calibration

of 120°C, 160°C, and 220°C would be sufficient to readily determine Υ. The type of relation was also considered, looking at linear, logarithmic and power fits to the points. A linear relation provides a response within +/- 2% of the alternatives, and was chosen for simplicity.

3.5 Experimental Conditions

The target operating conditions for the experimental portion of this work were chosen to capture a reasonable range of power plant operating conditions within the limitations of the test loop to investigate FAC mechanisms. The majority of the experimental runs were conducted under neutral chemistry conditions at either 140°C or 200°C. Runs were also completed under ammoniated conditions, with a target pH of ∼9.2, with the addition of NH_4OH. Several of the early runs were also completed using hydrazine, N_2H_4, as an oxygen scavenger, particularly when high pH runs were conducted, as oxygen concentrations above one ppb will stifle the FAC [7].

3.6 Iron Effects

To study the effects of bulk iron concentration on FAC, a means of reliably increasing the iron concentration had to be developed. Several methods

were investigated including iron turnings in autoclaves, inline iron wire feeds and sacrificial piping arrangements. Each of these methods was considered to be impractical due to geometrical constraints or availability of suitable materials. Calculations were performed based on the initial runs in Loop 1, and a system made up of 1.6 mm ID sacrificial probes made from the low chromium A106B material with a total length of approximately 0.80 m was proposed, Figure 3.9.



Figure 3.9: Iron injection system (right) and measurement probe(left)

This method was selected and the design length chosen based on the assumption that material lost from the ID of the probe could reasonably be assumed to increase the bulk coolant dissolved iron concentration. As this relation was to be investigated by the study, some assumptions were made in the calculation (ie: linear reduction of FAC rate along the length of the tube) and some conservatism was applied.

A series of valves were installed in the test section upstream of the resistance probe to permit the establishment of a steady state FAC rate in the probe, then, effectively without interrupting flow, the iron input device could be valved in. The result is a distinct response in the data showing an almost immediate response to the introduction of higher concentrations of dissolved iron in the coolant. The effect is shown in Figure 3.10. The location of the measurement probe is sufficiently downstream of the iron source to mitigate the influence of incidental flow effects on the measured FAC rate.

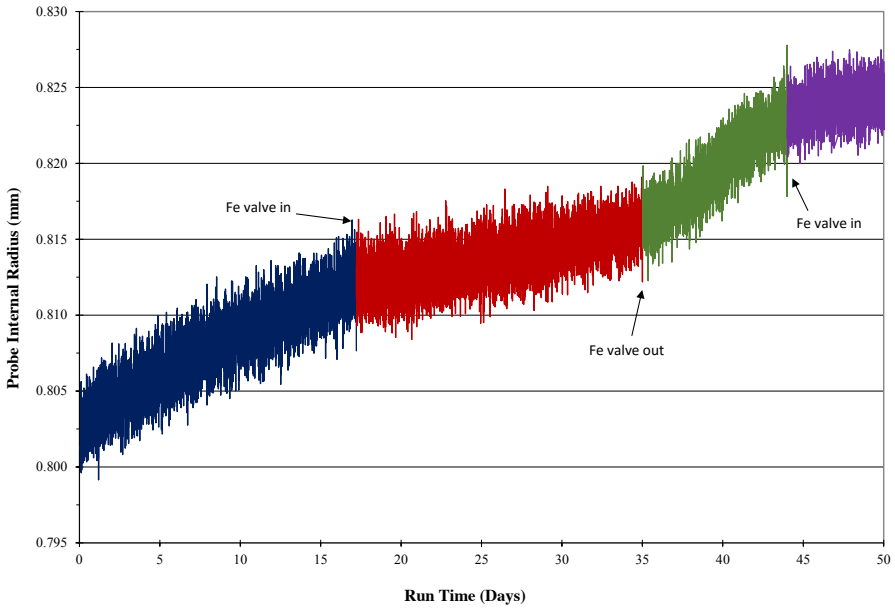

Figure 3.10: Run 2 data showing distinct changes in FAC rate with iron source valve-in

Of critical importance in achieving this effect is ensuring that the conditions within the iron input device are maintained such that more resilient oxides

do not form during the valved out period (Fe_2O_3 for example). The loop must be maintained to eliminate the possible ingress of oxygen. During the vacuum purge process when first valving-in a new probe, it is essential that the iron input device be included in the vacuum/purge, and maintained in a dry pressurized with argon state until the first valve-in. After that, when the iron input device is valved-out, it should maintain a pressurized state with the deoxygenated coolant from the loop, ideally resulting in only some general corrosion in the stagnant coolant which is quickly removed once flow is reintroduced and FAC proceeds.

3.7 Sampling

Once data had been generated showing the response to changes in the FAC rate due to increasing iron concentration, the next step was to attempt to physically measure the concentration gradients through the test section.

Current industry practices for sampling corrosion products typically involve running a sampling line from a point in the system and then running the sample through a cooler/pressure reducer where the sample temperature is far lower than operating temperature [60]. As iron solubility decreases dramatically at temperatures below 120°C, these methods may not provide a quantitative measurement of actual concentrations in the bulk coolant.

Thus a method to collect grab samples of the at-temperature coolant was developed and is described in the following section.

3.7.1 Apparatus

The system designed to capture at-temperature grab samples consists of a set of sample vessels and a complex valve scheme to allow for online sampling to occur. Two vessels were chosen to permit grab sample collection upstream and downstream of the FAC measurement probe, providing the most flexibility in measurement. This arrangement would allow measurement of the concentration difference across the probe, and also the concentration input from the iron input device, which will provide a direct measurement showing the relation of FAC rate to dissolved iron concentration in the bulk coolant.

The arrangement of the modified test section is shown in Figure 3.11. A custom valve manifold was built, and the valve system allows the isolation of the entire test section, the introduction of the iron saturation device, and collection of grab samples without interrupting flow through the FAC measurement probe for long periods.

In order to collect grab samples of the bulk coolant for the purpose of low level iron concentration analysis, all components used in the removable portion of the sampling system must be non-ferrous to minimize contamination. Accordingly, two 300 mL autoclaves manufactured entirely from Zirconium 705

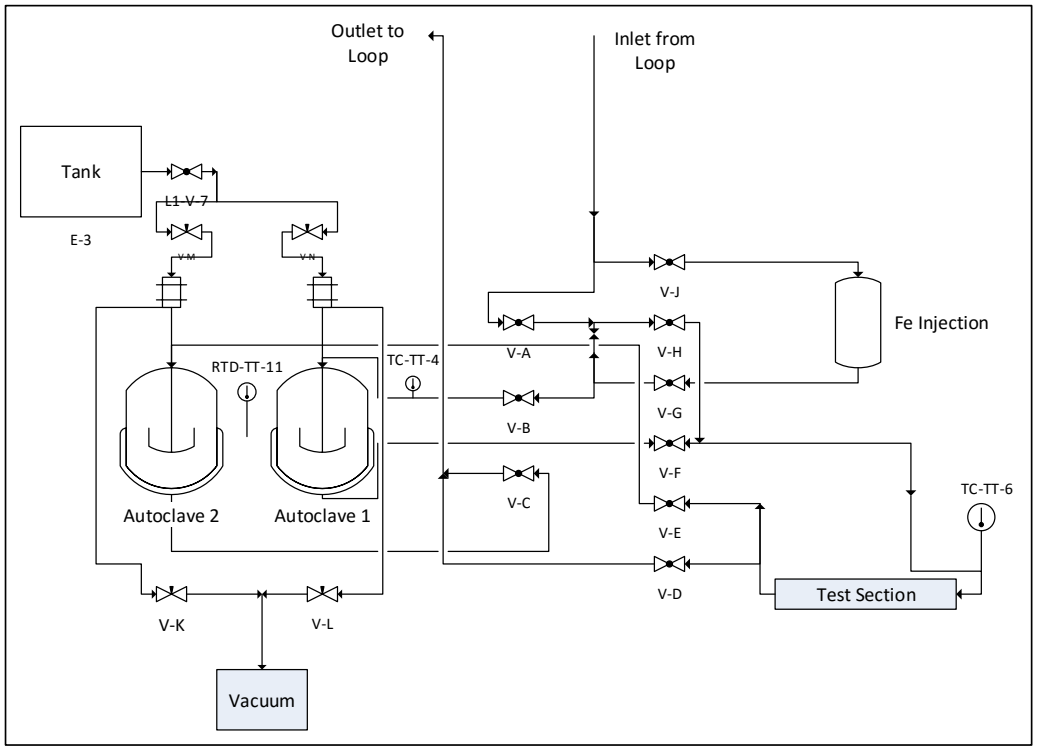

Figure 3.11: Loop 1 sampling system flow diagram

are employed in the system. These autoclaves were repurposed from previous experiments, and were chosen because of their material of construction, not their size. All wetted fittings, gaskets and tubing within and adjacent to the autoclaves are either Zirconium 705 or titanium alloys containing minimal iron.

The autoclaves are mounted within a Fisher Scientific laboratory oven which has been modified to permit the various tubing and monitoring instrumentation to be connected. Each autoclave has the following penetrations:

1. Inlet
2. Outlet
3. Vacuum
4. Argon purge
5. Safety Head (with Inconel rupture disc)

The autoclaves mounted in the modified oven are shown in Figure 3.12. A vacuum pump is connected to the autoclaves, as well as a 3.2 mm (1/8") fill line coming from the loop tank. To minimize shock on the loop, the autoclaves are pre-filled with tank water so that a 300 ml pocket of air is not introduced to the system. The tank water is very clean, de-oxygenated and de-ionized water, as the loop water has been passed through the IX columns to remove corrosion products and other impurities that might enter the flow.



Figure 3.12: Zirconium autoclaves mounted in laboratory oven.

3.7.2 Procedure

Once the autoclaves have been filled, they are pressurized and checked for leaks by slightly opening their inlet valves. Once leak tightness is confirmed, they are brought to operating temperature with the oven prior to valving into the flow. During the heating process, the inlet valves are cracked slightly open to allow any excess pressure in the autoclaves to be released to the loop. Temperature control is key to the success of the experiment. Figure 3.13 shows the solubility of iron at various pH and temperatures (based on Tremaine and Leblanc [16] and Sturla [61]). Based on the target loop temperature (in the case of Figure 3.13, the target is 140°C indicated by the vertical dashed line), the oven temperature must be held at slightly below

140°C for pH = 7.0. The reason is that if the temperature were to be higher in the autoclave than the incoming bulk coolant, as the temperature increased in the coolant, the solubility of iron would decrease, and thus iron could begin to precipitate out of solution and deposit on the inside surface of the autoclave during the sampling process.

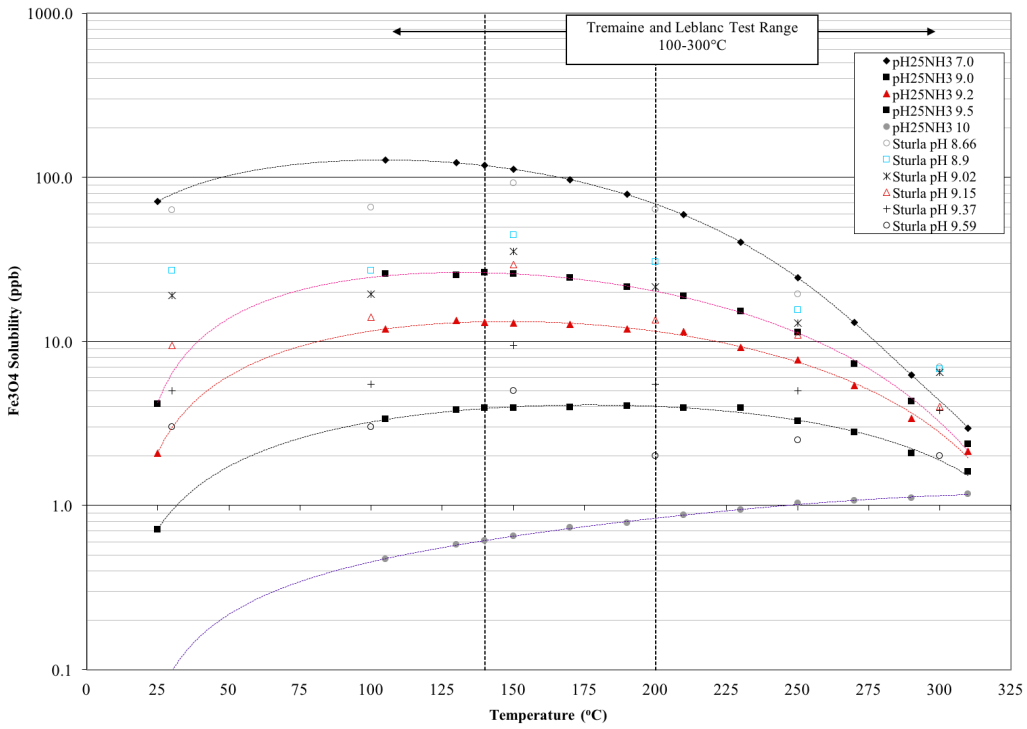

Figure 3.13: Extrapolated solubilities of magnetite in water at various conditions

The autoclaves are exposed to the flow for a 24 hour period to permit any minor adjustments to temperature in the system as well as to allow any

minor change to the FAC rate as a result of the introduction of the sampling system to stabilize. Once steady state FAC has been confirmed, the bypass is opened and the outlet to the autoclave is quickly closed, followed by the inlet, thus capturing a grab sample of the bulk coolant. The oven is turned off, and the autoclaves are cooled to room temperature over 6-12 hours.

As the autoclaves cool with the grab sample inside, the dissolved iron in the bulk coolant precipitates onto the inside surfaces. This has been verified by measurement as described below.

To assess the sample from an autoclave, a 2% solution of nitric acid (HNO_3, Fisher Scientific Trace Metals grade) is introduced to the coolant solution which was extracted into a 500 mL volumetric flask inside a nitrogen-purged glove-box. Extraction is via a peristaltic pump. All tubing, fittings and other components of the sampling system that come into contact with the acidified sample have been assessed for iron contamination, resistance to nitric acid solutions, and gas permeability. All glassware and handling equipment for collecting individual samples are washed, soaked for 24 hours in a 3% HNO_3 bath and then triple-rinsed with deionized water prior to use.

Once the autoclave contents are acidified in the flask, a sample for reference is extracted to confirm the initial dissolved iron in the bulk grab sample from the autoclave; typically < 2 ppb of iron is reported, indicating that any iron present in the coolant when collected at temperature has precipitated

inside of the autoclave. Next, the precipitated iron is stripped from the inside surfaces of the autoclaves by pumping the nitric acid solution through the autoclave with the peristaltic pump. Initially, 10 minutes of pumping produced reasonable results, but was not long enough to avoid carry-over of precipitated iron in later runs. A series of bench-top experiments indicated that a pumping time of 6 hours was adequate.

A total of six samples are collected from each autoclave for each run condition, one blank, three primary samples, and two filtered samples (passed through a 0.2 μm PTFE filter). The samples are transported from CNER to the laboratory of the Provincial Research and Productivity Council (RPC) adjacent to the UNB campus for analysis by inductively coupled plasma emission spectroscopy (ICP-ES) to establish the concentration of dissolved iron, which is detected as total ionic iron (Fe^{2+} or Fe^{3+}, the instrument does not differentiate). ICP-ES was selected over inductively coupled plasma mass spectrometry (ICP-MS) because it is more reliable for detecting iron concentrations below 10 ppb without a significant investment in time and instrument maintenance. Since the ICP-MS was shared with other workers, general iron contamination of the instrument that was well within the acceptable limits for other work, was totally unacceptable for the measurements being taken in this work. To accurately obtain real measurements below 10 ppb, the ICP-MS would need to be dismantled and cleaned prior to each sample batch. This process takes approximately one week, during which no other samples

can be run.

Chapter 4

Experimental Results

The objective of the experimental portion of this work was to observe the effect of changes in iron concentration in the bulk coolant on FAC rate. Loop modifications and sampling system development were carried out to investigate this response through a series of experimental runs, summarized in Table 4.1, the results of which are presented in the following sections.

Table 4.1: Experimental Run Summary with Target Conditions

Run	Flow Rate [LPM]	Temp [°C]	pH	N_2H_4	Sampling
1	$0.5 - 0.85$	140	9.2	Y	N
2	0.85	$140 - 200$	9.2	Y	N
3	0.85	$140 - 200$	9.2	N	N
4	0.85	$120 - 200$	9.2	N	N
5	$0.5 - 0.8$	$140 - 200$	7	N	Y
6[1]	$0.5 - 0.8$	$140 - 200$	7	N	Y
7[1]	0.8	$140 - 200$	9.2	N	Y
8[1]	0.8	$140 - 200$	9.2	N	Y
9[1]	$0.5 - 0.8$	$140 - 200$	7	N	Y
10	0.5	140	7	N	N

[1] Run attempted but interrupted by mechanical issues with loop

4.1 Loop Runs

4.1.1 Run 1

CNER Loop 1 had been laid up for some time prior to being engaged for this research program. Before commissioning to begin these experiments, the loop was cleaned with an organic acid solution used at UNB for loop conditioning. A solution of 0.01M citric acid and 0.005M oxalic acid in deionized water was cycled through the loop for several hours, and then flushed multiple times with fresh deionized water.

The loop was started and brought up to temperature. The operating parameters of the run (Table 4.2) were set. Some difficulties were encountered

maintaining an O_2 concentration around 1 ppb, which is necessary at these conditions since at the target chemistry, FAC will stifle at O_2 concentrations slightly higher than 1 ppb [7]. As a result, hydrazine (N_2H_4) was added to the loop as an oxygen scavenger.

Table 4.2: Run 1: Target chemistry conditions

Parameter	Value
$FlowRate\ [LPM]$	0.5
$Temperature[^{\circ}C]$	140
pH	9.2
$Oxygen\ [ppb]$	< 1
$NH_3\ [ppm]$	$0.35 - 0.5$
$N_2H_4\ [ppb]$	< 50

After several days, the FAC measurement probe was valved in, and monitoring began. After two days of operation the O_2 level increased dramatically, stifling the FAC and the run was abandoned.

The O_2 ingress was traced to a faulty injection septum assembly. The septum assembly is built by fitting a natural rubber septum into a Swagelok fitting and mounting this to tubing on the loop tank. It was determined that the septum location was not ideal, being on a relatively high flow return line, and that a slight localized vacuum may have been created behind the septum, drawing air into the loop. The septum was changed and the fitting relocated to the top of the tank (where the back of the septum would be exposed only to the argon purge gas in the tank). The concentration of O_2 was reduced and other chemistry parameters stabilized quickly.

Previously, when valving in an FAC measurement probe, there was a large O_2 spike that would take up to several hours to come back to operating levels (in this case, below 1 ppb). To reduce this, an improvement to the valve-in procedure was developed to minimize this effect. After the probe is installed in the loop and just prior to valve-in, the test section is drained of any standing water, and a vacuum is introduced to the test section. After approximately 10 minutes under vacuum, the test section is purged with high-purity argon (set at about 50 psi coming out of the regulator) while still running the vacuum pump. The pressure is lowered on the argon to 10 psi after the initial purge, and the valve to the vacuum is closed. Once the pressure stabilizes to 10 psi, the loop valve to the argon is closed, isolating the test section with a charge of 10 psi of argon.

Following this procedure, the probe was valved in with no significant O_2 spike. After seven days, no measurable FAC was detected so the flow rate was increased to 0.85 L/min. Within 24 hours, FAC began and over the course of the next few days, a steady rate of 0.14 mm/a was established. Clearly, at pH 9.2 and a flow rate of 0.5 L/min, the FAC rate is too low to measure reliably. Figure 4.1 shows the internal radius of the probe versus time.

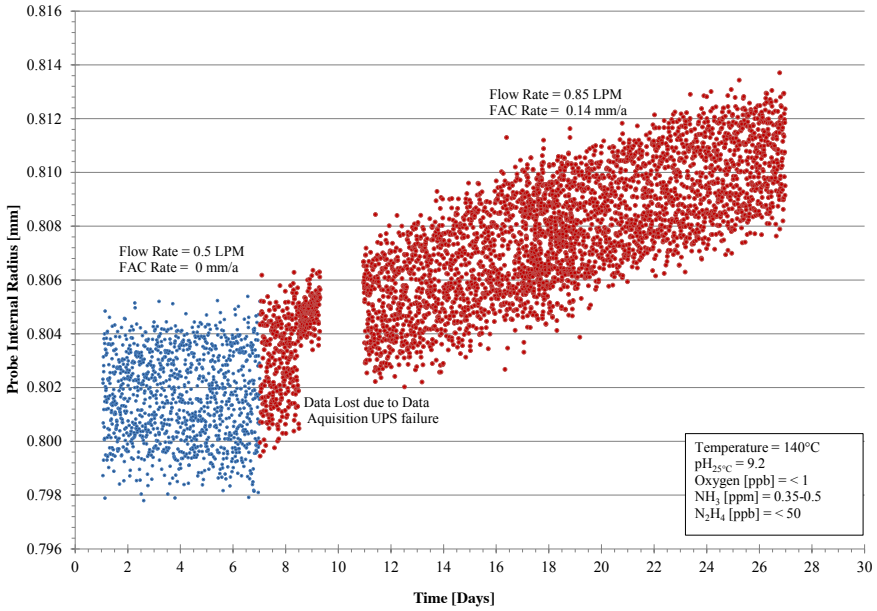

Figure 4.1: Run 1 probe internal radius vs. time

4.1.2 Run 2

Run 1 established a baseline FAC rate for the target conditions in Loop 1. Experiments then began to investigate the effects of bulk iron concentration. The loop was modified as described previously to accept the iron injection system into the test section. Run 2 began with the conditions shown in Table 4.3. This run produced data not only for the effects of an increase in iron concentration, but also for temperature variations from 140°C to 200°C. The results of Run 2 are presented in Table 4.4.

Table 4.3: Run 2: Target chemistry conditions

Parameter	Value
$FlowRate\ [LPM]$	0.85
$Temperature[^{\circ}C]$	140 *to* 200
pH	9.2
$Oxygen\ [ppb]$	< 1
$NH_3\ [ppm]$	$0.35 - 0.5$
$N_2H_4\ [ppb]$	< 50

Table 4.4: Run 2 results with iron concentration and hydrazine variations

Test	Iron	Rate [mm/a]	% Change	Temp [°C]	Avg pH	N_2H_4 [ppb]	O_2 [ppb]
1	N	0.183	60	142.7	9.2	35	0.71
2	Y	0.073		142.1	9.3	26	0.74
3	N	0.292	75	143.0	9.3	14	0.72
4	Y	0.073		142.2	9.3	15	0.67
5	N	0.000	N/A	200.6	9.3	16	0.70
6	N/A[1]	N/A[1]		N/A[1]	N/A[1]	N/A[1]	N/A[1]
7	N	0.256	71	142.9	9.2	7	0.73
8	Y	0.073		142.1	9.3	4	0.68
9	N	0.037	20	200.7	9.3	22	0.72
10	Y	0.029		201.7	9.3	14	0.69

[1] Test was interrupted by power outage

Firstly, note that the FAC rate is consistently reduced by introducing the iron source. At approximately 140°C, there is a reduction in FAC rate of between 60% and 75%. At 200°C, this reduction was only 20%. This may be attributed to the significantly reduced FAC rate at 200°C, which would affect

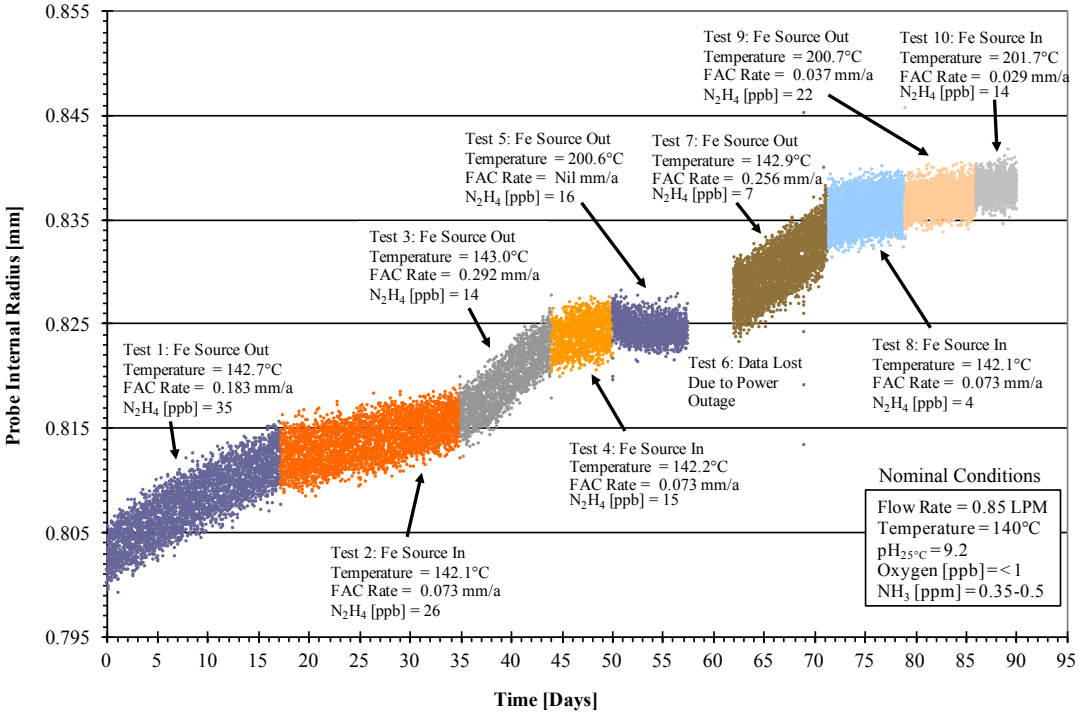

Figure 4.2: Run 2 probe internal radius vs. time

the overall amount of iron being introduced upstream of the measurement probe, as the iron injection device depends on FAC to generate the iron into solution. At this point it was assumed based on simple calculations of metal loss through the iron injection system that the iron concentration was being increased to approximately 80% of saturation at 140°C, since at 100% saturation the driving force for the FAC should, in theory, be eliminated completely.

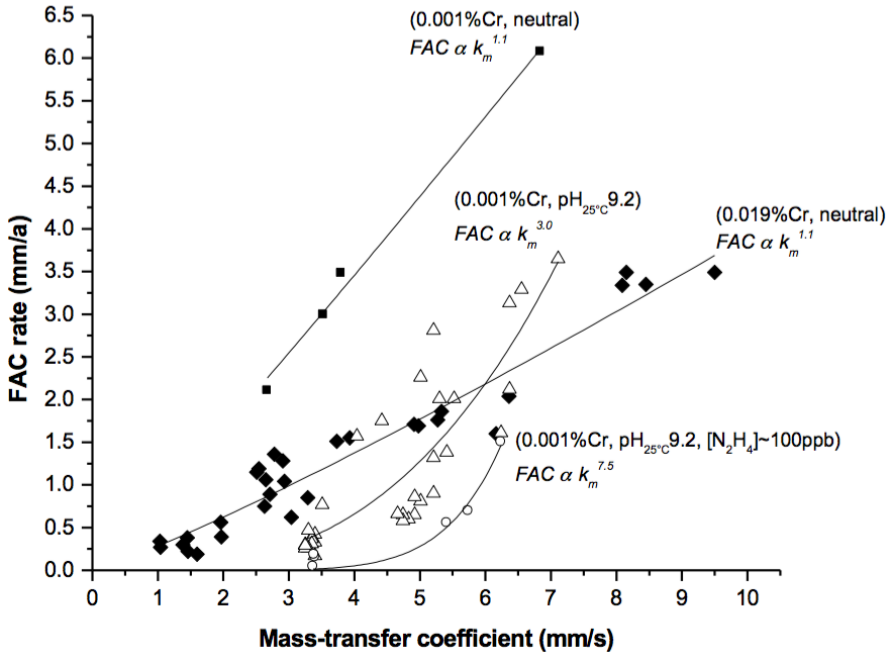

Figure 4.3: Variation of FAC RATE at 140°C, ∼1 ppb O_2, with increase in N_2H_4 from 0 to 100 ppb [5]

Secondly, there appears to be a reduction in FAC rate from the presence of hydrazine as well, since the rates are slightly higher at 140°C when the

hydrazine concentration is below 20 ppb. The current result is consistent with previous UNB Nuclear results, Figure 4.3, but contradicts some previously described responses to hydrazine inclusion in the system chemistry, where there is no influence of hydrazine at 180°C and an increase in FAC rate was seen with increasing hydrazine concentrations at higher temperatures, Figure 4.4 [62].

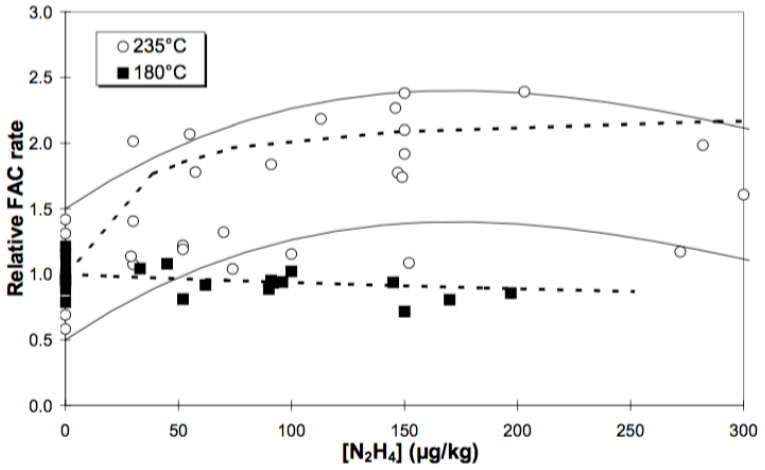

Figure 4.4: Relative FAC rate versus hydrazine concentration for tubular carbon steel specimens exposed to a single-phase flow at 180°C and 235°C at pH25°C = 9.0 [62]

The absence of data from Test 6 in Table 4.4 was due to a two-day power outage that occurred at UNB, during which the loop had to be laid up with the test section purged to minimize damage to the FAC measurement probe. The plot of internal radius versus time is presented in Figure 4.2.

4.1.3 Run 3

The loop was shut down for preventative maintenance and instrument calibration following Run 2. The H^+-OH^- ion exchange column was valved in to bring the water chemistry back to neutral conditions, and the tank was refilled with deionized water. With the addition of the fresh water, oxygen levels increased, consuming any remaining hydrazine in the loop. Run 3 (Table 4.5) repeated the experiment of Run 2, only with no hydrazine addition.

Table 4.5: Run 3: Target chemistry conditions

Parameter	Value
$FlowRate\ [LPM]$	0.85
$Temperature[^{\circ}C]$	140 *to* 200
pH	9.2
$Oxygen\ [ppb]$	< 1
$NH_3\ [ppm]$	$0.35 - 0.5$
$N_2H_4\ [ppb]$	0

Following initial difficulties eliminating excess O_2, the loop chemistry was stabilized and the loop ran smoothly. Control of pH was more difficult than in the previous run. This may be because of the higher overall FAC rates in the absence of hydrazine, resulting in more displacement of NH_4^+ from the ion exchange resin by iron and thus more manipulation of the resin columns to maintain the target pH.

Part-way through Run 3, the Orbisphere oxygen monitor failed, but it was reasoned that, since FAC continued unabated, concentrations stayed below

~1 ppb. This was supported with Chemets dissolved oxygen tests, but the range of the Chemets only provides a 'less than 5 ppb' range.

The results of Run 3 are presented in Figure 4.5 and Table 4.6. Two series of iron effects tests were completed, both at 140°C. Following the second test of the run, a power outage occurred, which resulted in the loop reaching room temperature for two days. Fortunately, FAC resumed almost immediately upon startup.

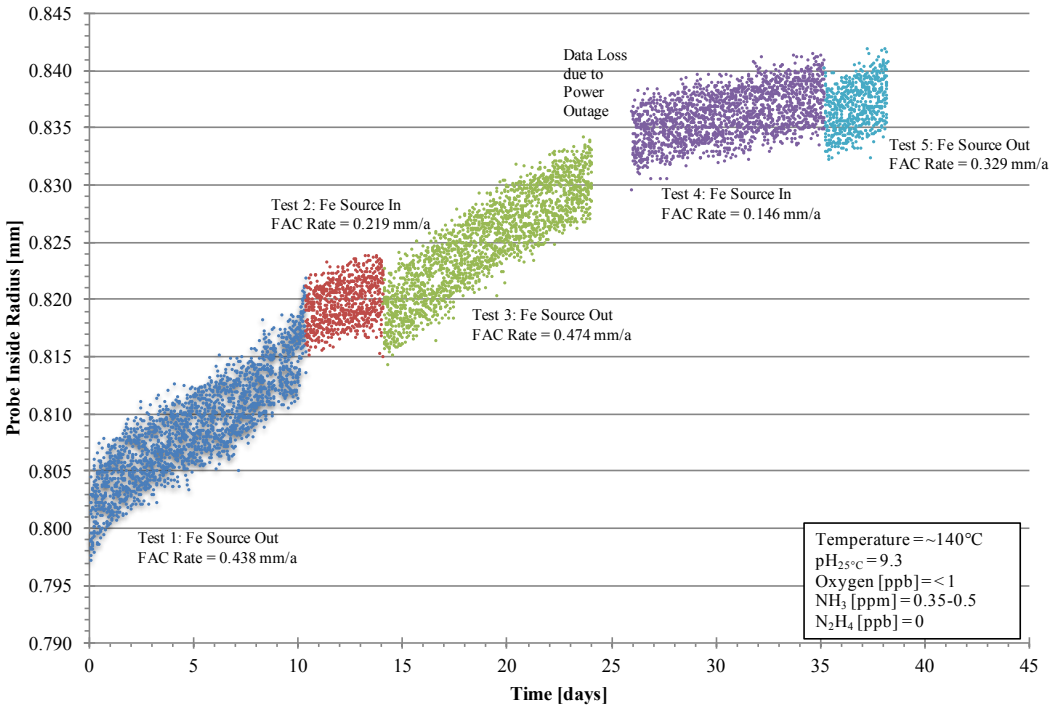

Figure 4.5: Run 3 probe internal radius vs. time

As one can see in Table 4.6, the FAC rates in this run are higher than those

in Run 2, likely because of the absence of hydrazine. The trend of reduction from the increase in iron concentration is very similar at 50%-69%.

Table 4.6: Run 3 results with iron concentration variation and no hydrazine

Test	Iron	Rate [mm/a]	% Change	Temp [°C]	Avg pH	N_2H_4 [ppb]	O_2 [ppb]
1	*N*	0.438	50	140.7	9.3	0	< 1
2	*Y*	0.219		139.8	9.3	0	< 1
3	*N*	0.474	69	140.6	9.3	0	< 1
4	*Y*	0.146		139.5	9.3	0	< 1
5	*N*	0.329	*N/A*	140.6	9.3	0	< 1

Test 6 during Run 3 was used to collect data to investigate a value observed during a parametric study of the EPRI FFA modelling software relating to the model's accounting for temperature influence on FAC rate (See Appendix C for the results of the parametric study). The data from this test are shown in Figure 4.6, and are plotted with outputs from EPRI FFA, the empirical FAC modelling code, and applicable data points from Run 2 in Figure 4.7. As can be seen in Figure 4.7, FFA predicted an unexpected increase in FAC rate at approximately 170°C. The data from the current experiments does not follow this prediction, as was expected. As the particulars of the FFA model algorithm are not known to UNB Nuclear, it is unclear why this occurs.

After approximately 87 days, Run 3 was stopped and after preventative maintenance, the loop was prepared for the next run.

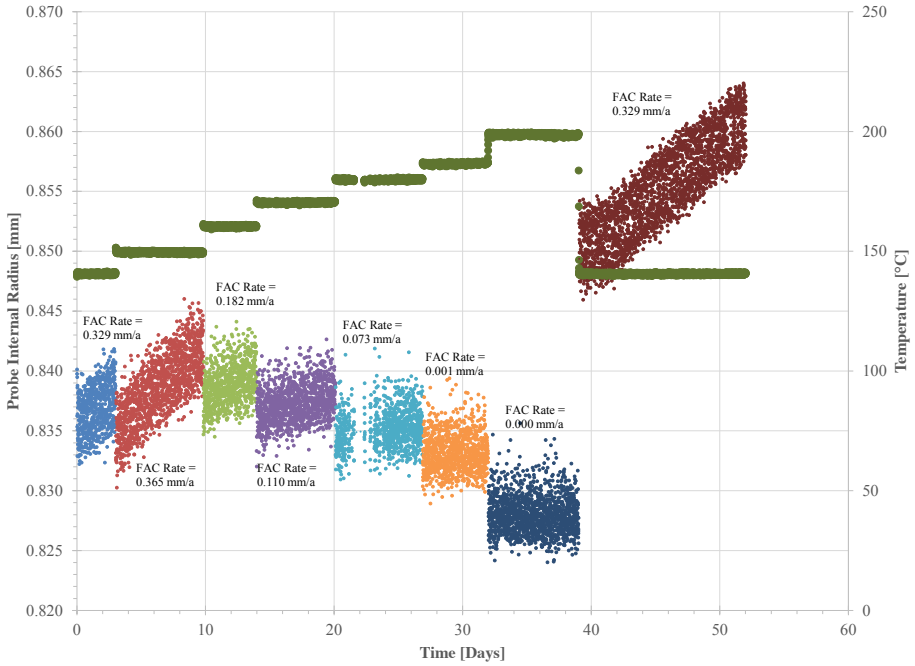

Figure 4.6: Run 3 Test 6: probe internal radius vs. time with variation in temperature from 140°C to 200°C

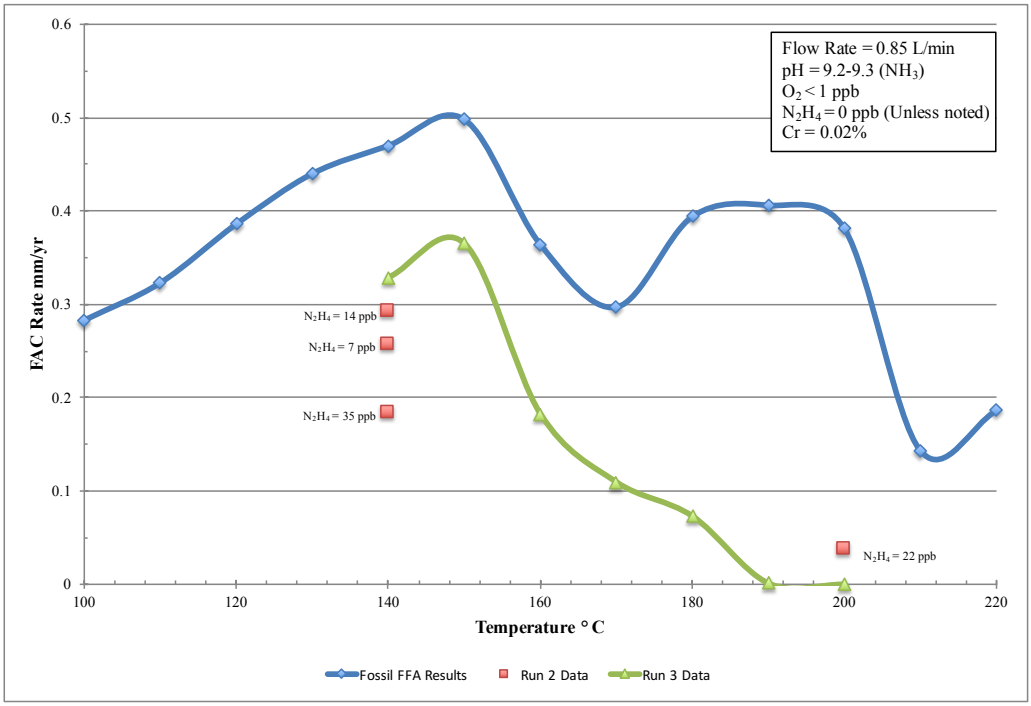

Figure 4.7: FAC rate vs temperature; Fossil FAC Advisor model vs experimental results

4.1.4 Run 4

Run 4 was the investigation of the temperature correlation for measurement probe resistance, as described in Section 3, Temperature Correlation, and will not be presented again here.

4.1.5 Run 5

In parallel with Run 4, preparations were made to begin Run 5, which introduced the sampling system to experiment. This run was the first attempt at measuring a change in concentration of dissolved iron in the bulk solution and its direct, real time effect on FAC rate. The process of obtaining this measurement was described in Section 3.

The run began with the loop chemistry set to neutral conditions (pH $\sim$7). This condition was chosen in order to obtain an upper limit of dissolved iron and to minimize variations due to pH fluctuations from the saturated IX column. Initially, the sampling process worked very well, and the results obtained were considered remarkably accurate. After the first portion of the run, with no iron input, a measured concentration difference of 14.34 ppb was returned from the ICP-ES, compared to 14.15 ppb that was estimated by calculation from measured FAC rates for the same conditions.

The data for Run 5 are presented in Table 4.7 and Figure 4.8. Similar trends

Table 4.7: Run 5 results with iron concentration measured at inlet and outlet of probe

Test	Iron	Sample	Rate [mm/a]	% Change	Temp [°C]	Meas. Fe [ppb] Inlet	Meas. Fe [ppb] Outlet	Flow [LPM]
1	*N*	*N*	0.877	64.9	139.5	17	32	0.5
2	*N*	*Y*	0.804		138.4			
3	*Y*	*N*	0.256		139.6	N/A[1]	109	0.5
4	*Y*	*Y*	0.329		138.8			
5	*N*	*N*	2.740	61.1	142.5	42	74	0.8
6	*N*	*Y*	2.703		140.5			
7	*Y*	*N*	1.023		141.0	94	151	0.8
8	*Y*	*Y*	1.096		140.2			
9	*N*	*N*	0.657	48.8	200.0	89	152	0.8
10	*N*	*Y*	0.621		198.9			
11	*Y*	*N*	0.402		199.1	105	217	0.8
12	*Y*	*Y*	0.256		199.0			
13	*N*	*N*	2.265	N/A[2]	139.9	N/A[2]	N/A[2]	0.8
14	*N*	*Y*	1.790		139.2			

[1] Sample contaminated during collection

[2] Loop experienced mechanical difficulties before finishing Run 5

were observed in the FAC rate response to the change in iron concentration as was seen in Run 3, represented by the % Change column in Table 4.7, indicating the reduction in FAC rate with the change in bulk iron concentration. Minimal change in FAC rate was observed as a result of the sampling process, an indication that temperature control in the experimental apparatus was acceptable. Several issues were encountered with the sampling results. The second set of samples (Test 3-4) were contaminated. Iron concentration was several orders of magnitude above what what expected. This reinforced

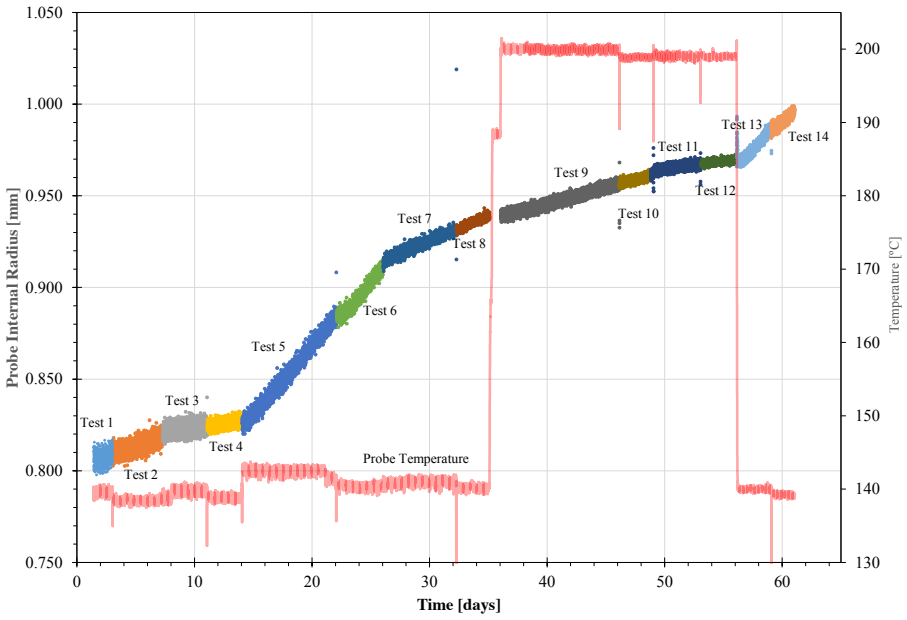

Figure 4.8: Run 5 Probe internal radius vs. time (Refer to Table 4.7 for test conditions)

the need for rigour when handling the samples throughout the collection process (for example, 0.5 mg of Fe introduced to the 500 ml volumetric flask would result in values several orders of magnitude away from the target results). More alarming was the cumulative effect in the supposed baseline iron concentrations without the iron source valved in. These values should have remained constant, within the range of error of the measurement. This led to the hypothesis that the cycle time of the nitric acid solution to recover the samples was not long enough, so it was increased from 10 minutes to 30 minutes. Little improvement was observed. This led to a series of bench tests to examine the cycle time required to strip the iron deposits from the inside of the autoclaves. A grab sample was collected in the autoclaves from the loop per the normal procedure to precipitate iron onto the inside of the autoclave. The first test involved running a 4% solution of HNO_3 through the autoclave, sampling every 30 minutes up to 120 minutes (a more agressive HNO_3 solution was used for this test than for the normal sampling to accelerate the effect). The result of this test showed the iron concentration in the sample was still increasing at the 120 minute mark. A second test ran a 2% HNO_3 through an autoclave with sampling every hour up to 5 hours. This test showed more promising results, with the iron concentration levelling out at around the 4 hour mark. To ensure the iron was sufficiently captured, six hours was chosen as the cycle time.

4.1.6 Runs 6 through 9

The loop was started up and was conditioned for Run 6, a repeat of Run 5 with the revised sampling process, and the test section was valved in. Within several days, a steady FAC rate of approximately 1.0 mm/a was established. Upon valving in the autoclaves, a significant O_2 spike occurred, amounting to an O_2 level >1ppm for several hours. Since the iron-sampling autoclaves were valved in, it was decided to wait to see if FAC would return, as the O_2 spike immediately reduced FAC rates by >75%. After 48 hours, the rate had returned to slightly less than the 1.0 mm/a, so the autoclaves were valved out and sampled. Prior to reinstalling the autoclaves, the O_2 source was found and eliminated.

During the next segment of the run, a pressure transient tripped the loop and ended the run prematurely. An Inconel rupture disk, which acts as over-pressure relief in the autoclaves, failed during pressurization of the sampling system. It is unknown what specific alloy the original rupture disks were made from, but the replacement rupture disks are Inconel 600, which, at room temperature, should be sufficiently resistance to nitric acid to suit the sampling runs. The operational history of the original rupture disks also was not known, so while they were visually inspected as suitable for use, it is possible they were stressed at some point. The pressure transients measured in the loop did not approach the nominal 1845 psi pressure rating of the Inconel 600 disks. Runs 7, 8 and 9 were attempted, but continuing mechanical

problems with the loop were encountered. Pressure transients, sampling oven failures and water leaks took several months to overcome. Given the timeline of the experimental program, further investigation into the sampling system was abandoned for this project.

4.1.7 Run 10

One of the focal points of this research program was to investigate the effects of iron concentration on FAC rates. To validate assumptions made in accounting for iron concentration effects in the mechanistic model, data were required to quantify the effect of varying bulk iron concentrations at different positions down the length of a pipe.

Table 4.8: Run 10: Target chemistry conditions

Parameter	Value
$FlowRate\ [LPM]$	0.5
$Temperature[^{\circ}C]$	140
pH	7.0
$Oxygen\ [ppb]$	< 1
$NH_3\ [ppm]$	0

This was achieved in the loop by substituting sections of the sacrificial iron source (A106B, 0.019% Cr) with sections of 316 stainless steel immune to FAC. This test was conducted at the conditions presented in Table 4.8, results of which are presented in Figure 4.9 and Table 4.9.

Table 4.9: Run 10 results with iron source length variation

Test	Iron	Rate [mm/a]	Temp [°C]	Avg pH	O_2 [ppb]
1	0	0.800	139.6	7	< 1
2	100%	0.330	139.1	7	< 1
3	50%	0.510	139.8	7	< 1

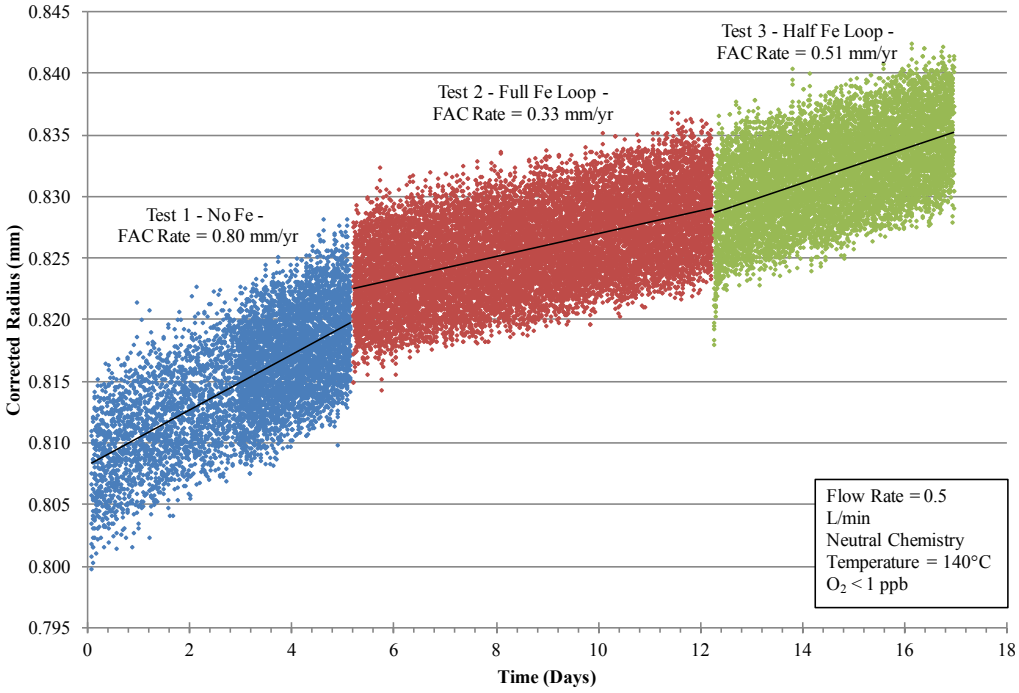

Figure 4.9: Run 10 FAC rate response to varying length of iron injection system (and thus the bulk iron concentration entering the measurement probe).

The results of this run were directly applicable to the mechanistic model, showing the response of the FAC rate to relatively fixed steps in bulk iron

concentration. Repeat tests were planned (including conducting this experiment at elevated pH), but challenges with the loop ended the experimental portion of this work.

Chapter 5

Model Development

5.1 Oxide Structure

The modelling of FAC begins with the assumption of an overall structure of the corroding system. In particular, we assume a structure that exists when FAC is occurring; iron-based metal covered by oxide layers exposed to bulk water that imposes chemically-reducing conditions on the system. Figure 5.1 presents this structure diagrammatically on the right hand side. On the left hand side of Figure 5.1, the processes assumed to be occurring in this structure are shown.

As shown in Figure 5.1, an intermediate layer is assumed to form between the metal surface and the magnetite layer. This so-called passivating layer

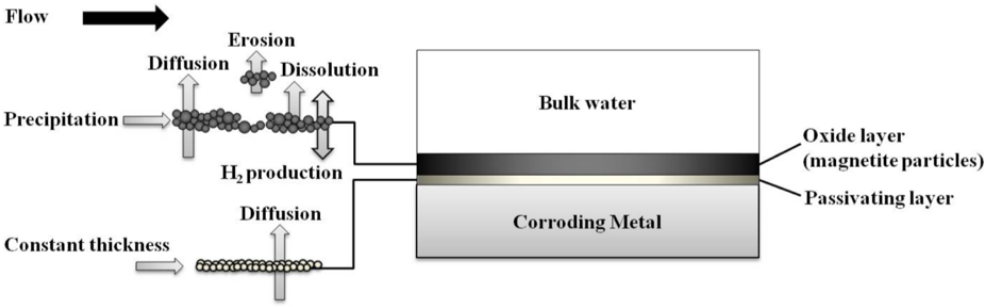

Figure 5.1: Assumed oxide structure for FAC mechanistic model [27]

represents a hypothetical Cr-Fe barrier that forms immediately upon exposure to the coolant at the metal-oxide interface. The purpose of this layer is to account for initial effects arising from variations in material composition of the base steel, in particular the chromium content.

The passivating layer is taken into consideration in the model as an additional diffusional resistance. Therefore, corrosion products (ionic and hydrolyzed iron) must first diffuse through this layer before either forming magnetite at the inner interface of the magnetite oxide (and thus replacing the volume of corroded metal) or diffusing through the already-formed magnetite layer between the passivating layer and the bulk coolant.

The passivating layer is assumed to form immediately based on experimental work indicating that the effects of very low variations in Cr content of the base steel result in a marked reduction in FAC rate upon initial exposure to the coolant [6]. The effect of the increased Cr content has also been observed

as a steady-state effect, meaning the reduction in FAC rate attributed to the Cr concentration persists as wall thinning continues.

There have been contradictory reports on the mechanism of Cr effects on FAC rates. Bignold [21], for example, provided evidence (shown in Figure 5.2) of Cr enrichment at the oxide-coolant interface, presumably formed by the selective dissolution of iron from the Cr-containing magnetite. This is not incompatible with our hypothesis of the Cr-rich passivating layer, but it does suggest that oxide dissolution at the oxide-solution interface, and therefore FAC, would begin to slow down at long exposures, contrary to the assumption of a continual steady-state. This was also pointed out by Bouchacourt (Figure 5.3).

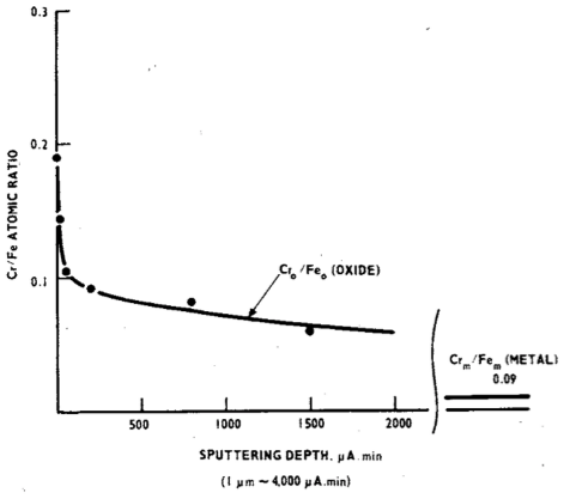

Figure 5.2: Variation of Cr/Fe ratio through the oxide film formed on 1%Cr-1/2%Mo steel at pH 9.30, 148°C[21]

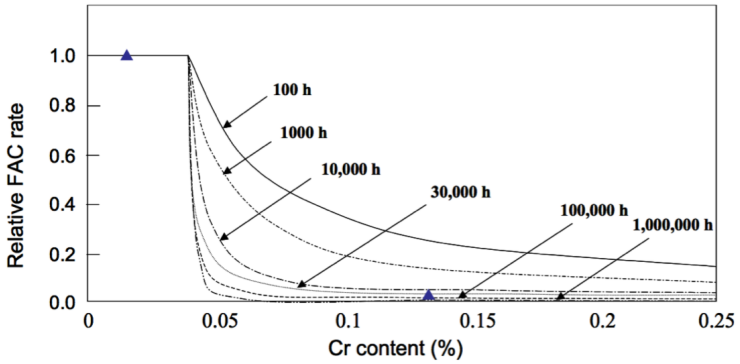

Figure 5.3: Bouchacourt model of Cr effect on FAC rate [8]

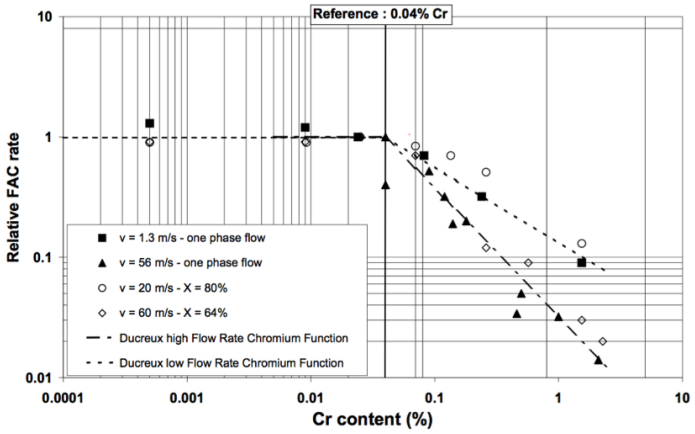

Figure 5.4: Ducreux model of Cr effect on FAC. Relative FAC rate vs Cr content of carbon steel at 180°C (single phase) or 175°C (two-phase) at $pH_{25^\circ\mathrm{C}}$ = 9.0 [63]

Figure 5.4 presents the relative rate of FAC vs Cr content of carbon steel as described by the Ducreux correlation [63]. This correlation, which is often applied in commercial FAC packages [63], [8], sets a threshold value of 0.04% Cr in carbon steel, below which there is no influence of Cr content on FAC rate, with apparent elimination of FAC just above 1%. Note, however, that many later experiments have indicated Cr effects at concentrations of 0.02-0.001% [6].

5.2 Mass Balances

The UNB mechanistic model is based on a mass balance across each interface of the oxide structure. The mass balances at each interface are presented in the following sections.

5.2.1 Metal-Passivating Interface

At the metal-passivating layer interface, the mass balance considers only the diffusional resistance of the layer, and equates to the mass lost at the metal surface with time ($\frac{dm}{dt}$) being equal to the flux of iron and iron products diffusing through the passivating layer:

$$\frac{dm}{dt} = \frac{D_{Fe}\phi_P(C_{M-P} - C_{P-O})}{\frac{\delta_P\zeta_P}{\rho_P(1-\phi_P)}} \tag{5.1}$$

Where:

D_{Fe} = diffusivity of iron in water [cm^2/s]

ϕ_P = passivating layer porosity

C_{M-P} = concentration of iron at the metal-passivating interface [g/cm^3]

C_{P-O} = concentration of iron at the passivating-oxide interface [g/cm^3]

δ_P = thickness of passivating layer [g/cm^2, a function of oxide density]

ζ_P = tortuosity of the passivating layer

ρ_P = density of passivating layer [g/cm^3]

As mentioned before, the passivating layer is assumed to be defined as a fixed thickness, porosity and tortuosity, based on base metal chromium content. In the current model, this results in the passivating layer effect as being a fixed diffusional resistance in the path of corrosion product movement from the metal surface to the bulk coolant. The quantitative measurements of individual parameters of porosity and tortuosity, and their individual relation to chromium content are not available at this time. The current research program considered a single chromium value, 0.019%, for which data was generated within this experimental program. Further experimental investigation is necessary to specifically determine values for these variables. As such, a value of 0.2 and 1.8 were assumed for the passivating layer porosity and tortuosity, respectively, which provided a reasonable diffusive resistance and resulted in a good fit of the model to the data. A porosity value of 0.2 is relatively high, and it could be reasoned that as the chromium content increased, the porosity of the layer would be reduced, leading to a reduced

rate of diffusion and lower FAC rate.

5.2.2 Passivating-Oxide Interface

After diffusing through the passivating layer, the corrosion products encounter two processes at the passivating-oxide interface. The first is the formation of magnetite via the Schikorr reaction to fill the volume of corroded base metal, shown by the term on the left of Equation 5.2. The second process is the diffusional resistance on the right hand side of Equation 5.2, much like that described for the metal passivating-layer previously, only in this case the thickness of the oxide layer will vary throughout the corrosion process, with an average value at steady-state FAC rates.

$$0.476\frac{dm}{dt}(1.101+\phi_{OX}) = \frac{D_{Fe}\phi_{OX}(C_{P-O}-C_{O-B})}{\frac{\delta_{OX}\zeta_{OX}}{\rho_{OX}(1-\phi_{OX})}} \tag{5.2}$$

Where:

D_{Fe} = diffusivity of iron in water [cm^2/s]

ϕ_{OX} = oxide layer porosity

C_{P-O} = concentration of iron at the passivating-oxide interface [g/cm^3]

C_{O-B} = concentration of iron at the oxide-bulk interface [g/cm^3]

δ_{OX} = thickness of oxide layer [g/cm^2]

ζ_{OX} = tortuosity of the oxide layer

ρ_{OX} = density of oxide layer [g/cm^3]

5.2.3 Oxide-Solution Interface

The final interface considered in the model is where the oxide layer meets the flowing fluid in the system. At this point, there are three processes occurring in parallel that impact the rate of FAC. A mass balance at this interface accounts for the mass transfer, as $k_m(C_{O-B} - C_B)$, outward diffusion of iron species, as $0.476\frac{dm}{dt}(1.101+\phi_{OX})$, and finally the dissolution of the magnetite, $k_d F^*(SC^{Sat}_{O-B} - C_{O-B})$, resulting in Equation 5.3.

$$k_m(C_{O-B} - C_B) = 0.476\frac{dm}{dt}(1.101 + \phi_{OX}) + k_d F^*(SC^{Sat}_{O-B} - C_{O-B}) \quad (5.3)$$

Where:

k_m = mass transfer coefficient [cm/s]

C_b = bulk iron concentration [g/cm^3]

k_d = dissolution rate constant [cm/s]

F^* = surface area factor = 1.732

S = super-saturation factor = 1.1

C^{Sat}_{O-B} = solubility at the oxide-bulk interface [g/cm^3]

The processes occurring at this interface would be considered to be the controlling aspects of the overall FAC mechanism, as they will have the greatest impact on the rate at which the reaction at the metal surface can occur.

5.3 Final Equations

In the following sections, the fundamental equations applied in the model are presented.

5.3.1 Mass-Loss Rate

Based on the previously discussed mass balances, Equations 5.1, 5.2 and 5.3 are combined and rearranged to solve for the metal loss rate, $\frac{dm}{dt}$, which is the loss of base metal in $[g/cm^2]$ per unit time $[s]$, given as Equation 5.4.

$$\frac{dm}{dt} = \frac{C_{M-P} - \left(\frac{k_d F^* S C_{O-B}^{Sat} + k_m C_b}{k_d F^* + k_m}\right)}{\frac{\delta_P \zeta_P}{\phi_P D_{Fe} \rho_P (1-\phi_P)} + \frac{0.467(1.101+\phi_{OX})\delta_{OX}\zeta_{OX}}{\phi_{OX} D_{Fe} \rho_{OX} (1-\phi_{OX})} + \frac{0.467(1.101+\phi_{OX})}{k_d F^* + k_m}} \tag{5.4}$$

This equation is an updated derivation of that previously presented by Phromwong [64]. Whereas the previous iteration of the model applied interface iron solubilities to formulate the driving force for diffusion through the oxide layers, the current model presented in Equation 5.4 uses the calculated iron concentration at the metal-passivating layer to drive the diffusion of species to the oxide-bulk interface where mass transfer to the bulk coolant occurs.

5.3.2 Oxide Thickness

In order to predict the metal loss rate, the thickness of the oxide layer must also be determined. A mass balance of the inner oxide layer results in Equation 5.5. The terms represent the inner oxide layer growth on the left hand side, with the difference of precipitation and dissolution on the right.

$$0.723\frac{d\delta_i}{dt} = 0.476\frac{dm}{dt}(1-\phi_{OX}) - k_d F^*(SC^{Sat}_{O-B} - C_{O-B}) \qquad (5.5)$$

This will enable the calculation, at each time step, of the change in oxide layer thickness, $\frac{d\delta_i}{dt}$, as a result of the metal loss at that time step determined by Equation 5.4. Only the inner oxide layer has been considered here, as the presence of an outer oxide layer would indicate that there is an oversaturation of iron in the bulk coolant, and FAC would not be occurring.

5.3.3 Spalling

A feature that is unique to the UNB mechanistic model is the inclusion of oxide particle removal in the calculation at each time step. The sudden removal of discrete particles of oxide allows the model to take into account subtle variations in flow effects and oxide morphology from one condition to the next. It is postulated that the continuous dissolution of the magnetite loosens the particles and makes them easier to be spalled/removed.

At each time step, a random-number generator selects an oxide particle diameter based on a half-normal distribution bound by the smallest assumed crystallite (10 nm) to half the thickness of the oxide film at that time step [25].

The calculation to determine spalling time, t_{sp}, is then carried out at the time step, where a decision is made based on the total simulation time. If the value calculated for the time it will take for a particularly sized oxide particle to be removed is less than the simulation time since the last spalling event, then the the spalling event will occur, and the oxide thickness will be reduced by the size of the oxide particle.

To determine the spalling time, Phromwong [27] considered that spalling time was proportional to particle diameter squared, and inversely proportional to fluid shear stress at the wall, oxide porosity as well as the overall dissolution rate of the oxide layer. This is represented as Equation 5.6[26]. Subtle variations in oxide morphology due to specific conditions are accounted for with a spalling factor, k_{sp}, which is discussed in more detail in the next chapter.

$$t_{sp} = \frac{k_{sp} d^2}{\tau \phi_{OX} k_d F^* (C_{O-B}^{Sat} - C_{O-B})} \tag{5.6}$$

Where:

t_{sp} = spalling time [s]

k_{sp} = spalling time factor

d = oxide particle diameter [cm]

τ = shear stress at the pipe wall [N/cm]

ϕ_{OX} = oxide porosity

k_d = dissolution rate constant [cm/s]

F^* = surface area factor = 1.732

C_{O-B}^{Sat} = solubility at the oxide-bulk interface [g/cm^3]

C_{O-B} = concentration of iron at the oxide-bulk interface [g/cm^3]

Several authors have questioned the applicability of wall shear stress to the prediction of FAC ([65] and [66]). In this work, the use of wall shear stress, τ, has been reevaluated as a means of determining spalling time. As noted in Section 2, wall shear stresses may not be of sufficient magnitude to remove oxide particles. In any case, the intention of the spalling time function was to provide a proportionality between spalling events and the fluid behaviour. Here, rather than using wall shear stress, it is proposed that the mass transfer rate may be a more suitable measure of the intensity of the mechanisms leading to an increase in oxide removal. As shown in Figure 5.5, the relative shape of both the turbulence and mass transfer profiles follow the shape of the corrosion much more closely than the shear stress profile.

Here the hydrodynamic characteristic of the flow is represented by using the Sherwood number in Equation 5.6 to give Equation 5.7

$$t_{sp} = \frac{k_{sp} d^2}{Sh \phi_{OX} k_d F^* (C_{O-B}^{Sat} - C_{O-B})} \tag{5.7}$$

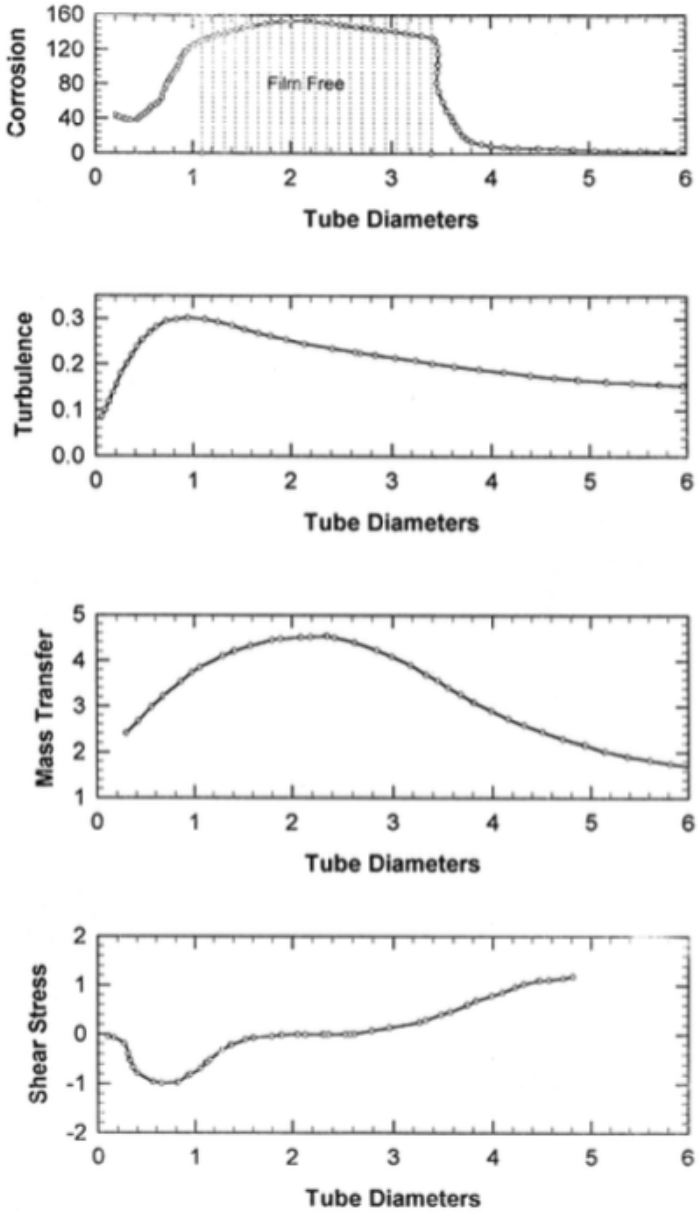

Figure 5.5: Variation of corrosion rate and various hydrodynamic parameters downstream of a flow expansion [65]

This has led to an effective means of increasing resolution of FAC rate prediction where subtle variations in mass transfer are seen in applications where complex geometry must be analyzed.

5.3.4 Iron Effects

The driving force behind the transfer processes controlling the rate of FAC is the difference in iron concentration across the interfaces of the oxide structure and into the bulk coolant.

In the basic form of the FAC rate calculation, $R = K\Delta C$, the ΔC term is considered to be the difference between the solubility of iron species at the condition of interest and the existing concentration of iron species in the bulk coolant. As was observed in the wall thinning as a result of FAC of outlet feeder pipes in CANDU reactors [25], the primary factor leading to FAC in this system was an under-saturation of iron in the coolant as it left the reactor, due to a constant bulk iron concentration entering the system and an increasing solubility as the temperature increased across the reactor core.

The model already takes bulk iron concentrations into account through the basic equations and mass balances, but the calculations are often overly conservative. In effect, the calculated concentration differences produce too high a driving force to realistically model FAC. Thus, at each time-step in

the model, Equation 5.3 is rearranged to solve for a new value of the surface concentration at the oxide-bulk interface, as expressed in Equation 5.8.

$$C_{O-B} = \frac{0.476\frac{dm}{dt}(1.101 + \phi_{OX}) + k_d F^*(SC_{O-B}^{Sat}) + k_m(C_B)}{k_m + k_d F^*} \tag{5.8}$$

When calculating in the computer code, a factor of 0.5 is applied to the C_B term in the numerator of Equation 5.8. The introduction of this term is intended to average the surface concentration due to the effects of spalling events. In the one-dimensional model, as an individual particle of oxide is removed, the surface concentration at the fresh, exposed oxide could reasonably be assumed to be equal to the bulk concentration, C_B, and with time would increase to the surface concentration of the surrounding oxide. At that instant of particle removal, the concentration difference would effectively be zero, and as the surface concentration increases as FAC and dissolution continue, that concentration difference (the driving force for the processes occurring at the oxide-bulk interface) would increase until another spalling event occurs.

5.4 Electrochemistry

The UNB mechanistic model incorporates the effects of the electrochemical processes occurring at each interface of the metal/oxide/coolant structure.

While more macro-scale processes (mass-transfer and spalling) influence the rate of FAC, the underlying kinetics of the reactions occurring at each interface are governed by the electrochemical reactions. Thus, at each time step, electrochemical potentials, iron species solubilities and concentrations and hydrogen concentrations are determined through electrochemical calculations. The electrochemical treatment applied by the UNB model has been incorporated as presented by Lang [37] and Phromwong [27]. It is assumed that the electrochemical processes involved in the mechanism of FAC follow Butler-Volmer kinetics, represented in Figure 5.6 [27] and as per Equation 5.9. Equation 5.9 gives the current produced by an electrochemical reaction as a function of electrochemical potential.

$$i = i_0 \left\{ exp\left[\frac{\beta nF}{RT}(E_0 - E_{eq}) \right] - exp\left[-\frac{(1-\beta)nF}{RT}(E_0 - E_{eq}) \right] \right\} \qquad (5.9)$$

Where:

i = current of reaction [A]

i_0 = exchange current [A]

β = symmetry factor

n = number of electrons passed in the reaction

F = Faraday constant = 96485 [C/mol]

R = Universal Gas Constant = 8.314 [J/mol*K]

T = temperature [K]

E_0 = standard potential of the reaction [V]

E_{eq} = equilibrium potential of the reaction [V]

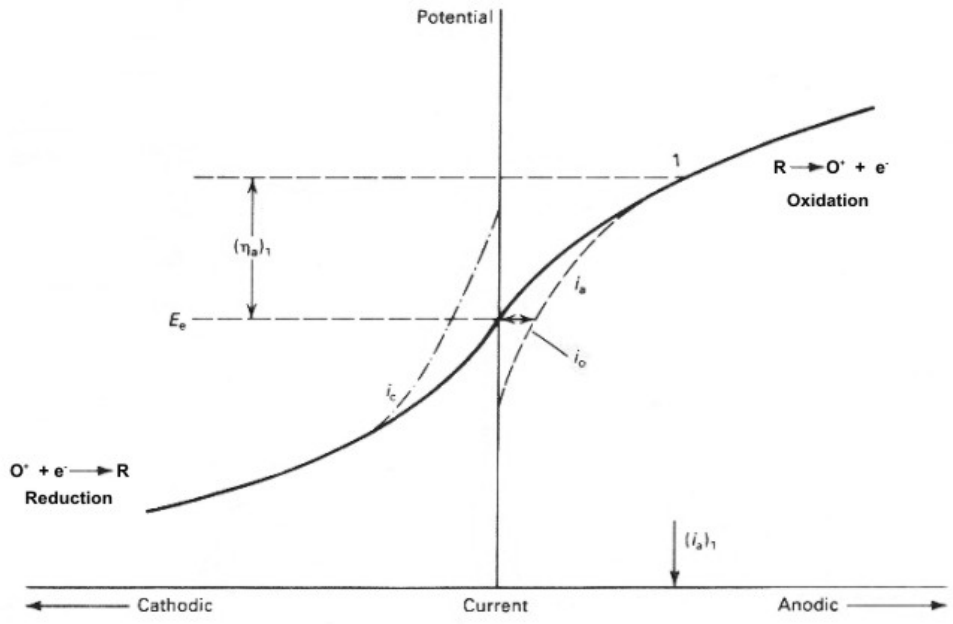

Figure 5.6: Butler-Volmer plot relating electrochemical potential to current

For a given half-cell reaction the Butler-Volmer curve represents the forward and reverse processes (with respect to the current topic, the dissolution (anodic) and deposition (cathodic) of iron) that occur. As the potential shifts from the equilibrium value the current increases along the curve in either direction depending on whether the actual potential is greater or less than the equilibrium potential. Each interface half-cell reaction is written in the reduction form of Equation 5.10 and applied to the Nernst Equation (Equation

5.11) to calculate the equilibrium potential at the temperature of interest:

$$O^{n+} + ne^- \rightarrow R \tag{5.10}$$

$$E_{eq} = E^\circ - \frac{RT}{nF} ln\left(\frac{a_{reduced}}{a_{oxidized}}\right) \tag{5.11}$$

Where:

E_{eq} = equilibrium potential of the reaction [V]

E_0 = standard potential of the reaction [V]

R = Universal Gas Constant = 8.314 [J/mol*K]

T = temperature [K]

n = number of electrons passed in the reaction

F = Faraday constant = 96485 [C/mol]

$a_{oxidized}$ and $a_{reduced}$ = activities of species of interest

E_0, is given by Equation 5.12 using the appropriate Gibbs Energy of Formation (ΔG_F°)(values from [67] and [68]):

$$E^0 = \frac{-\Delta G_F^\circ}{nF} \tag{5.12}$$

The exchange current, i_0, is then calculated using Equation 5.13 [69] for each interface in the system. It represents the current passed between the anodic and cathodic reactions occurring at equilibrium, with a net current flow of

zero in the system.

$$i_0 = \frac{Fk_BT}{h} C_0 exp\left(\frac{-\Delta G_{Act}}{RT}\right) exp\left(\frac{-\beta nF}{RT} E_{eq}\right) \tag{5.13}$$

Where:

k_B = Boltzmann constant, $1.38x10^{-23}$ [J/K]

h = Planck's constant ($3.99x10^{-34}$ [J*s/mol]

C_0 = concentration of the charge changing species $[mol/cm^2]$

ΔG_{Act} = Activation energy for the reaction [J/mol]

Finally, the mixed potential at each interface is calculated:

$$E_{mixed} = \frac{RT}{2nF\beta} ln \left(\frac{i_{0A} exp\left(\frac{\beta nF}{RT} E_A\right) + i_{0C} exp\left(\frac{\beta nF}{RT} E_C\right)}{i_{0A} exp\left(\frac{-(1-\beta)nF}{RT} E_A\right) + i_{0C} exp\left(\frac{-(1-\beta)nF}{RT} E_C\right)} \right) \tag{5.14}$$

Where:

i_{0A} and i_{0C} = anodic and cathodic exchange currents from 5.13 [J/K]

E_A and E_C = Over-potentials of the anodic and cathodic reactions [V]

Faraday's Law (Equation 5.15) relates $\frac{dm}{dt}$ to current, thus allowing the re-

calculation of critical variables used in the model.

$$i = \frac{nF}{MW}\left(\frac{dm}{dt}\right) \tag{5.15}$$

Where:

i = corrosion current, [A]

n = number of electrons transferred

F = Faraday constant = 96485 [C/mol]

MW = molecular weight of species of interest [g/mol]

Based on the mixed potential calculated at the oxide-bulk interface, E^{OB}_{mixed}, the corresponding dissolution rate constant is adjusted to a new value using Equation 5.16 [27].

$$k^e_d = k_d exp\big(\frac{\beta nF E^{OB}_{mixed}}{RT}\big) \tag{5.16}$$

By employing the above electrochemical calculations, at each time step oxide dissolution rate as well as interface concentrations and iron solubilities are determined and adjusted for inclusion in Equations 5.4 and 5.5. For each iteration of the model calculation, the electrochemical adjustment begins by calculating the concentration of hydrogen at each interface. The diffusivity of hydrogen gas at the temperature of interest is first calculated using Equation 5.17[70].

$$D_{H_2} = 2.22 * 10^{-5} T\big(exp\frac{-12400}{RT}\big) \tag{5.17}$$

The mass transfer of hydrogen is then calculated with the result of Equation 5.17 by relating the overall mass transfer, k_m, to the ratio of diffusivities of hydrogen and iron. This acts as the limiting current in the electrochemical calculations by limiting the transfer of hydrogen to the bulk coolant by mass transfer.

$$k_{m_{H_2}} = k_m \frac{D_{H_2}}{D_{Fe}} \tag{5.18}$$

Hydrogen generation at the metal surface as given by Johari [35] is equal to:

$$H_2 \text{ generated} = 5.66 * 10^{-3} \frac{dm}{dt}(7.32 - \phi) \tag{5.19}$$

There is evidence [71], [72] that at 300°C, ∼100% of the hydrogen corresponding to the iron oxidation to Fe^{2+} diffuses into the metal and escapes, while only that corresponding to the further oxidation to magnetite diffuses towards the solution.

The hydrogen transport at the conditions considered here is being investigated in a research program at UNB Nuclear; pending the results of that program, it has been assumed that 10% of the hydrogen generated at the metal-passivating layer will diffuse immediately through the thin passivating layer, with the remainder diffusing through the pipe wall. The concentration at the passivating-oxide layer is assumed to be the same as at the metal-passivating layer for the purpose of electrochemical calculations. Thus, the amount of hydrogen generated at the metal-passivating interface, Equation

5.19, is set equal to the diffusion of hydrogen through the oxide layer, based on the equation given by Lister [25]:

$$0.1 * 5.66 * 10^{-3} \frac{dm}{dt}(7.32 - \phi) = \frac{D_{H_2}\phi_{ox}(C_{H_2}^{MP} - C_{H_2}^{OB})}{\frac{\delta_{OX}\zeta_{OX}}{\rho_{OX}(1-\phi_{OX})}} \tag{5.20}$$

Where:

$C_{H_2}^{MP}$ = Concentration of hydrogen at the metal-passivating interface, [mol/L]

$C_{H_2}^{OB}$ = Concentration of hydrogen at the oxide-bulk interface, [mol/L]

Equation 5.21 describes the mass transfer of hydrogen from the oxide-bulk interface into the bulk coolant.

$$h_{H_2}(C_{H_2}^{OB} - C_{H_2}^{B}) = 0.1 * 5.66 * 10^{-3} \frac{dm}{dt}(7.32 - \phi_{OX}) \tag{5.21}$$

Where:

$C_{H_2}^{B}$ = Concentration of hydrogen in the bulk coolant, [mol/L]

$C_{H_2}^{O-B}$ = Concentration of hydrogen at the oxide-bulk interface, [mol/L]

Rearranging Equation 5.20 and Equation 5.21 gives the hydrogen concentrations at the oxide-bulk interface and the metal-passivating/passivating-oxide

interface:

$$C_{H_2}^{OB} = \frac{0.1 * 5.66 * 10^{-3} \frac{dm}{dt}(7.32 - \phi)}{h_{H_2}} + C_{H_2}^{B} \tag{5.22}$$

And:

$$C_{H_2}^{MP} = C_{H_2}^{B} + \frac{0.1 * 5.66 * 10^{-3} \frac{dm}{dt}(7.32 - \phi)\left[\frac{h_{H_2}\delta_{OX}\zeta_{OX}}{\rho_{OX}(1-\phi_{OX})} + D_{H_2}\right]}{D_{H_2} h_{H_2} \phi_{OX}} \tag{5.23}$$

Certain assumptions were made to the electrochemical adjustments incorporated in this model to produce suitable outputs from the computer code. The activation energies used in the calculation of the exchange current were calculated from assumed values of potential and current. Values for Gibbs energies used in in the calculation of the equilibrium potentials also required adjustment from calculated values, possibly due to the sensitivity of the computer code. The construction of the assumed interfaces in the computer code establishes a complex interaction between the thermodynamic parameters for the reactions occurring at each side of the passivating layer. Calculated values of Gibbs energies would result in an inability of the code to converge on a final value. Those points being considered, the model is capable of reasonably adjusting the electrochemical parameters to anticipated values through the iterative process employed.

The electrochemical reactions assumed at each interface are:

At the metal-passivating interface:

$$Fe^{2+} + 2e^- \rightleftharpoons Fe \tag{5.24}$$

and:

$$2H^+ + 2e^- \rightleftharpoons H_2 \tag{5.25}$$

At the passivating-oxide interface:

$$2H^+ + 2e^- \rightleftharpoons H_2 \tag{5.26}$$

and:

$$Fe_3O_4 + 2H_2O + 2H^+ + 2e^- \rightleftharpoons 3Fe(OH)_2 \tag{5.27}$$

And at the oxide-bulk interface:

$$Fe_3O_4 + 2H_2O + 2H^+ + 2e^- \rightleftharpoons 3Fe(OH)_2 \tag{5.28}$$

$$2H^+ + 2e^- \rightleftharpoons H_2 \tag{5.29}$$

It has been assumed that the dissolution of Fe_3O_4, Equation 5.28 is the reverse of the Schikkor reaction occurring at the passivating-oxide interface describing the formation of Fe_3O_4, Equation 5.27. At the conditions of interest (generally neutral to high pH, and temperatures above 140 °C), it is considered to be a reasonable assumption for the purposes of the current

FAC model.

5.5 Model Computation

The UNB model has previously been applied by coding the equations into either the C or Visual Basic coding languages. For convenience, the entire model was re-coded and re-validated using the Python scripting language (see Appendix A for the Python computer code used here).

The overall flow of the computer code to solve the model equations that have been presented is shown in Figure 5.7. As shown, the model is more or less a linear calculation with a single looped section which iterates the FAC rate, oxide thickness, spalling and electrochemical calculations over a specified interval to determine an average rate and oxide thickness at a specific point of interest.

The model can easily be applied to 2D or 3D situations by building a nodal arrangement with this general logic as a nested function (effectively, one of these calculation loops per node).

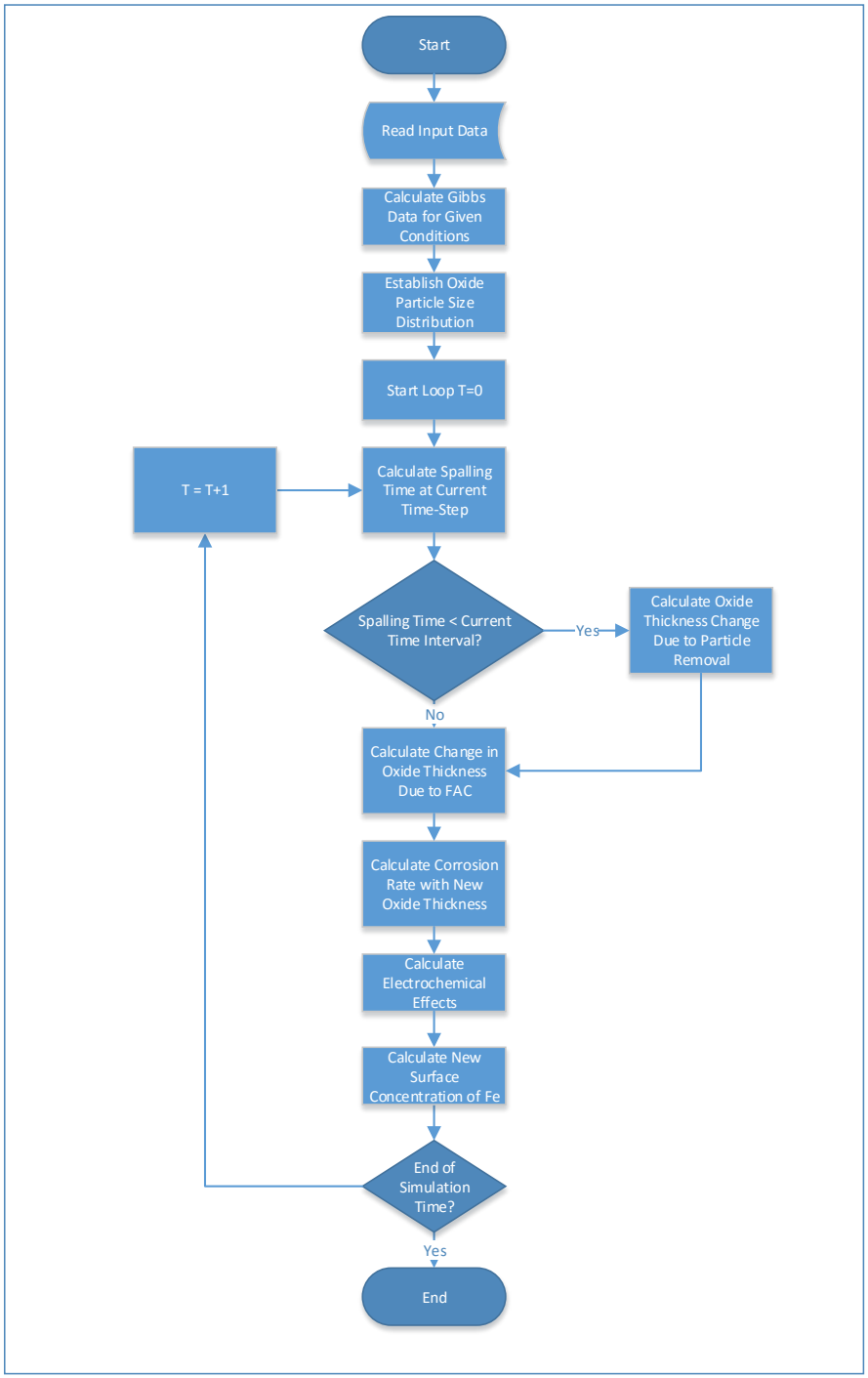

Figure 5.7: Basic logic diagram for UNB mechanistic model computation

Chapter 6

Discussion

A major focus of this program was to investigate the effects of changes in bulk iron concentration on FAC and to assess the ability of the UNB mechanistic model to predict these effects. As was discussed previously, the equation Rate = KΔC was found to be too simple to account for the observed experimental results. The assumption of a simple driving force based on the under saturation of the coolant in dissolved iron provides an approximation of the effect, but not a distinct mechanism that enables accurate prediction. The experiments completed in this work covered a range of conditions while investigating the effect of iron concentration; pH, flow, temperature and oxidizing agents. At 140°C, at both pH $\sim$7 and $\sim$9.2, the reduction in FAC rate as a result of valving in the iron source falls within the range of 50% to 75%. When the temperature is increased to 200°C, this reduction due to the

iron source falls to ∼20%.

In some cases, the mechanistic model is able to produce a reasonable fit to experimental results. For example, at a flow rate of 0.85 LPM, pH 9.2 and 140°C, the FAC rate was measured at 0.438 mm/a without iron input, and 0.219 mm/a with iron input. Using the model with these parameters, and assuming 80% of saturation, the model predicts a drop from 0.44 mm/a to 0.20 mm/a.

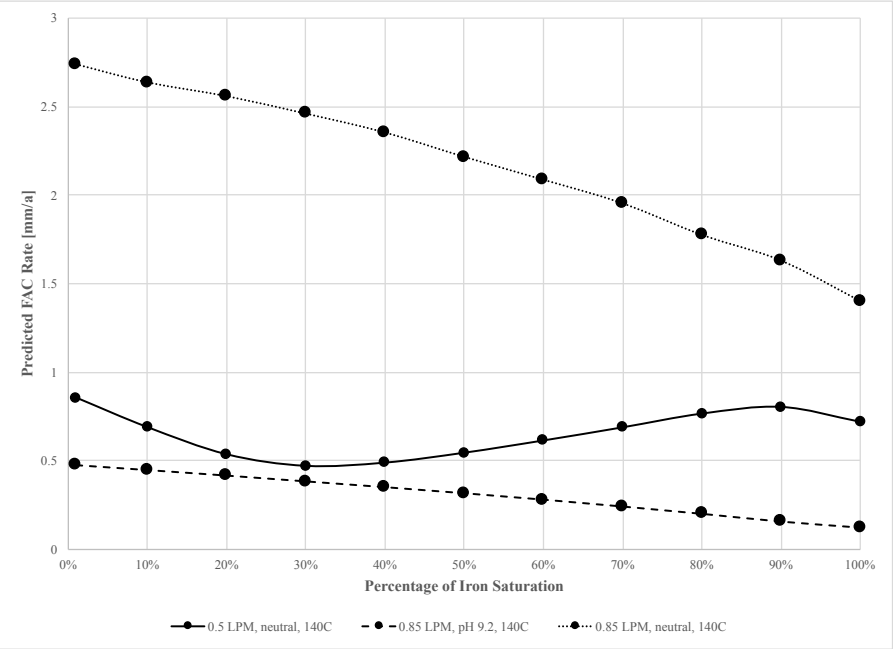

Figure 6.1: Predicted FAC rate response to increasing iron concentration as a percentage of saturation concentration

Unfortunately, as mentioned previously, the mechanisms describing the behavior of FAC at one condition may not necessarily be applicable to all conditions. As can be seen in Figure 6.1, while the rate of FAC responds very well to increasing iron concentration for ammoniated and neutral conditions at 140°C and a flow rate of 0.85 LPM, for neutral conditions at that temperature with a flow rate of 0.5 LPM the FAC rate increases with increasing bulk iron concentration above about 30% of the saturation concentration. In this case, mass transfer may become the rate limiting step in the process due to the lower flow velocity, thus reaching a limit to the current capabilities of the model as presented.

Nevertheless, where high mass transfer rates are present, through modifications to the model in the calculation of the surface concentration of iron, a reasonable fit to Run 10 experimental FAC rates was obtained, as shown in Figure 6.2.

The model predictions in Figure 6.2 were generated by manipulating the value of C_b that was input into the model for calculation. It was assumed that the only value to change along the length of the tube was the bulk iron concentration. The FAC rate data from Run 10 were plotted and a curve was fitted along the length of the probe. For this case, the probe length was taken as the total length of tube upstream of the measured section, so at the entry to the probe, the iron loop was valved out, at mid-way, half the iron probe was in-line, and the outlet of the probe was taken as the full iron loop

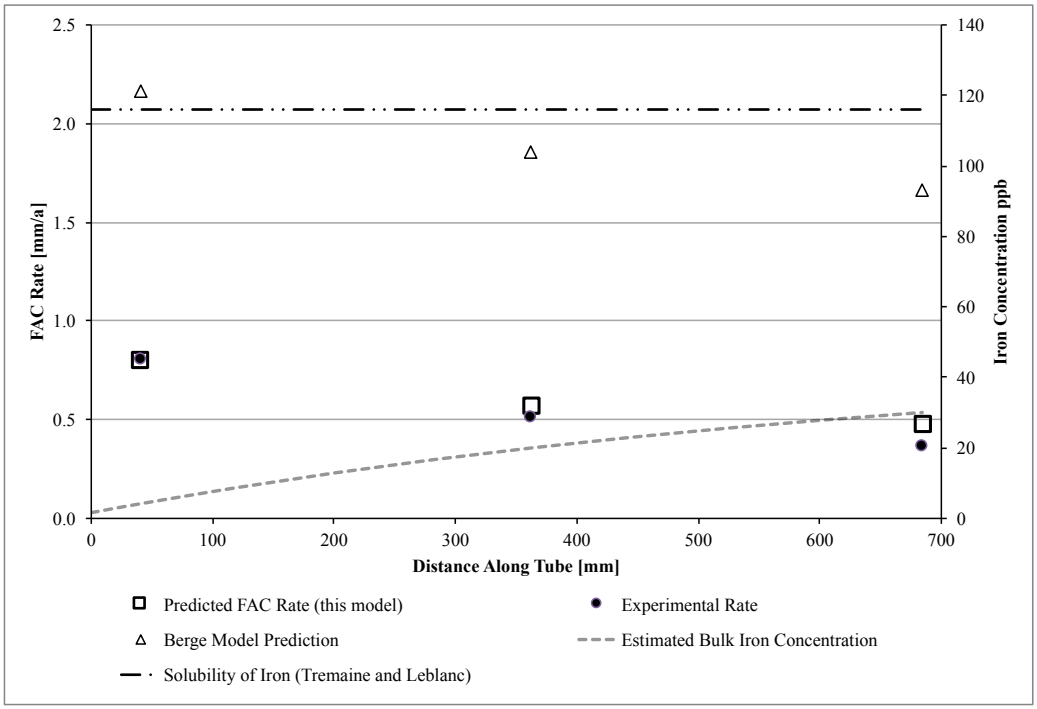

Figure 6.2: Measured and predicted FAC rates with variations in bulk iron concentration

being in-line. The fitted curve was then used to calculate nominal FAC rates along the entire length of the iron loop, and based on these rates, iron input from each section was estimated, as shown in Table 6.1. The estimate of C_b was made by assuming that, at steady state, the metal loss rate, varying linearly along the tube length, in g/cm^2, was equal to the iron input to the coolant.

Probe Distance [mm]	Calculated FAC Rate [mm/a]	Calculated C_b [ppb]
0	0.844	1.64
40.25	0.801	4.14
120.75	0.718	8.75
201.25	0.642	12.89
281.75	0.573	16.59
362.25	0.511	19.88
442.75	0.455	22.82
523.25	0.405	25.44
603.75	0.362	27.77
684.25	0.325	29.86

Table 6.1: Calculated values for modelling iron effect

The assumed entering concentration was taken as $1.64 * 10^{-9} g/cm^3$, or 1.64 ppb, which is considered a reasonable initial concentration given the material composition of the experimental loop. Further development of the model will be necessary in this respect, as a lack of specific data to support manipulation of the mechanisms was limiting. The experimental results show a somewhat linear trend of FAC rate with length of tube, but due to the arrangement of the experimental apparatus, the input of iron from the iron injection device may not necessarily follow a linear trend.

That being said, the iron input loop was disassembled following a number of runs in the experiment. The conditions that the probes had been exposed to varied extensively in temperature, pH and flow rate, so it would be difficult to draw quantitative conclusions from this data. The inlet and outlet diameters of each of the eight sections of the loop were measured by placing the probe in a fixture and photographing the end with a reference for scale adjacent to it. The inlet diameters were for information only, as the substantial flow disturbance from the right-angle fittings on the probes would negate any reasonable correlation from probe to probe. The outlet diameters however, should reasonably represent the trend along the length of the tube.

The outlet diameters are plotted in Figure 6.3, and while there is some scatter, seem to indicate a linear decrease in diameter along the length of the tube. This does provide some justification for the assumptions of a linear rate decrease along the tube length, but further, more controlled investigation of this effect should be considered.

Previous versions of the model have been applied and presented by Lister [25], Phromwong [27] and Kippers [26], which show excellent predictive capabilities over a wide range of system conditions. The model is built within a computer code and solved iteratively. Figure 6.4 and Figure 6.5 show an example output of a model run under neutral conditions with a flow rate of 0.5 L/min and a temperature of 140°C to compare directly with experimental data from the CNER Loop 1 facility, using a 1.6 mm ID FAC measurement

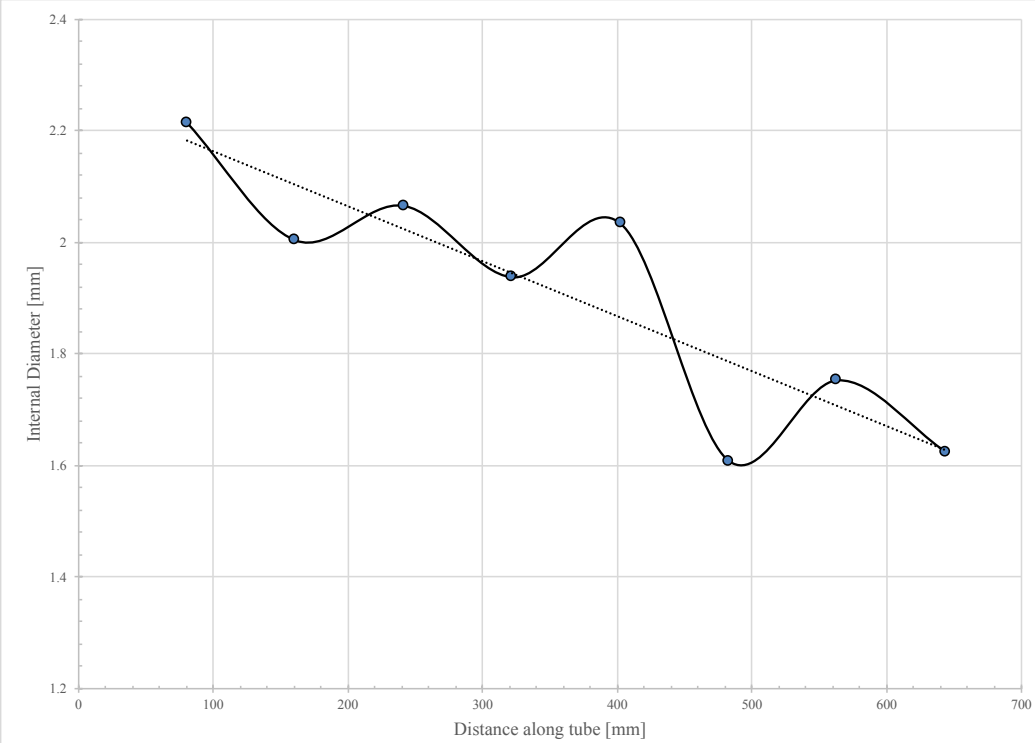

Figure 6.3: Sacrificial Iron Loop Section Outlet Diameters

probe. Additional model output with the associated variable inputs are provided in Appendix B. While oxide thickness was not measured, the predicted value is within the range of thicknesses measured in other UNB experiments [6]. The model prediction of 0.847 mm/yr average FAC rate at steady state corresponds well with the 0.85 mm/yr measured FAC rate in the loop. Keep in mind that this experimental value was used to benchmark and validate the model, so the k_{sp} term was optimized for this point to support later calculations.

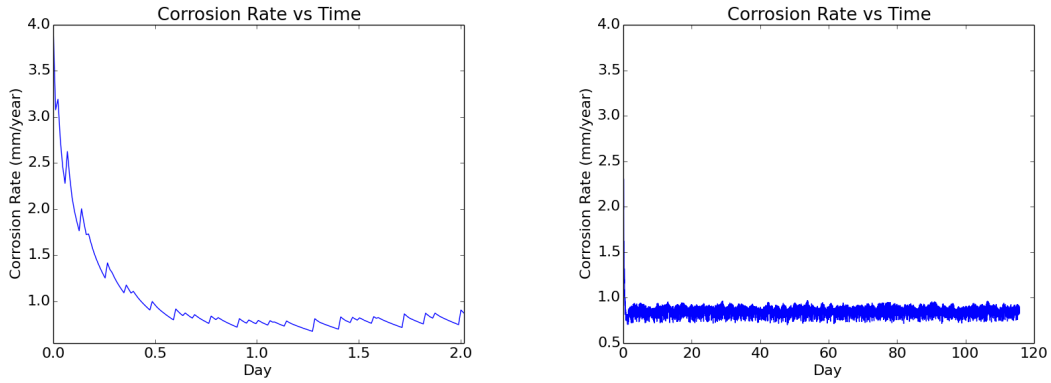

Figure 6.4: Model output, predicted FAC rate for neutral conditions, 0.5L/min, at 140°C

The scatter seen in Figure 6.4 is a consequence of variations inherent in the iterative nature of solving the functions, but primarily of the effects of oxide removal by flow effects (the spalling term). The spalling constant, k_{sp}, enables the model to be tailored to a specific band of conditions, and is how the model accounts for variables that are highly problematic to obtain. In particular, information regarding the morphology and stability of the oxide

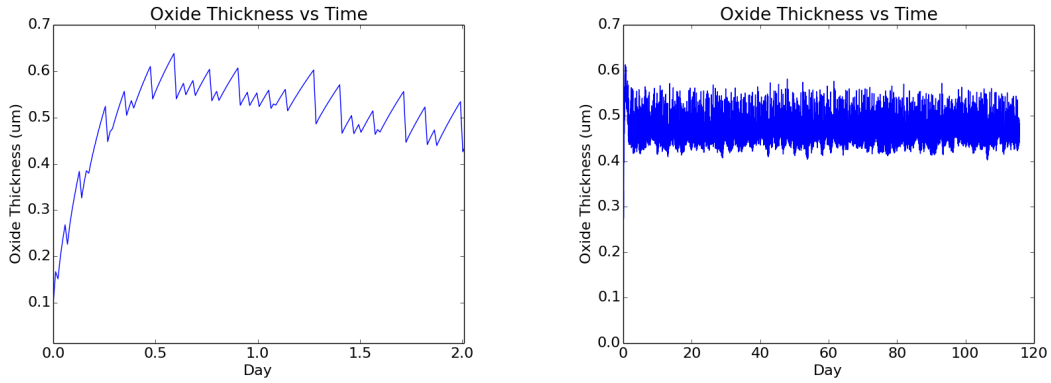

Figure 6.5: Model output, predicted oxide thickness for neutral conditions, 0.5L/min, at 140°C

formed under different conditions for example, while there is some indication that oxide porosity decreases with increasing temperature [22], measured values for oxide porosity variations with temperature are not available.

Figure 6.6 shows experimental FAC rates plotted against mass transfer coefficient [27], and subsequent k_{sp} values used in the current model to match the experimental rates obtained.

Applying this correlation to variations in mass transfer rate calculated using computational fluid dynamics (CFD) ([73],[26]) to simulate the effects of a nozzle exposed to FAC conditions, results from Kippers et al. [26] were updated with the current model in a two-dimensional simulation as presented in Figure 6.7, where $d^* = \delta/d$, d being the probe diameter and δ being the displacement from probe center line, and $x^* = x/d$, with x equal to the distance along the probe downstream of the nozzle.

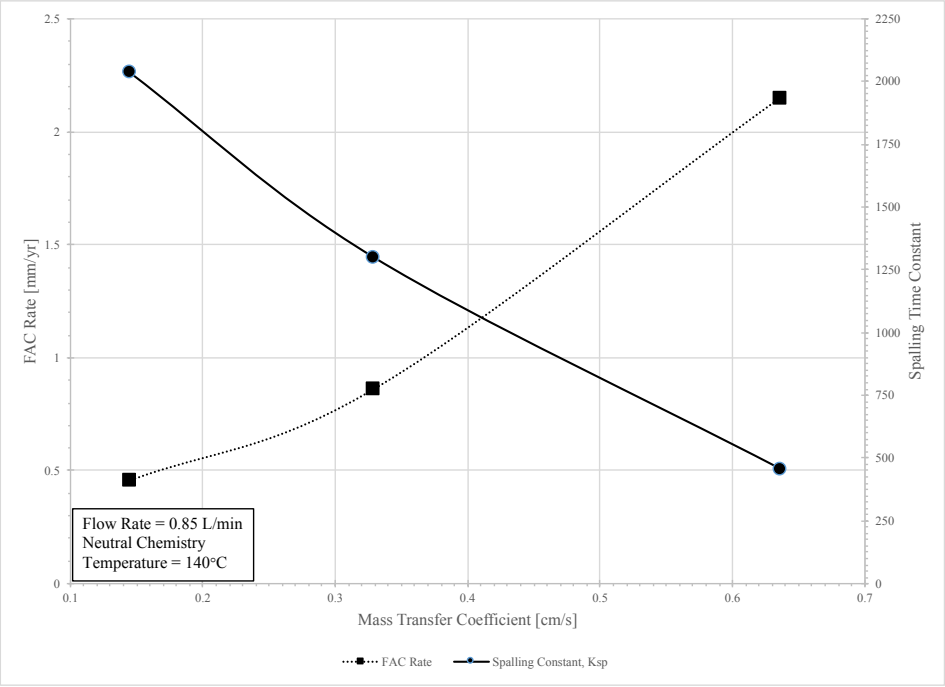

Figure 6.6: Variation of FAC rate and spalling time constant, k_{sp}, with change in mass transfer coefficient, k_m. Obtained by testing measurement probes of differing diameters (1.6 mm, 2.4 mm and 3.2 mm)

In addition to generating the mass transfer profiles with CFD, Kippers [73],[26] also carried out an experimental program to generate data to validate the CFD and modelling results. A measurement probe was fitted with a stainless steel insert that introduced a nozzle with a diameter of 0.8 mm just upstream of the measured section of the probe.

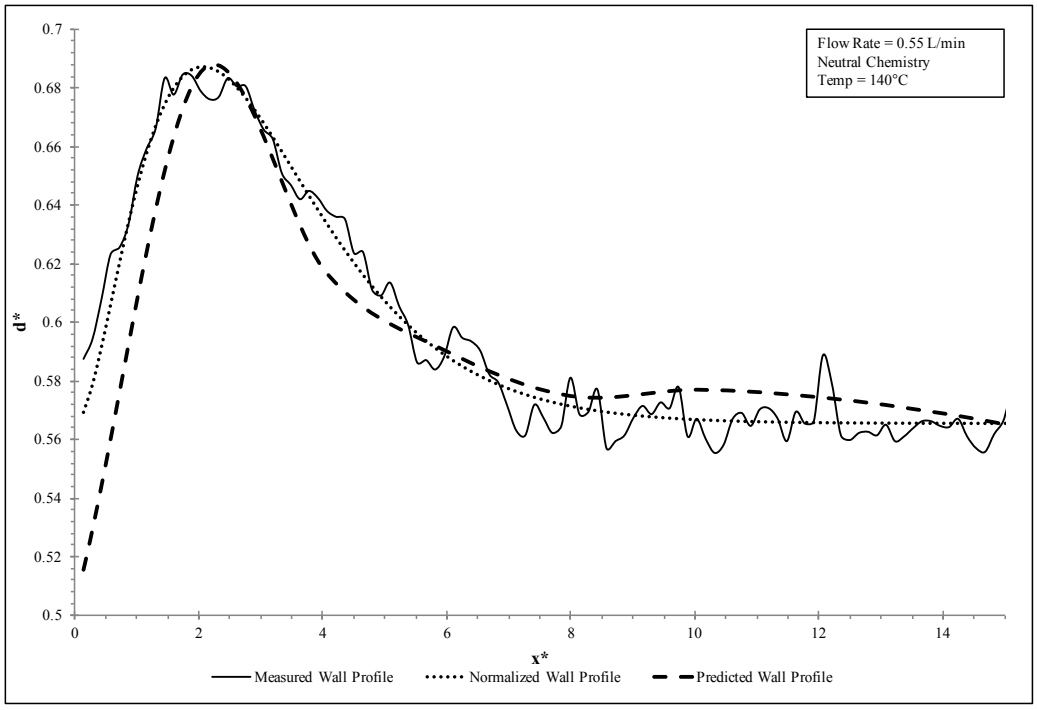

Figure 6.7: Measured and predicted wall profile due to FAC downstream of a nozzle

As can be seen from Figure 6.7, the current iteration of the UNB model prediction is a good fit to the actual measured profile downstream of the nozzle. It should be noted that this capability to accurately predict FAC under highly turbulent, geometrically challenging conditions is unique to the UNB mecha-

nistic model. Further exploration of this capability could greatly expand the application of FAC predictive modelling to the complex arrangements that currently rely solely on inspection for FAC detection. For example, welded connections that are not smooth on the inside diameter could be measured and modelled to determine not only the magnitude of wall thinning, but the locations downstream where maximum FAC will occur. By coupling computational fluid dynamics analysis with the UNB mechanistic model, virtually any geometry and flow condition should be within the capabilities of the model to accurately predict wall profiles due to FAC degradation. Figure 6.8 shows the predicted wall profile with time as corrosion proceeds in the highly turbulent flow, based on mass transfer rate values obtained from the CFD analysis by Kippers [73].

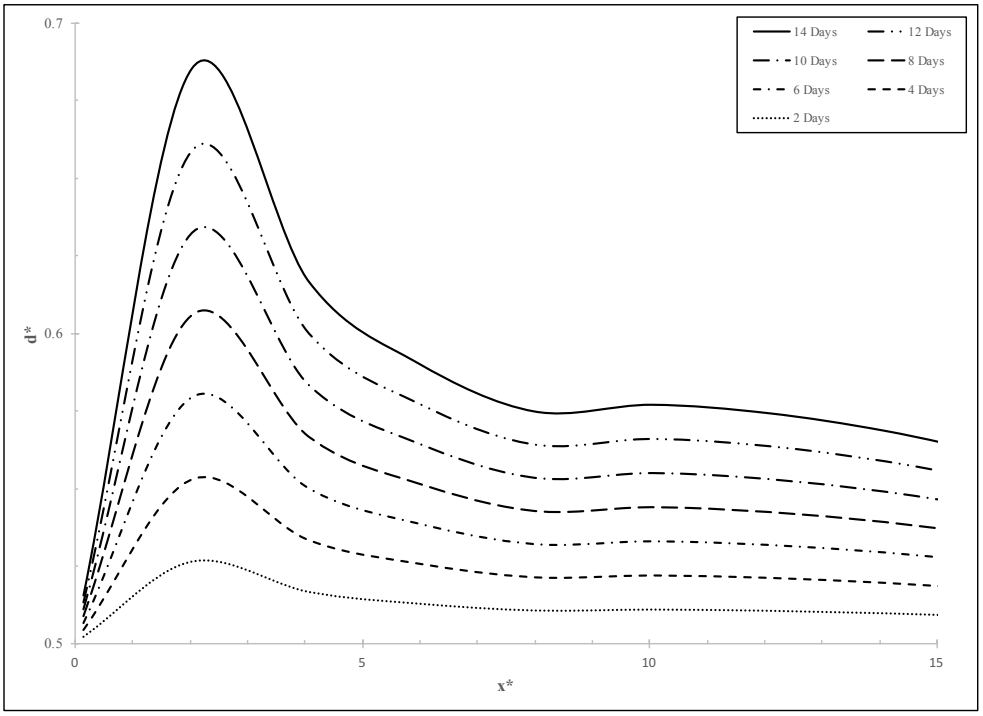

Figure 6.8: Predicted progression of wall thinning downstream of nozzle

Chapter 7

Conclusions

The UNB mechanistic model for predicting flow-accelerated corrosion has been enhanced to improve adaptability of the model to more complex conditions and geometries.

The temperature correlation presented by Lertsurasakda [59] has been experimentally validated and a process for calibrating resistance probes for online FAC measurement has been presented. This will enable researchers to gather more consistent and more precise FAC measurements for future FAC model development.

The effects of iron concentration in the bulk coolant on FAC have been investigated experimentally. A distinct effect has been observed when the concentration of iron in the bulk coolant is manipulated, and applying a

simple concentration difference effect on the driving force of the FAC mechanism has been shown to be inadequate to account for the effect. Coupling the calculations of surface concentration with mechanical removal of oxide particles to account for variations in the surface concentration with time has produced modelling results that reasonably agree with observed data.

A sampling process to accurately determine iron concentrations in the bulk coolant has been developed. Grab sampling of the at-temperature coolant reduces sampling errors introduced by varying coolant temperature through a sampling line, thus obtaining a more representative sample from the operating system. Initial results showed excellent agreement with calculated values, yet challenges with the sample retrieval process and schedule constraints limited the investigation and further development of this system.

Since the spalling term used in the mechanistic model is a controlling aspect when considering magnitude of the metal loss rate, and mass transfer has an integral effect on the magnitude of FAC in operating plant systems, a means of accounting for mass transfer in the spalling term has been introduced. Previously, the effects of wall shear stress were included in the spalling calculation by fluid velocity in a straight pipe. The model presented in this work relates the time to a spalling even to the Sherwood number, increasing the model's sensitivity to mass transfer values. This has improved the ability of the model to predict FAC rates in highly turbulent flows, thus resolving the limitation of FAC models to use geometric factors to account for complex

geometry. By coupling the mechanistic model with computational fluid dynamics analysis and obtaining discrete fields of mass-transfer rates through a system, any geometry and flow condition can be assessed for FAC in 1, 2 or 3 dimensions.

Chapter 8

Future Work

Based on the outcomes of the current research program, the following are recommended for further development of this work.

8.1 Model Development

While the model in its current state can predict FAC rates well, further work will add increased capability and flexibility. The model could be further validated against more data, including measurements from power plants taken under controlled conditions. Currently the data set available to test the model against is limited. It is recommended not only to obtain any available plant data, whether from nuclear or fossil, but also to expand the

experimental program to encompass more parameters. Specifically:

- Additional ranges of pH, and with various amines (ammonia, lithium hydroxide, ethanolamine) to validate adjustment of solubilities as well as electrochemical calculations.

- Additional temperature ranges between 85°C to 320°C. Current model validation included 140°C, 200°C and 310°C.

- Additional material compositions (primarily chromium content). Existing correlations (Figures 5.3 and 5.4) focus mostly on Cr concentrations >0.04%, yet evidence from UNB testing shows marked effects well below 0.04%.

- Additional geometries for testing and subsequently modelling to couple the mechanistic chemical/spalling model to computational fluid dynamics.

- Experiments to relate the spalling constant, k_{sp}, to the details of oxide morphology obtained under various conditions.

- Additional research is required to refine the electrochemical calculations. The chemical equations at the interfaces, and the interface structure itself, needs to be investigated further. Analysis of the computer code needs to be carried out to overcome the challenges with calculated electrochemical input parameters (Activation Energies in particular).

- The concept of variable mechanisms depending on conditions should be investigated. Pores-solutions vs. solid state diffusion, different interface structures, different response to material composition etc., all dependent on the conditions of interest.

The inclusion of oxygen effects will be important as the industry shifts from reducing treatments to oxygenated treatments to combat FAC. While oxygen generally stifles FAC, the reactions responsible also consume dissolved oxygen in the coolant. Thus, modelling can help to determine optimal placement of injection and sampling points, as well as to ensure that areas of FAC do not exist around the circuit where oxygen levels may dip below the threshold values for the given conditions.

The UNB model currently relies on user knowledge to select input variables beyond the simple chemistry and flow conditions of the system. Many of these values could be programmed into algorithms to be calculated automatically from verified relations or selected from existing data sets. For example, oxide dissolution rate constants, mass transfer coefficients, oxide porosity and tortuosity, could all be determined based on a simple set of input variables.

8.2 Sampling

The sampling system as described in the experimental section of this report is a good basis for further work on obtaining high-temperature grab samples for corrosion-product measurement in a development program. Development could include:

- Revised layout of the sampling system to minimize tubing runs and optimize system temperature control.
- Ensuring the glove-box is adequate for all the handling of the autoclaves and withdrawn samples.
- Further investigation into the use of acid mixtures (particularly nitric acid and thyoglycolic acid) to dissolve deposited iron species more effectively from the zirconium autoclaves.

8.3 Commercialization

In its current state, the UNB mechanistic model requires extensive experience and knowledge to operate, and even minor changes to the operating parameters can necessitate manipulation of the underlying computer code. With a step-wise approach, a more user friendly package could be developed to expand the capabilities of the model as well as make it more user friendly.

- Simplify variable input.
- Include integrated calculation of complex variables based on input variables, as well as including tabulated variables (for example, a number of variables are determined from tabulated values based on water temperature).
- Simplify time interval calculations to permit a basic model cycle duration input, effectively allowing for a specified number of days to model to be input as a parameter.
- Include a comprehensive user interface.

Bibliography

[1] G. Koch, M. Brongers, N. Thompson, Y. Virmani, J. Payer, "*Corrosion Costs and Preventative Strategies in the United States*," tech. rep., NACE FHWA-RD-01-156, Houston, TX, 2002.

[2] J. Gorman, M. Arey, G. Koch, "*Cost of Corrosion in the Electric Power Industry*," tech. rep., EPRI Report 1004662, Palo Alto, CA, 2001.

[3] "*Cost of Corrosion Annually in the US*." http://www.g2mtlabs.com/corrosion/cost-of-corrosion/. Accessed: 2016-04-23.

[4] J. Pietralik, "*The Role of Flow Accelerated Corrosion under Nuclear Power Plant Conditions*," E-Journal of Advanced Maintenance, vol. v. 4, pp. 63–78, 2012.

[5] D.H. Lister and S. Uchida, "*Reflections on FAC Mechanisms*," in Flow-Accelerated Corrosion (FAC) in Fossil and Combined

Cycle/HRSG Plants International Conference, (Arlington, VA, USA), July 2010.

[6] D.H. Lister et al, "*A Fundamental Study of Flow-Accelerated Corrosion in Feedwater System*," Power Plant Chemistry, vol. v. 10, no. n. 11, pp. 659–667, 2008.

[7] D.H. Lister et al, "*Effects of Dissolved Oxygen on Flow-Accelerated Corrosion in Feedwater Systems*," in 13th Int. Conf. on Envir. Deg. of Matls. in Nucl. Power Systems, (Whistler, BC), August 2007.

[8] EPRI, "*Flow Accelerated Corrosion in Power Plants*," tech. rep., EPRI Product TR1066110R1, Palo Alto, CA, 1998.

[9] G.J. Bignold et al, "*Mechanistic Aspects of Erosion-Corrosion Under Boiler Feedwater Conditions*," in Water Chemistry of Nuclear Reactor Systems 3, (London), pp. 219–226, BNES, 1983.

[10] Z. Walker, "*Managing Flow Accelerated Corrosion in Carbon Steel Piping in Nuclear Plants*," in Fitness for Service, Life Extension, Remediation, Repair and Erosion/Corrosion Issues for Pressure Vessel Components, (San Diego, CA), ASME, July 2004.

[11] M. Khatibi et al, "*Parameters Influencing Flow-Accelerated Corrosion (FAC) in the Secondary Side of Nuclear Power Plants*," in 30th Annual Conference of the Canadian Nuclear Society, (Calgary, Alberta), CNS, May 2009.

[12] R.B. Dooley and V.K. Chexal, "*Flow-Accelerated Corrosion of Pressure Vessels in Fossil Plants*," International Journal of Pressure Vessels and Piping, vol. v. 77, pp. 85–90, 2000.

[13] EPRI, "*Guidelines for Controlling Flow-Accelerated Corrosion in Fossil and Combined Cycle Plants*," tech. rep., EPRI Product 1008082, Palo Alto, CA, 2005.

[14] W. Cook, *Experiments and Models of General Corrosion and Flow-Assisted Corrosion of Materials in Nuclear Reactor Environments*. PhD thesis, University of New Brunswick, Fredericton, New Brunswick, Canada, February 2005.

[15] L. Tomlinson, "*Mechanism of Corrosion of Carbon and Low Alloy Ferritic Steels by High Temperature Water*," Corrosion, vol. v. 37, no. n. 10, pp. 591–596, 1981.

[16] P.R. Tremaine and J.C. LeBlanc, "*The Solubility of Magnetite and the Hydrolysis and Oxidation of* Fe^{2+} *in Water at 300°C*," Journal of Solution Chemistry, vol. v. 9, no. n. 6, pp. 415–442, 1980.

[17] F.H. Sweeton and C.F. Baes, "*The Solubility of Magnetite and Hydrolysis of Ferrous Irons in Aqueous Solutions at Elevated Temperatures*," Journal of Chemical Thermodynamics, vol. v. 2, pp. 479–500, 1970.

[18] K. Mohajery, L. Deydier de Pierrefeu and D.H. Lister, "*The Dissolution Rate Constant of Magnetite in Water at Different Temperatures and pH Conditions*," in Nuclear Plant Chemistry Conference, International Conference on Water Chemistry of Nuclear Reactor Systems, (Paris, France), 2012.

[19] G. Bohnsack, *The Solubility of Magnetite in Water and in Aqueous Solutions of Acid and Alkali*. Germany: Hemisphere Publishing Corporation, 1987.

[20] P. Berge, J. Decreux and P. Saint Paul, "*Effects of Chemistry on Corrosion-Erosion of Steels in Water and Wet Steam*," in Water Chemistry of Nuclear Reactor Systems 2, (London), pp. 19–23, BNES, 1980.

[21] G.J. Bignold et al, "*Erosion-Corrosion in Nuclear Steam Generators*," in Water Chemistry of Nuclear Reactor Systems 2, (London), pp. 5–18, BNES, 1980.

[22] L.E. Sanchez-Caldera, P. Griffith and E. Rabinowicz, "*The Mechanism of Corrosion-Erosion in Steam Extraction Lines of Power Stations*," Transactions of the ASME: J. Engineering for Gas Turbines and Power, vol. v. 110, pp. 180–184, 1988.

[23] M. Bouchacourt, "*Improvement of the Erosion-Corrosion Mechanistic Model: Role of Surface Oxide Film*," in Water Chemistry of Nuclear Reactor Systems 6, vol. v. 2, (London), pp. 338–339, BNES, 1992.

[24] S. Trevin and M. Moutrille, "*Optimization of EDF's NPPs Maintenance Due to Flow Accelerated Corrosion and BRT-CiceroTM Improvement by NDT Results Analysis*," in 18th World Conference on Nondestructive Testing 6, (Durban, South Africa), pp. 16–20, 2012.

[25] D.H. Lister and L. Lang, "*A Mechanistic Model for Predicting Flow-Assisted and General Corrosion of Carbon Steel in Reactor Primary Coolants*," in Int. Conf. Water Chem. Nucl. Reactor Systems, (Avignon, France), April 2002.

[26] N. Kippers et al, "*Modelling FAC Under Conditions of Accentuated Turbulence in Feedwater*," in Int. Conf. Flow Accelerated Corrosion, (Avignon, France), 2013.

[27] P. Phromwong, *Experimental and Modelling Study of Flow And Material Effects on Steel Corrosion Under Typical Power Plant Coolant Conditions*. PhD thesis, University of New Brunswick, Fredericton, New Brunswick, Canada, February 2013.

[28] EPRI, "*Fossil FAC Advisor Version 1.0 Beta User Guide*," tech. rep., EPRI Product TR1020900, Palo Alto, CA, 2010.

[29] M.D. Pandey, D.Lu, J. Riznic, "*A Probabalistic Assessment of Flow-Accelerated Corrosion Rate in Pipe Bends with Unknown Initial Thickness*," in Proceedings of the 2012 20th International Conference on Nuclear Engineering, (Anaheim, California), ASME, July 2012.

[30] M. I. Jyrkama and M. D. Pandey, "*Methodology for Predicting Flow-Accelerated Corrosion Wear Using Unreferenced Multiple Inspection Data*," Nuclear Engineering and Design, vol. v. 250, pp. 317–325, 2012.

[31] M. Jyrkama, M.D. Pandey, "*Risk-Informed Predictions of Feeder End of Life*," in 32nd Annual Conference of the Canadian Nuclear Society, (Niagara Falls, Ontario), CNS, June 2011.

[32] X.X. Yuan, M.D. Pandey, G.A. Bickel, "*A Probabalistic Model of Wall Thinning in CANDU Feeders Due to Flow-Accelerated Corrosion*," Nuclear Engineering and Design, vol. v.238, pp. 16–24, 2008.

[33] E.C. Potter and G.W.M. Mann, "*Oxidation of Mild Steel in High Temperature Aqueous Systems*," in 1st Int. Congress on Metallic Corrosion, (Butterworth, London), pp. 417–426, 1962.

[34] E.M. Field, R.C. Stanley, A.M. Adams and D.R. Holmes, "*The Growth, Structure and Breakdown of Magnentite Films on Mild Steel*," in Second International Congress on Metallic Corrosion, (New York), pp. 829–841, 1963.

[35] J. Johari, "*Modelling Corrosion for Corrosion-Product Transport in CANDU Reactors and PWRs*," Master's thesis, University of New Brunswick, Fredericton, New Brunswick, Canada, 1996.

[36] J.E. Castle, G.H. Masterson, "*The Role of Diffusion in the Oxidation of Mild Steel in High Temperature Aqueous Solutions*," Corrosion Science, vol. v. 6, pp. 93–104, 1966.

[37] L. Lang, "*Modelling the Corrosion of Carbon Steel Feeder Pipes in CANDU Reactors*," Master's thesis, University of New Brunswick, Fredericton, New Brunswick, Canada, 2000.

[38] G.J. Bignold, R.Garnsey, G.M.W. Mann, "*High Temp. Aqueous Corrosion of Iron Development of Theories of Equilibrium Solution Phase Transport Through a Porous Oxide*," Corrosion Science, vol. v. 12, pp. 325–332, 1972.

[39] J. Robertson, "*The Mechanism of High Temperature Aqueous Corrosion of Steel*," Corrosion Science, vol. v. 29, pp. 1275–1291, 1989.

[40] K. Garbett G. J. Bignold and I. S. Woolsey, "*Mechanistic Aspects of the Temperature Dependence of Erosion-Corrosion*," in Meeting on Erosion-Corrosion of Steels in High-Temperature Water and Wet Steam, (Les Renardieres, France), 1982.

[41] L. Tomlinson, M.H. Hurdus, P.J.B. Silver, "*The Effect of Hydrogen on the Corosion of a 2.25% Cr Ferritic Steel by High Temperature Water*," Corrosion Science, vol. v. 21, pp. 369–380, 1981.

[42] P. Berge, C. Ribon., P. Saint Paul, "*Effects of Hydrogen on the Corrosion of Steels in High Temperature Water*," Corrosion, vol. v. 32, pp. 223–228, 1976.

[43] D.H. Lister, "*Mass Transfer in the Contamination of Isothermal Steel Surfaces*," Nuclear Science and Engineering, vol. v. 61, pp. 107–118, 1976.

[44] C. Schreiner, S. Zugmann, R. Hartl, H. Gores, "*Fractional Walden Rule for Ionic Liquids: Examples from Recent Measurements and Critique of the So-Called Ideal KCl Line for the Walden Plot*," J. Chemical Engineering Data, vol. v. 55, pp. 1784–1788, 2010.

[45] K.D. Efird, "*Effect of Fluid Dynamics on the Corrosion of Copper-Base Alloys in Sea Water*," Corrosion, vol. v. 33, pp. 3–8, 1977.

[46] B.C. Syrett, "*Erosion-Corrosion of Copper-Nickel Alloys in Sea Water and Other Aqueous Environments - A Literature Review*," Corrosion, vol. v.32, pp. 242–252, 1976.

[47] E. Heitz, "*Chemo-Mechanical Effects of Flow on Corrosion*," Corrosion, vol. v.47, pp. 135–145, 1991.

[48] S. Nesic, J. Postlethwaite, "*Relationship Between the Structure of Disturbed Flow and Erosion-Corrosion*," Corrosion, vol. v.46, pp. 874–880, 1990.

[49] T. Sydberger, U. Lotz, "*Relation Between Mass Transfer and Corrosion in a Turbulent Pipe Flow*," J. Electrochemical Society: Electrochemical Science and Technology, vol. v.129, pp. 276–283, 1982.

[50] G. Schmitt, M. Bakalli, "*Advanced Models for Erosion Corrosion and Its Mitigation*," Materials and Corrosion, vol. v.59, pp. 181–192, 2008.

[51] J.W. Cleaver and B. Yates, "*Mechanism of Detachment of Colloidal Particles from a Flat Substrate in a Turbulent Flow*," Journal of Colloid and Interface Science, vol. v. 44, pp. 464–474, 1973.

[52] W.H. Ahmed, "*Evaluation of the proximity effect on flow-accelerated corrosion*," Annals of Nuclear Energy, vol. v.37, pp. 598–605, 2008.

[53] M.Coney, S. Wilkin, H.Oates, "*Thermal-Hydraulic Effects on Mass Transfer Behaviour and on Erosion-Corrosion Metal Loss Rates*," tech. rep., Central Electricity Generating Board, Leatherhead, England, 1980.

[54] D.J. Tagg, M.A. Patrick, A.A. Wragg, "*Heat and Mass Transfer Downstream of Abrupt Nozzle Expansions in Turbulent Flow*," Chemical Engineering Research and Design, vol. v.57, pp. 171–181, 1979.

[55] T.Y Rizk, G.E. Thompson, J.L. Dawson, "*Mass Transfer Enhancement Associated With Sudden Flow Expansion*," Corrosion Science, vol. v.38, pp. 1801–1814, 1996.

[56] M. El-Gammal, W.H. Ahmed, C.Y. Ching, "*Investigation of wall mass transfer characteristics downstream of an orifice*," Nuclear Engineering and Design, vol. v.242, pp. 353–360, 2011.

[57] F.P. Berger and K. Hau, "*Mass Transfer in Turbulent Pipe Flow Measured by the Electrochemical Method*," Int. J. Heat Transfer, vol. v. 20, pp. 1185–1194, 1977.

[58] "*ASTM G96-90(2001)e1 - Standard Guide for On-Line Monitoring of Corrosion in Plant Equipment (Electrical and Electrochemical Methods)*." ASTM International.

[59] C. Lertsurasakda, *Investigation of Flow-Accelerated Corrosion Under Two-Phase Flow Conditions*. PhD thesis, University of New Brunswick, Fredericton, New Brunswick, Canada, July 2013.

[60] T. Petrova, R.B. Dooley, "*Corrosion Product Sampling and Analysis for Fossil and Combined Cycle Plants*," tech. rep., International Association for the Properties of Water and Steam, London, UK, 2013.

[61] P. Sturla, "*Oxidation and Deposition Phenomena in Forced Circulating Boilers and Feedwater Treatment*," in Fifth National Feedwater Conf., (Prague), 1973.

[62] E.M. Pavageau, "*Effect of Hydrazine on Flow Accelerated Corrosion*," tech. rep., EPRI Report 1008208, Palo Alto, CA, 2005.

[63] EPRI, "*Results of an Experimental Program Conducted in Électricité de France's CIROCO Loop*," tech. rep., EPRI Product TR1011837, Palo Alto, CA, 2006.

[64] P. Phromwong et al, "*Modelling Material Effects in Flow-Accelerated Corrosion*," in 15th Int. Conf. on Envir. Deg. Of Matls. in Nucl. Power Plant Systems, (CO, US), BNES, August 2011.

[65] B. Poulson, "*Complexities in Predicting Erosion Corrosion*," Wear, vol. v. 233-235, pp. 497–504, 1999.

[66] J.M. Pietralik, C.S. Schefski, "*Flow and Mass Transfer in Bends Under Flow-Accelerated Corrosion Wall Thinning Conditions*," Journal of Engineering for Gas Turbines and Power, vol. v. 133, pp. 1–7, 2011.

[67] S.E. Ziemniak, M.E. Jones and K.E.S. Combs, "*Solubility and Phase Behavior of Cr(III) Oxides in Alkaline Media at Elevated Temperatures*," Journal of Solution Chemistry, vol. v. 278, pp. 33–66, 1998.

[68] B. Beverskog and I. Puigdomenech, "*Revised Pourbaix Diagrams for Iron at 25-300°C*," Corrosion Science, vol. v. 38, pp. 2121–2135, 1996.

[69] J. O'M. Bockris, A.K.N. Reddy, *Modern Electrochemistry - An Introduction to an Interdisciplinary Area, Volume 2*. New York: Plenum Press, 1970.

[70] R.T. Ferrell and D.M. Himmelblau, "*Diffusion Coefficients of Hydrogen and Helium in Water*," AIChE Journal, vol. v. 13, pp. 702–708, 1967.

[71] K. McKeen, M. Lalonde, A. Scott, J. Ross, "*Hydrogen Effusion Probe Development and Installation at the Point Lepreau Generating Station*," in 28th Annual conference of the Canadian Nuclear Society, (Saint John, New Brunswick, Canada), 2007.

[72] C.R. Stuart, W.G. Cook, E.C. Gardner, "*Primary Heat Transport System Return To Service Following The Refurbishment Outage At The Point Lepreau Generating Station*," in Nuclear Plant Chemistry Conference, (Sapporo, Japan), 2014.

[73] N. Kippers, "Private communication." 2014.

Appendix A

Appendix A Computational Code

```
'''
Created on Feb 19, 2017

@author: Michael A. Briggs
'''
import os
import csv
import random as rand
import matplotlib.pyplot as plt
import numpy as np
import math
```

```
############################
# This section imports model data from comma separated
   variable file [ .csv ]

import csv
reader = csv.reader(open("/Users/michaelbriggs/Documents
   /UNB/ModellingWorkingFolder/FAC_Main_Mk1_Inputs_4.csv
   "), delimiter=',')
data = []
for row in reader:
    data.append(row)

#now you can use indices to address a cell such as:
# to index, [row][column], note that column or row # 1
   is identified as 0.

#To select the instance of conditions to test from CSV,
   assign column # to the corresponding column in the
   csv minus 1 (so column D you would enter 3)
column =input ("What␣data␣column␣would␣you␣like␣to␣model
   ?␣Hint:␣Column␣number␣=␣letter␣number␣-1,␣so,␣column␣
   D␣would␣be␣3,␣column␣E␣would␣be␣4:")
CB = float(data[8][column])
```

```
CSat_OB = float(data[9][column])
Ce_OB = float(data[10][column])
CSat_PO = float(data[11][column])
Ce_OP = float(data[12][column])
CSat_MP = float(data[14][column])
Ce_MP = float(data[14][column])
Ce_MO = float(data[15][column])
Ce_OC = float(data[16][column])
CSat_Cr = float(data[17][column])
U = float(data[18][column])
kd = float(data[19][column])
km = float(data[20][column])
ksp = float(data[21][column])
kCR = float(data[22][column])
Temperature0 = float(data[23][column])
TKelvin = float(data[24][column])
DP0 = float(data[25][column])
DFe0 = float(data[26][column])
f0 = float(data[27][column])
S0 = float(data[28][column])
DeltaP0 = float(data[29][column])
ChiP0 = float(data[30][column])
PhiP0 = float(data[31][column])
RhoP0 = float(data[32][column])
```

```
MP0 = float(data[33][column])
RhoH2O = float(data[34][column])
MFe0 = float(data[35][column])
RhoFe0 = float(data[36][column])
RhoSteel0 = float(data[37][column])
PhiOX0 = float(data[38][column])
ChiOX0 = float(data[39][column])
RhoOX0 = float(data[40][column])
DCORs0 = float(data[41][column])
Delta = float(data[42][column])
t0 = float(data[43][column])
tstep0 = float(data[44][column])
Paverage0 = float(data[45][column])
SDP0 = float(data[46][column])
CrContent0 = float(data[47][column])
FF = float(data[48][column])
CH2coolant = float(data[49][column])
ConcC4H9ONTotal = float(data[50][column])
CorrosionRateExp0 = float(data[51][column])
iH2_Hp_OB0 = float(data[52][column])
EmixedInitial0 = float(data[53][column])
n = float(data[54][column])
F0 = float(data[55][column])
R = float(data[56][column])
```

```
h0 = float(data[57][column])
kboltzman = float(data[58][column])
Beta = float(data[59][column])
FeMolarMass = float(data[60][column])
H2MolarMass = float(data[61][column])
EcorrInitial0 = float(data[62][column])
FeCr2O4 = float(data[63][column])
ActivationEFe_Fe2_MP = float(data[64][column])
ActivationEH2_Hp_MP = float(data[65][column])
ActivationEH2_Hp_OB = float(data[66][column])
ActivationEFe2p_Fe3O4_OB = float(data[67][column])
ActivationEFe2p_Fe3O4_OP = float(data[68][column])
ActivationEH2_Hp_OP = float(data[69][column])
pH = float(data[70][column])
MU = float(data[71][column])
probediameter = float(data[72][column])
kd_OB = kd
kd_OP = kd
Time = list()
Thickness = list()
corrosionnrate = list()
kdiss = list()
OB_Con = list()
OP_Con = list()
```

```
MP_Con = list()
CSAT = list()
DummyTime = t0
j = 0
spall = list()
mu, sigma = 0.0, 100.0 # mean and standard deviation for
    spalling function
AverCorRate =0.0
AverThickness = 0.0
hH2 = km

####################################
#Gibbs Energy Calculations -- Criss and Cobble
   Correspondence Principle -- Adjusting to operating
   temperature

### Fe ###
# Using the CP value at 298 and assuming constant CP
   over the temperatures of 298-498 K
CP0Fe  = 24.98 #  from Beverskog
GF0Fe = 0.0 # G of formation at standard temperature and
    pressure at 298.15K
S0Fe = 27.28 # entropy at standard temperature and
   pressure from Beverskog
```

```
HF0Fe = 0.0
# Standard G formation of elements is  0 at any
   temperature by definition
DeltaGfFe = 0.0

### Fe3O4 ###
CP0Fe3O4 = 150.73  #From Ziemniak
GF0Fe3O4 = -1012.57# from Beverskog
S0Fe3O4 = 146.14 # from Beverskog
HF0Fe3O4 = -1118.38
#G formation at T = DeltaGf = G0 + (CP0 - S0)*(TKelvin -
    298.15) - T*CP0*Ln(T/298.15) assuming an average CP
DeltaGfFe3O4 = GF0Fe3O4 + ((CP0Fe3O4 - S0Fe3O4) * (
   TKelvin - 298.15) - TKelvin * CP0Fe3O4 * math.log(
   TKelvin / 298.15))/1000

### H2O ###
# J/mol.K; Used the value of Cp at 25 C, small change
   over the temperature of 25-300 C
# All values from Ziemniak
CP0H2O = 75.29
GF0H2O = -237.1
S0H2O = 69.95
HF0H2O = -285.85
```

```
DeltaGfH2O = GF0H2O + ((CP0H2O - S0H2O) * (TKelvin -
   298.15) - TKelvin * CP0H2O * math.log(TKelvin /
   298.15))/1000

### H2 (g) ###
# All values from Ziemniak
CP0H2 = 28.84
GF0H2 = 0
S0H2 = 130.68
HF0H2 = 0
DeltaGfH2 = 0

### H+###
# All values from Ziemniak
CP0Hp = -71.0
GF0Hp = 0
S0Hp = -22.20
HF0Hp = 0
DeltaGfHp = GF0Hp + ((CP0Hp - S0Hp) * (TKelvin - 298.15)
    - TKelvin * CP0Hp * math.log(TKelvin / 298.15))/1000

### Fe(OH)2 ###
CP0FeOH2 = 133.0 # From Tremaine
GF0FeOH2 = -447  # From Beverskog
```

```
S0FeOH2 = -29.20 # From Ziemniak
HF0FeOH2 = -563.08
DeltaGfFeOH2 = GF0FeOH2 + ((CP0FeOH2 - S0FeOH2) * (
   TKelvin - 298.15) - TKelvin * CP0FeOH2 * math.log(
   TKelvin / 298.15))/1000

## #Fe2+ ###
CP0Fe2p = 90.0  #83
GF0Fe2p = -88.92 #-91.88 # from Beverskog
S0Fe2p = -107.1 #-105.6
HF0Fe2p = -88.69
DeltaGfFe2p = GF0Fe2p + ((CP0Fe2p - S0Fe2p) * (TKelvin -
    298.15) - TKelvin * CP0Fe2p * math.log(TKelvin /
   298.15))/1000

#Corrosion reaction: Fe + 2H2O = 2H+ +2e- + Fe(OH)2 (
   equations should always be written as reduction)   Fe
   (OH)2 + 2H+ +2e- = Fe + 2H2O

DeltaGFe_Fe2 = DeltaGfFe + 2 * DeltaGfH2O - 2*DeltaGfHp
   - DeltaGfFeOH2 #-20
#Magnetite precipitation and dissolution   Fe3O4 + 2H2O
   + 2H+ + 2e- = 3 Fe(OH)2
```

```
DeltaGFe2p_Fe3O4 = 80#3*DeltaGfFeOH2 - DeltaGfFe3O4 - 2 *
    DeltaGfH2O - 2*DeltaGfHp #80
#Hydrogen Production or consumption:   2H+ + 2e = H2
DeltaGH2_Hp = DeltaGfH2 - 2 * DeltaGfHp

# Hydrogen Henry's constant at Temperature T
kHenry298 = 0.00078; # mol/L.atm
kHenry = kHenry298 * math.exp(-500*(1 / TKelvin - 1 /
   298.15)) # value of 500 taken From Aom's thesis

##############################
# Primary Functions for calculation of corrosion rate
   and oxide thickness change at each iteration

#Change in oxide thickness function
def DDeltaFunction(DeltaOX, Ce_MP, CSat_OB, CB, Ce_OB,
   kd):
    if DeltaOX <= 0:
        DeltaOX = 0.0
    A = 1* (Ce_MP)
    B = ((kd * f0 * S0 * CSat_OB) + km * CB) / ((kd * f0
       ) + km)
    D = kCR*(ChiP0 * DeltaP0) /(PhiP0 * DFe0 * RhoP0 *
       (1 - PhiP0))
```

```
    E = (0.476 * (1.101 + PhiOX0) * ChiOX0 * DeltaOX) /(
       PhiOX0 * DFe0 * RhoOX0 * (1 - PhiOX0))
    F = (0.476 * (1.101 + PhiOX0)) / ((kd * f0) + km)
    DMi = (A - B) / ( D + E + F)
    DDelta = (0.476 * DMi * (1.0 - PhiOX0) - (kd * f0 *
       (S0 * CSat_OB - Ce_OB))) / 0.723 # variation in
       oxide thickness

    if Delta == 0:
        DDelta = 0.476 * DMi * (1.0 - PhiOX0)
    if DDelta < 0:
        DDelta = 0.476 * DMi * (1.0 - PhiOX0)
    return  DDelta

# Corrosion Rate Function

####  CHANGED DELTA TO DELTAOX ######

def CorrosionRateFunction(DeltaOX, Ce_MP, CSat_OB, CB):
    if DeltaOX <= 0:
        DeltaOX = 0.0
    AA = 1 *(Ce_MP)
    BB = ((kd * f0 * S0 * CSat_OB) + km * CB) / ((kd *
       f0) + km)
```

```
    DD = kCR*(ChiP0 * DeltaP0) /(PhiP0 * DFe0 * RhoP0 *
       (1 - PhiP0))
    EE = (0.476 * (1.101 + PhiOX0) * ChiOX0 * DeltaOX)
       /(PhiOX0 * DFe0 * RhoOX0 * (1 - PhiOX0))
    FF = (0.476 * (1.101 + PhiOX0)) / ((kd * f0) + km)
    DM = (AA - BB) / ( DD + EE + FF)
    return  DM

def FACECPCal(kd, CH2coolant,DeltaGFe_Fe2,
   DeltaGFe2p_Fe3O4,DeltaGH2_Hp ,kHenry , CSat_OB, Ce_MP
   , Ce_OP, Ce_OB,  DeltaOX, DMOX,  TKelvin,
   ConcC4H9ONTotal, ActivationEFe_Fe2_MP,
   ActivationEH2_Hp_MP, ActivationEH2_Hp_OB,
   ActivationEFe2p_Fe3O4_OB,ActivationEH2_Hp_OP,
   ActivationEFe2p_Fe3O4_OP, pH):

## Electrochemical Calculations for each iteration,
   changing based on Corrosion Rate and Oxide thickness
   values.

    kd_OB = kd_OP = kd

    # Calculate Concentration of Hydrogen in bulk
    CeHp = math.pow(10, -pH)
```

```
    #Diffusivity of H2
    DH2 = 0.0000222 * TKelvin * math.exp(-12400 / (R *
       TKelvin))

    hH2 = km * DH2/ DFe0

    AP = (RhoP0 * (1 - PhiP0) * DH2 * PhiP0)/(DeltaP0 *
       ChiP0)  # diffusion calculation from base
       equation for passivating layer
    AOX= (RhoOX0 * (1 - PhiOX0) * DH2 * PhiOX0)/(DeltaOX
        * ChiOX0) # diffusion calculation for oxide
       layer

# H2 concentration at M_P interface assuming high mass
   transfer to the bulk

    CH2coolant = CH2coolant * 1e-6 * H2MolarMass *
       101325 * RhoH2O / (8.314 * 298.15 * 1000)  # cm
       ^3/kg water *1e-6 * H2MolarMass *P/(RT) * rowater
       /1000 = g H2/cm^3 H2O
    CeH2_MP = (CH2coolant + 0.1*(0.005659 * DMOX * (1.63
        - PhiOX0) *(1 / AOX + 1 / hH2)) + 3.58e-3 *DMOX
       / AP) # assume 90% of H2 at this interface
```

```
        actually moves through metal
    CeH2_OP = (CH2coolant + (0.005659 * DMOX * (1.63 -
        PhiOX0) *(1 / AOX + 1 / hH2)))

# H2 concentration at O_B interface
    CeH2_OB = CH2coolant + (0.005659 * DMOX * (1.63 -
        PhiOX0) / hH2)

#Dissolution of magnetite at O_B interface Fe3O4 + 2H2O
   + 2H+ + 2e- = 3 Fe(OH)2
    nFe2p_Fe3O4_OB = 2.0

    EeFe2p_Fe3O4_OB = -1 *  DeltaGFe2p_Fe3O4 * 1000/ (
        nFe2p_Fe3O4_OB * F0) - math.log(10) * 2 * R *
        TKelvin / (nFe2p_Fe3O4_OB * F0) * pH - 3 * R *
        TKelvin / (nFe2p_Fe3O4_OB * F0) * math.log(Ce_OB
        * 1000 / 90.0) # Equilibrium potential for
        dissolution reaction at O_B interface

    i0Fe2p_Fe3O4_OB = F0 * kboltzman * TKelvin / h0 * (
        math.exp(-1 * ActivationEFe2p_Fe3O4_OB  / (R *
        TKelvin )) * math.pow(Ce_OB * 1000 / 90.0, 1.0)*
         math.exp(-1 * Beta * nFe2p_Fe3O4_OB * F0 *
        EeFe2p_Fe3O4_OB / (R * TKelvin)));
```

```
#Hydrogen consumption at O_B interface 2H+ + 2e- =  H2

    nH2_Hp_OB = 2.0

    EeH2_Hp_OB = -1 * DeltaGH2_Hp * 1000 / (nH2_Hp_OB *
       F0 ) - math.log(10) * 2 * R * TKelvin * pH / (
       nH2_Hp_OB * F0) - R * TKelvin / (nH2_Hp_OB * F0)
       * math.log((CeH2_OB * 1000 / 2.0 )) # At O_B
       interface

    i0H2_Hp_OB = F0 * kboltzman * TKelvin / h0 * math.
       exp(-1 * ActivationEH2_Hp_OB / (R * TKelvin)) *
       math.pow(CeH2_OB * 1000 / H2MolarMass, 1.0) *
       math.exp(-1 * Beta * nH2_Hp_OB * F0 * EeH2_Hp_OB
       /(R * TKelvin));

# Mixed Potential at the O_B interface
    i0_H1= i0H2_Hp_OB * math.exp(Beta * nH2_Hp_OB * F0 *
        EeH2_Hp_OB / (R * TKelvin))

    i0_H2 = i0H2_Hp_OB * math.exp(-1 * (1 - Beta) *
       nH2_Hp_OB * F0 * EeH2_Hp_OB / (R * TKelvin))
```

```
    i0_Fe1 = i0Fe2p_Fe3O4_OB * math.exp(Beta *
       nFe2p_Fe3O4_OB * F0 * EeFe2p_Fe3O4_OB / (R *
       TKelvin))

    i0_Fe2 = i0Fe2p_Fe3O4_OB * math.exp(-1 * (1 - Beta)
       * nFe2p_Fe3O4_OB * F0 * EeFe2p_Fe3O4_OB / (R *
       TKelvin))

    Emixed = R * TKelvin  / (nFe2p_Fe3O4_OB * F0 * Beta
       * 2) * math.log((i0_H1 + i0_Fe1) / (i0_H2 +
       i0_Fe2))

#Adjusting the concentration of iron species at O_B
   interface (in mol/l should be calculated back to g/cm
   ^3)
    CSat_OBNew = (math.exp((Emixed + DeltaGFe2p_Fe3O4 *
       1000/ (nFe2p_Fe3O4_OB * F0) + 2 * R * TKelvin *
       math.log(10) * pH / (nFe2p_Fe3O4_OB * F0)) * (-1)
        * nFe2p_Fe3O4_OB * F0 / (3 * R * TKelvin)))* 90
       / 1000

#Adjusting the dissolution rate constant of magnetite

    ked_OB = kd_OB * math.exp(-1 * (1 - Beta) *
```

```
        nFe2p_Fe3O4_OB * F0 * (Emixed - EeFe2p_Fe3O4_OB)
        / (R * TKelvin))

# At O_P interface
#Precipitation of magnetite at O_P interface   Fe3O4 + 2
   H2O + 2H+ + 2e- = 3Fe(OH)2
# R * 6 is due to the fact that the n=1/3 in these
   equation instead of 2
    nFe2p_Fe3O4_OP =.33

    EeFe2p_Fe3O4_OP = -1 *  DeltaGFe2p_Fe3O4 * 1000 / (2
        * F0) - math.log(10) * R * TKelvin /(F0) * pH -
       3 * R * TKelvin / (2 * F0) * math.log(Ce_OP *
       1000 / FeMolarMass)

    i0Fe2p_Fe3O4_OP = F0 * kboltzman * TKelvin / h0 * (
       math.exp(-1 * ActivationEFe2p_Fe3O4_OP  / (R *
       TKelvin )) * math.pow(Ce_OP * 1000 / 90.0, 1.0)*
        math.exp(-1 * Beta * nFe2p_Fe3O4_OP * F0 *
       EeFe2p_Fe3O4_OP / ( R * TKelvin)));


#Hydrogen production 2H+ + 2e- = H2 at O_P;
    nH2_Hp_OP = 0.33
```

```
    EeH2_Hp_OP = -1 * DeltaGH2_Hp * 1000 / (2 * F0 ) -
       math.log(10) *  R * TKelvin * pH / (F0)  - R *
       TKelvin / (2 * F0) * math.log((CeH2_OP* 1000 /
       2.0 ))

    i0H2_Hp_OP = F0 * kboltzman * TKelvin / h0 * (math.
       exp(-1 * ActivationEH2_Hp_OP / (R * TKelvin)) *
       math.pow(CeH2_OP * 1000  / H2MolarMass , 1.0) *
       math.exp(-1 * Beta * nH2_Hp_OP * F0 * EeH2_Hp_OP
       / (R * TKelvin)))

# Mixed Potential at the O_P interface
    i0_H1OP= i0H2_Hp_OP * math.exp(Beta * nH2_Hp_OP * F0
        * EeH2_Hp_OP / ( R * TKelvin))

    i0_H2OP = i0H2_Hp_OP * math.exp(-1 * (1 - Beta) *
       nH2_Hp_OP * F0 * EeH2_Hp_OP / ( R * TKelvin))

    i0_Fe1OP = i0Fe2p_Fe3O4_OP * math.exp(Beta *
       nFe2p_Fe3O4_OP * F0 * EeFe2p_Fe3O4_OP / ( R *
       TKelvin))

    i0_Fe2OP = i0Fe2p_Fe3O4_OP * math.exp(-1 * (1 - Beta
```

```
        ) * nFe2p_Fe3O4_OP * F0 * EeFe2p_Fe3O4_OP / ( R *
         TKelvin))

#just for Beta = 0.5
    EmixedOP =  R * TKelvin  / ( nFe2p_Fe3O4_OP * F0 *
       Beta * 2) * math.log((i0_H1OP + i0_Fe1OP) / (
       i0_H2OP + i0_Fe2OP))

#Adjusting the dissolution rate constant of magnetite
    ked_OP = kd_OP * math.exp(-1 * (1 - Beta) *
       nFe2p_Fe3O4_OP * F0 * (EmixedOP - EeFe2p_Fe3O4_OP
       ) / ( R * TKelvin))

#Adjusting the concentration of iron species at O_P
   interface (in mol/l should be calculated back to g/cm
   ^3)
    CSat_OPNew = (math.exp((EmixedOP + DeltaGFe2p_Fe3O4
       * 1000/ (2 * F0) +  R * TKelvin * math.log(10) *
       pH / (F0)) * (-1) * 2 * F0 / (3 * R * TKelvin)))*
        90 / 1000

    Ce_OPNew = CSat_OPNew + (0.476* (1-PhiOX0)*DMOX /
       ked_OP) * 90 / 1000
```

```
    Ce_MPNew = (DMOX * ChiP0 * DeltaP0 /(PhiP0 * DP0 *
       RhoP0 * (1 - PhiP0)) + Ce_OPNew*1000/90)*56/1000


# At M-P interface

#Oxidation of Fe at M_P interface   Fe^2+ + 2e- = Fe

    nFe_Fe2p_MP = 2
    EeFe_Fe2p_MP = -1 * DeltaGFe_Fe2* 1000 / (
       nFe_Fe2p_MP * F0) - math.log(10) * 2 * R *
       TKelvin / (nFe_Fe2p_MP * F0) * pH + R * TKelvin /
        (nFe_Fe2p_MP * F0) * math.log(Ce_MPNew * 1000 /
       FeMolarMass)
    i0Fe_Fe2p_MP = F0 * kboltzman * TKelvin / h0 * (math
       .exp(-1 * ActivationEFe_Fe2_MP  / (R * TKelvin))
       * math.pow(Ce_MPNew * 1000 / FeMolarMass,1.0) *
       math.exp(-1 * Beta * nFe_Fe2p_MP * F0 *
       EeFe_Fe2p_MP / (R * TKelvin)));

#Hydrogen production 2H+ + 2e- = H2 at M_P;
    nH2_Hp_MP = 2
    EeH2_Hp_MP = -1 * DeltaGH2_Hp * 1000 / (nH2_Hp_MP *
       F0 ) - math.log(10) * 2 * R * TKelvin * pH / (
```

```
   nH2_Hp_MP * F0)  - R * TKelvin / (nH2_Hp_MP * F0)
    * math.log((CeH2_MP* 1000 / 2.0 ))
# At M_P interface, CH2_MP converted to mol/l, g/cm
   ^3 * 1000/Molar mass H2 and then to atm: mol/l/
   KHenry(mol/l.atm) => atm
i0H2_Hp_MP = F0 * kboltzman * TKelvin / h0 * (math.
   exp(-1 * ActivationEH2_Hp_MP / (R * TKelvin)) *
   math.pow(CeH2_MP * 1000  / H2MolarMass , 1.0) *
   math.exp(-1 * Beta * nH2_Hp_MP * F0 * EeH2_Hp_MP
   / (R * TKelvin)))


A1 = DMOX * (n * F0) / (FeMolarMass * i0Fe_Fe2p_MP)
C1 = Beta * n * F0 / (R * TKelvin)
C2 = math.exp(C1 * (EeFe_Fe2p_MP))
X1 = (A1 + math.pow(math.pow(A1,2) + 4, 0.5)) / 2
X2 = (A1 - math.pow(math.pow(A1,2) + 4, 0.5)) / 2


if (X1 <=0 and X2 > 0):
    Ecorr = math.log(X2) / C1 + EeFe_Fe2p_MP
elif X1 > 0:
    Ecorr = math.log(X1) / C1 + EeFe_Fe2p_MP
else:
```

```
        print ('error')


    CSat_MPNew = (math.exp((Ecorr + DeltaGFe_Fe2 * 1000
       / (n * F0 ) + math.log(10) * 2 * R * TKelvin * pH
        / (n * F0)) * (1) * n * F0 / (R * TKelvin)))*
       FeMolarMass / 1000

    CSat_OP = CSat_OPNew
    CSat_OB = CSat_OBNew
    CSat_MP = CSat_MPNew
    Ce_MP = Ce_MPNew
    Ce_OP = Ce_OPNew
    kd_OB = ked_OB
    kd_OP = ked_OP
    kd = kd_OB

    return (CSat_OP, CSat_OB, CSat_MP, Ce_MP, Ce_OP, kd,
        Ecorr, Emixed, kd_OB, kd_OP, EmixedOP)
################################
# FAC Solver function
# Will introduction spalling and electrochemical
   calculations with iteration
```

```
i=0
#Generates a list of x values representing oxide
   particle size
while i < 10000:
    x = rand.normalvariate(mu, sigma)
    if x > 10.0 and x < 150.0:
        spall.append(x)
        i = i+1

DeltaOX = Delta

for i in range(0,10000):
#Choosing particle diameter for the particular iteration
    'i'

    ParticleDiameter = float(spall[j])

# calculating spalling time, so, the time it would take
   to remove the oxide particle, given the size and
   conditions
    ST1 = 1*ksp*math.pow(ParticleDiameter * 1e-7,1)
    ST2 = (km/100)*(probediameter/100)/(DFe0/10000)*10
    ST3 = PhiOX0 * kd * f0 * (S0 * CSat_OB - Ce_OB)
    SpallingTime = ST1 / (ST2*ST3)
```

```
# Decision point, if the spalling time is less than the
   simulation interval time, and the oxide particle
   diameter is less than half the oxide thickness, then
   a spalling event will occur

    if (DummyTime > SpallingTime and ParticleDiameter *
       1e-7 * RhoOX0 < (DeltaOX/2)):
        DeltaOX = DeltaOX - ParticleDiameter * 1e-7 *
           RhoOX0
        DummyTime = t0
        j = j + 1

    else:
        DummyTime = DummyTime + t0

    DDeltaOX = (DDeltaFunction(DeltaOX, Ce_MP,  CSat_OB,
        CB, Ce_OB, kd))

    # Runge Kutta method for calculating the Oxide
       thickness

    K1 = t0 * float(DDeltaOX)
    K2 = t0 * DDeltaFunction(DeltaOX + (K1 / 2.0), Ce_MP
```

```
        , CSat_OB, CB,Ce_OB, kd)
    K3 = t0 * DDeltaFunction(DeltaOX + (K2 / 2.0), Ce_MP
        ,  CSat_OB, CB,Ce_OB, kd)
    K4 = t0 * DDeltaFunction(DeltaOX + K3, Ce_MP,
        CSat_OB, CB,Ce_OB, kd)
    DeltaOX = (DeltaOX + (K1 + (2.0 * K2) + (2.0 * K3) +
         K4) / 6.0)
    if DeltaOX <= 0.0:
         DeltaOX = 1.0e-5

    DMOX = CorrosionRateFunction(DeltaOX, Ce_MP, CSat_OB
        , CB)
    if DMOX <0.0:
         DMOX = 1e-8

########################################
# Calling Electro-chemistry Function and revising
    concentration values.

    kd = float(data[19][column])
    Y = FACECPCal(kd, CH2coolant, DeltaGFe_Fe2,
        DeltaGFe2p_Fe3O4,DeltaGH2_Hp ,kHenry ,CSat_OB,
        Ce_MP, Ce_OP, Ce_OB,  DeltaOX, DMOX,  TKelvin,
        ConcC4H9ONTotal, ActivationEFe_Fe2_MP,
```

```
        ActivationEH2_Hp_MP, ActivationEH2_Hp_OB,
        ActivationEFe2p_Fe3O4_OB,ActivationEH2_Hp_OP,
        ActivationEFe2p_Fe3O4_OP, pH)
    CSat_MP = float(Y[2])
    CSat_OP = float(Y[0])
    CSat_OB = float(Y[1])
    kd = float(Y[5])
    Ce_MP = float(Y[3])
    Ce_OP = float(Y[4])
    Ecorr = float(Y[6])
    Emixed = float(Y[7])
    EmixedOP = float(Y[9])
    Delta = DeltaOX
    Ce_OB = (0.476 * (1.101 + PhiOX0) * DMOX + (kd * f0
        * S0 * CSat_OB) + km * 0.5*CB) / (km + kd * f0 )

##############################################
    Thickness.append(Delta *10000 /RhoOX0)
    corrosionnrate.append(DMOX *10 * 3600 * 24 *365/
        RhoOX0)
    AverCorRate = DMOX + AverCorRate
    AverThickness = Delta + AverThickness
    Time.append(t0*i/(3600*24))
    kdiss.append(kd)
```

```
    OB_Con.append(Ce_OB)
    OP_Con.append(Ce_OP)
    MP_Con.append(Ce_MP)
    CSAT.append(CSat_OB)
    delta_C = CB-Ce_OB

AverageCe_OB = sum(OB_Con)/10000
AverCorRate = sum(corrosionnrate)/10000
AverThickness =   AverThickness *10000 / (10000.0 *
   RhoOX0)
print 'Average Oxide Thickness:',AverThickness
print 'Average Corrosion Rate:', AverCorRate
print 'Emixed OB: ', Emixed
print 'Emixed MP', Ecorr


plt.figure()
font ={'family':'Computer Modern Roman', 'size':16}
plt.rc('font', **font)
plt.plot(Time,Thickness, '-')
plt.title('Oxide Thickness vs Time')
plt.xlabel('Day')
plt.ylabel('Oxide Thickness (um)')
plt.show()
```

```
plt.figure()
font ={'family':'Computer␣Modern␣Roman', 'size':16}
plt.rc('font', **font)
plt.plot(Time,corrosionnrate, '-')
plt.title('Corrosion␣Rate␣vs␣Time' )
plt.xlabel('Day')
plt.ylabel('Corrosion␣Rate␣(mm/year)')
plt.show()

plt.figure()
font ={'family':'Computer␣Modern␣Roman', 'size':16}
plt.rc('font', **font)
plt.plot(Time,OB_Con, '-')
plt.title('Oxide-Bulk␣Fe␣Concentration␣vs␣Time' )
plt.xlabel('Day')
plt.ylabel('Oxide␣Bulk␣[Fe]␣(ppb)')
plt.show()
```

Appendix B

Appendix B - Model I/O

B.1 Neutral Chemistry, 140°C, 0.5 LPM, No Iron Source, 1.6 mm probe

Parameter	Unit	Predicted Value
FAC Rate	mm/yr	0.848
Oxide Thickness	μm	0.473
Mixed Potential	V	-0.363

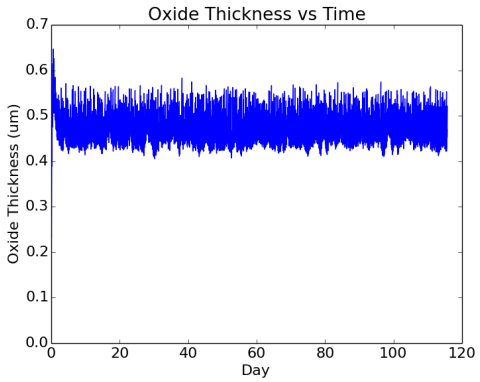

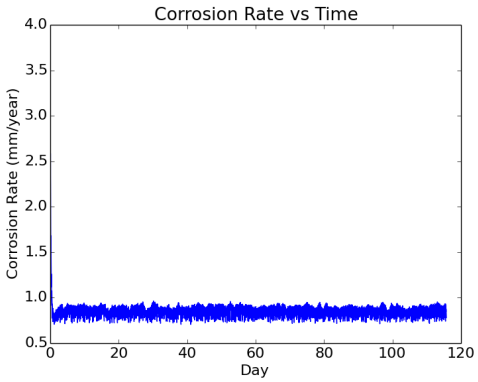

Parameter	Description	Unit	Value
CB	Initial [Fe] in bulk coolant	g/cm^3	1.64^{-9}
$CSatOB$	Initial Fe sol'b at oxide-bulk interface	g/cm^3	1.16^{-7}
$CeOB$	Initial [Fe] at oxide-bulk interface	g/cm^3	1.02^{-7}
$CSatPO$	Initial Fe sol'b at oxide-passivating interface	g/cm^3	3.54^{-7}
$CeOP$	Initial [Fe] at oxide-passivating interface	g/cm^3	3.48^{-7}
$CSatMP$	Initial Fe sol'b at metal-passivating interface	g/cm^3	2.61^{-7}
$CeMP$	Initial [Fe] at metal-passivating interface	g/cm^3	2.18^{-7}
U	Linear velocity of coolant	cm/s	414.5
kd	Dissolution rate constant of magnetite	cm/s	0.15
km	Mass transfer coefficient	cm/s	0.32698
ksp	Spalling time constant	–	851
kCR	Chromium content constant	–	1
$Temperature$	Temperature	$^\circ C$	140
$Tkelvin$	Temperature	K	413.15
$DP0$	Diffusivity of iron in passivating layer	cm^2/s	1.065^{-4}
$DFe0$	Diffusivity of Iron in Water	cm^2/s	1.065^{-4}
$f0$	Surface area factor	–	1.73205
$S0$	Supersaturation factor	–	1.1
$DeltaP0$	Passivating layer thickness	g/cm^2	9.78^{-6}
$ChiPO$	Tortuosity of passivating layer	–	1.8
$PhiPO$	Porosity of passivating layer	–	0.2
$RhoPO$	Density of passivating layer	g/cm^3	5.15
$MP0$	Mass fraction of iron in passivating layer	–	1
$RhoH2O0$	Density of Water	g/cm^3	0.92579
$MFe0$	Mass fraction of iron in oxide	–	0.723569
$RhoFe0$	Density of iron	g/cm^3	7.9
$RhoSteel0$	Density of steel	g/cm^3	7.86
$PhiOX0$	Porosity of oxide layer	–	0.09
$ChiOX0$	Tortuosity of oxide	–	2
$RhoOX0$	Density of oxide	g/cm^3	5.2
$DCORs0$	Initial concentration at oxide bulk	g/cm^3	0
$DOXs0$	Initial oxide layer thickness	g/cm^2	1.20^{-5}

Parameter	Description	Unit	Value
$t0$	Time interval for simulation	s	1000
$tstep0$	Number of steps in model run	–	7000
$Paverage0$	Minimum size of oxide particle	cm	1^{-6}
$SDP0$	Maximum size of oxide particle	cm	1^{-5}
$CrContent0$	Chromium content of pipe material	%	0.019
FF	Friction Factor ($f = 0.316Re^{-0.25}$)	–	0.0237
$CH2Coolant0$	Bulk concentration of hydrogen	cm^3/kg	0
$CorrRateExp0$	Experimental corrosion rate	$\mu m/yr$	875
$iH2_HpOB0$	Current at the oxide-solution interfact	A	1.18^{-12}
$EmixedInitial0$	Initial estimate of mixed potential	V	-0.5
0	Number of electrons transferred	–	2
$F0$	Faraday Constant	C/mol	96485
$R0$	Gas Constant	$J/mol * K$	8.314
$h0$	Planck's Constant	$J * s$	6.63^{-34}
$kboltzman0$	Boltzman Constant	J/K	1.38^{-23}
$Beta0$	Symmetry Factor	–	0.5
$FeMMass0$	$Fe(OH)^2$molar mass	g/mol	90
$H2MMass0$	H_2molar mass	g/mol	2.016
$Ecorrinitial$	Experimental corrosion potential	V	-0.55
$ActEFe_Fe2_MP$	Activation Energy	J/mol	180600
$ActEH2_HpMP$	Activation Energy	J/mol	160000
$ActEH2_HpOB$	Activation Energy	J/mol	215000
$ActEFe2p_Fe3O4_OB$	Activation Energy	J/mol	208000
$ActEFe2p_Fe3O4_OP$	Activation Energy	J/mol	173000
$ActEH2_HpOP$	Activation Energy	J/mol	177000
pH	pH at temperature	–	5.88
MU	Dynamic viscosity	cP	0.1955
$probedia$	Probe internal diameter	cm	0.16

B.2 Neutral Chemistry, 140°C, 0.5 LPM, 25% Iron Source, 1.6 mm probe

Parameter	Unit	Predicted Value
FAC Rate	mm/yr	0.807
Oxide Thickness	μm	0.483
Mixed Potential	V	-0.363

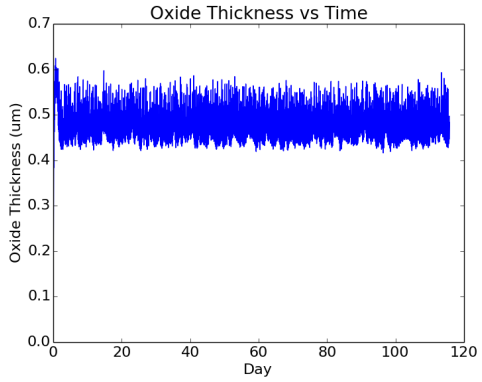

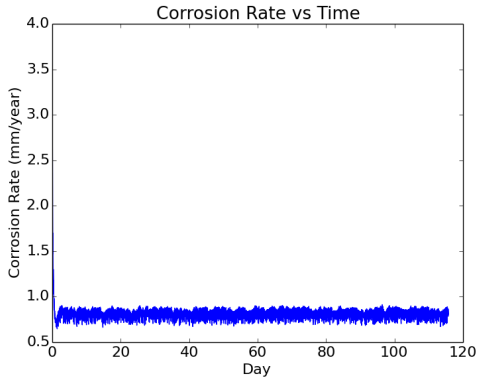

Parameter	Description	Unit	Value
CB	Initial [Fe] in bulk coolant	g/cm^3	4.15^{-9}
$CSatOB$	Initial Fe sol'b at oxide-bulk interface	g/cm^3	1.16^{-7}
$CeOB$	Initial [Fe] at oxide-bulk interface	g/cm^3	1.02^{-7}
$CSatPO$	Initial Fe sol'b at oxide-passivating interface	g/cm^3	3.54^{-7}
$CeOP$	Initial [Fe] at oxide-passivating interface	g/cm^3	3.48^{-7}
$CSatMP$	Initial Fe sol'b at metal-passivating interface	g/cm^3	2.61^{-7}
$CeMP$	Initial [Fe] at metal-passivating interface	g/cm^3	2.18^{-7}
U	Linear velocity of coolant	cm/s	414.5
kd	Dissolution rate constant of magnetite	cm/s	0.15
km	Mass transfer coefficient	cm/s	0.32698
ksp	Spalling time constant	–	851
kCR	Chromium content constant	–	1
$Temperature$	Temperature	$^{\circ}C$	140
$Tkelvin$	Temperature	K	413.15
$DP0$	Diffusivity of iron in passivating layer	cm^2/s	1.065^{-4}
$DFe0$	Diffusivity of Iron in Water	cm^2/s	1.065^{-4}
$f0$	Surface area factor	–	1.73205
$S0$	Supersaturation factor	–	1.1
$DeltaP0$	Passivating layer thickness	g/cm^2	9.78^{-6}
$ChiPO$	Tortuosity of passivating layer	–	1.8
$PhiPO$	Porosity of passivating layer	–	0.2
$RhoPO$	Density of passivating layer	g/cm^3	5.15
$MP0$	Mass fraction of iron in passivating layer	–	1
$RhoH2O0$	Density of Water	g/cm^3	0.92579
$MFe0$	Mass fraction of iron in oxide	–	0.723569
$RhoFe0$	Density of iron	g/cm^3	7.9
$RhoSteel0$	Density of steel	g/cm^3	7.86
$PhiOX0$	Porosity of oxide layer	–	0.09
$ChiOX0$	Tortuosity of oxide	–	2
$RhoOX0$	Density of oxide	g/cm^3	5.2
$DCORs0$	Initial concentration at oxide bulk	g/cm^3	0
$DOXs0$	Initial oxide layer thickness	g/cm^2	1.20^{-5}

Parameter	Description	Unit	Value
$t0$	Time interval for simulation	s	1000
$tstep0$	Number of steps in model run	–	7000
$Paverage0$	Minimum size of oxide particle	cm	1^{-6}
$SDP0$	Maximum size of oxide particle	cm	1^{-5}
$CrContent0$	Chromium content of pipe material	%	0.019
FF	Friction Factor ($f = 0.316Re^{-0.25}$)	–	0.0237
$CH2Coolant0$	Bulk concentration of hydrogen	cm^3/kg	0
$CorrRateExp0$	Experimental corrosion rate	$\mu m/yr$	875
$iH2_HpOB0$	Current at the oxide-solution interfact	A	1.18^{-12}
$EmixedInitial0$	Initial estimate of mixed potential	V	-0.5
0	Number of electrons transferred	–	2
$F0$	Faraday Constant	C/mol	96485
$R0$	Gas Constant	$J/mol * K$	8.314
$h0$	Planck's Constant	$J * s$	6.63^{-34}
$kboltzman0$	Boltzman Constant	J/K	1.38^{-23}
$Beta0$	Symmetry Factor	–	0.5
$FeMMass0$	$Fe(OH)^2$molar mass	g/mol	90
$H2MMass0$	H_2molar mass	g/mol	2.016
$Ecorrinitial$	Experimental corrosion potential	V	-0.55
$ActEFe_Fe2_MP$	Activation Energy	J/mol	180600
$ActEH2_Hp_MP$	Activation Energy	J/mol	160000
$ActEH2_HpOB$	Activation Energy	J/mol	215000
$ActEFe2p_Fe3O4_OB$	Activation Energy	J/mol	208000
$ActEFe2p_Fe3O4_OP$	Activation Energy	J/mol	173000
$ActEH2_HpOP$	Activation Energy	J/mol	177000
pH	pH at temperature	–	5.88
MU	Dynamic viscosity	cP	0.1955
$probedia$	Probe internal diameter	cm	0.16

B.3 Neutral Chemistry, 140°C, 0.5 LPM, 50% Iron Source, 1.6 mm probe

Parameter	Unit	Predicted Value
FAC Rate	mm/yr	0.573
Oxide Thickness	μm	0.541
Mixed Potential	V	-0.376

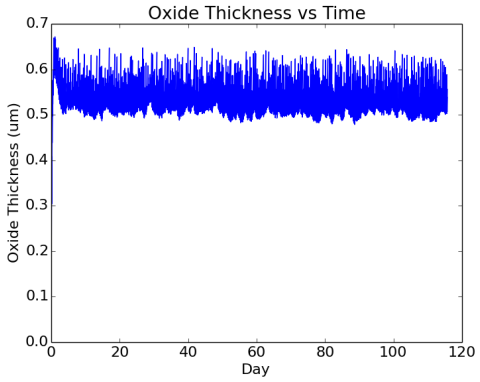

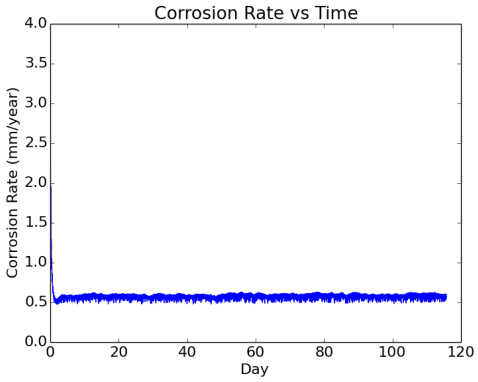

Parameter	Description	Unit	Value
CB	Initial [Fe] in bulk coolant	g/cm^3	2.01^{-8}
$CSatOB$	Initial Fe sol'b at oxide-bulk interface	g/cm^3	1.16^{-7}
$CeOB$	Initial [Fe] at oxide-bulk interface	g/cm^3	1.02^{-7}
$CSatPO$	Initial Fe sol'b at oxide-passivating interface	g/cm^3	3.54^{-7}
$CeOP$	Initial [Fe] at oxide-passivating interface	g/cm^3	3.48^{-7}
$CSatMP$	Initial Fe sol'b at metal-passivating interface	g/cm^3	2.61^{-7}
$CeMP$	Initial [Fe] at metal-passivating interface	g/cm^3	2.18^{-7}
U	Linear velocity of coolant	cm/s	414.5
kd	Dissolution rate constant of magnetite	cm/s	0.15
km	Mass transfer coefficient	cm/s	0.32698
ksp	Spalling time constant	–	851
kCR	Chromium content constant	–	1
$Temperature$	Temperature	$^\circ C$	140
$Tkelvin$	Temperature	K	413.15
$DP0$	Diffusivity of iron in passivating layer	cm^2/s	1.065^{-4}
$DFe0$	Diffusivity of Iron in Water	cm^2/s	1.065^{-4}
$f0$	Surface area factor	–	1.73205
$S0$	Supersaturation factor	–	1.1
$DeltaP0$	Passivating layer thickness	g/cm^2	9.78^{-6}
$ChiPO$	Tortuosity of passivating layer	–	1.8
$PhiPO$	Porosity of passivating layer	–	0.2
$RhoPO$	Density of passivating layer	g/cm^3	5.15
$MP0$	Mass fraction of iron in passivating layer	–	1
$RhoH2O0$	Density of Water	g/cm^3	0.92579
$MFe0$	Mass fraction of iron in oxide	–	0.723569
$RhoFe0$	Density of iron	g/cm^3	7.9
$RhoSteel0$	Density of steel	g/cm^3	7.86
$PhiOX0$	Porosity of oxide layer	–	0.09
$ChiOX0$	Tortuosity of oxide	–	2
$RhoOX0$	Density of oxide	g/cm^3	5.2
$DCORs0$	Initial concentration at oxide bulk	g/cm^3	0
$DOXs0$	Initial oxide layer thickness	g/cm^2	1.20^{-5}

Parameter	Description	Unit	Value
$t0$	Time interval for simulation	s	1000
$tstep0$	Number of steps in model run	–	7000
$Paverage0$	Minimum size of oxide particle	cm	1^{-6}
$SDP0$	Maximum size of oxide particle	cm	1^{-5}
$CrContent0$	Chromium content of pipe material	%	0.019
FF	Friction Factor ($f = 0.316Re^{-0.25}$)	–	0.0237
$CH2Coolant0$	Bulk concentration of hydrogen	cm^3/kg	0
$CorrRateExp0$	Experimental corrosion rate	$\mu m/yr$	875
$iH2_HpOB0$	Current at the oxide-solution interfact	A	1.18^{-12}
$EmixedInitial0$	Initial estimate of mixed potential	V	-0.5
0	Number of electrons transferred	–	2
$F0$	Faraday Constant	C/mol	96485
$R0$	Gas Constant	$J/mol * K$	8.314
$h0$	Planck's Constant	$J * s$	6.63^{-34}
$kboltzman0$	Boltzman Constant	J/K	1.38^{-23}
$Beta0$	Symmetry Factor	–	0.5
$FeMMass0$	$Fe(OH)^2$molar mass	g/mol	90
$H2MMass0$	H_2molar mass	g/mol	2.016
$Ecorrinitial$	Experimental corrosion potential	V	-0.55
$ActEFe_Fe2_MP$	Activation Energy	J/mol	180600
$ActEH2_Hp_MP$	Activation Energy	J/mol	160000
$ActEH2_HpOB$	Activation Energy	J/mol	215000
$ActEFe2p_Fe3O4_OB$	Activation Energy	J/mol	208000
$ActEFe2p_Fe3O4_OP$	Activation Energy	J/mol	173000
$ActEH2_HpOP$	Activation Energy	J/mol	177000
pH	pH at temperature	–	5.88
MU	Dynamic viscosity	cP	0.1955
$probedia$	Probe internal diameter	cm	0.16

B.4 Neutral Chemistry, 140°C, 0.5 LPM, 100% Iron Source, 1.6 mm probe

Parameter	Unit	Predicted Value
FAC Rate	mm/yr	0.484
Oxide Thickness	μm	0.541
Mixed Potential	V	-0.381

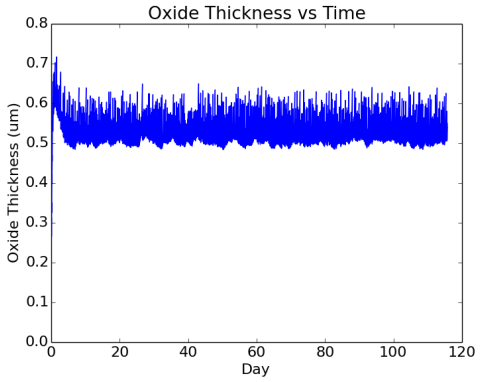

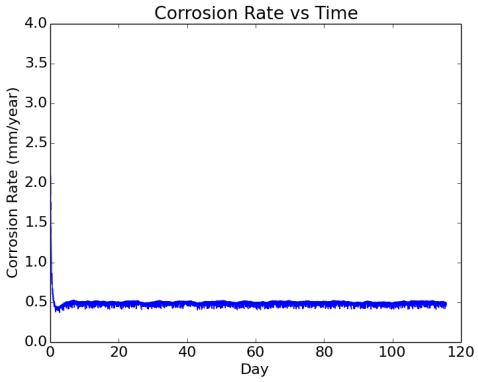

Parameter	Description	Unit	Value
CB	Initial [Fe] in bulk coolant	g/cm^3	3.03^{-8}
$CSatOB$	Initial Fe sol'b at oxide-bulk interface	g/cm^3	1.16^{-7}
$CeOB$	Initial [Fe] at oxide-bulk interface	g/cm^3	1.02^{-7}
$CSatPO$	Initial Fe sol'b at oxide-passivating interface	g/cm^3	3.54^{-7}
$CeOP$	Initial [Fe] at oxide-passivating interface	g/cm^3	3.48^{-7}
$CSatMP$	Initial Fe sol'b at metal-passivating interface	g/cm^3	2.61^{-7}
$CeMP$	Initial [Fe] at metal-passivating interface	g/cm^3	2.18^{-7}
U	Linear velocity of coolant	cm/s	414.5
kd	Dissolution rate constant of magnetite	cm/s	0.15
km	Mass transfer coefficient	cm/s	0.32698
ksp	Spalling time constant	–	851
kCR	Chromium content constant	–	1
$Temperature$	Temperature	$^\circ C$	140
$Tkelvin$	Temperature	K	413.15
$DP0$	Diffusivity of iron in passivating layer	cm^2/s	1.065^{-4}
$DFe0$	Diffusivity of Iron in Water	cm^2/s	1.065^{-4}
$f0$	Surface area factor	–	1.73205
$S0$	Supersaturation factor	–	1.1
$DeltaP0$	Passivating layer thickness	g/cm^2	9.78^{-6}
$ChiPO$	Tortuosity of passivating layer	–	1.8
$PhiPO$	Porosity of passivating layer	–	0.2
$RhoPO$	Density of passivating layer	g/cm^3	5.15
$MP0$	Mass fraction of iron in passivating layer	–	1
$RhoH2O0$	Density of Water	g/cm^3	0.92579
$MFe0$	Mass fraction of iron in oxide	–	0.723569
$RhoFe0$	Density of iron	g/cm^3	7.9
$RhoSteel0$	Density of steel	g/cm^3	7.86
$PhiOX0$	Porosity of oxide layer	–	0.09
$ChiOX0$	Tortuosity of oxide	–	2
$RhoOX0$	Density of oxide	g/cm^3	5.2
$DCORs0$	Initial concentration at oxide bulk	g/cm^3	0
$DOXs0$	Initial oxide layer thickness	g/cm^2	1.20^{-5}

Parameter	Description	Unit	Value
$t0$	Time interval for simulation	s	1000
$tstep0$	Number of steps in model run	–	7000
$Paverage0$	Minimum size of oxide particle	cm	1^{-6}
$SDP0$	Maximum size of oxide particle	cm	1^{-5}
$CrContent0$	Chromium content of pipe material	%	0.019
FF	Friction Factor ($f = 0.316Re^{-0.25}$)	–	0.0237
$CH2Coolant0$	Bulk concentration of hydrogen	cm^3/kg	0
$CorrRateExp0$	Experimental corrosion rate	$\mu m/yr$	875
$iH2_HpOB0$	Current at the oxide-solution interfact	A	1.18^{-12}
$EmixedInitial0$	Initial estimate of mixed potential	V	-0.5
0	Number of electrons transferred	–	2
$F0$	Faraday Constant	C/mol	96485
$R0$	Gas Constant	$J/mol * K$	8.314
$h0$	Planck's Constant	$J * s$	6.63^{-34}
$kboltzman0$	Boltzman Constant	J/K	1.38^{-23}
$Beta0$	Symmetry Factor	–	0.5
$FeMMass0$	$Fe(OH)^2$molar mass	g/mol	90
$H2MMass0$	H_2molar mass	g/mol	2.016
$Ecorrinitial$	Experimental corrosion potential	V	-0.55
$ActEFe_Fe2_MP$	Activation Energy	J/mol	180600
$ActEH2_HpMP$	Activation Energy	J/mol	160000
$ActEH2_HpOB$	Activation Energy	J/mol	215000
$ActEFe2p_Fe3O4_OB$	Activation Energy	J/mol	208000
$ActEFe2p_Fe3O4_OP$	Activation Energy	J/mol	173000
$ActEH2_HpOP$	Activation Energy	J/mol	177000
pH	pH at temperature	–	5.88
MU	Dynamic viscosity	cP	0.1955
$probedia$	Probe internal diameter	cm	0.16

B.5 Neutral Chemistry, 140°C, 0.85 LPM, No Iron Source, 1.6 mm probe

Parameter	Unit	Predicted Value
FAC Rate	mm/yr	2.750
Oxide Thickness	μm	0.224
Mixed Potential	V	-0.317

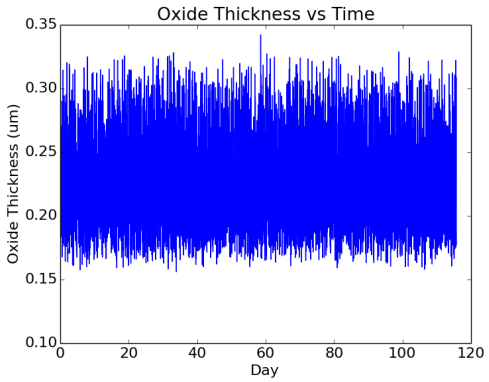

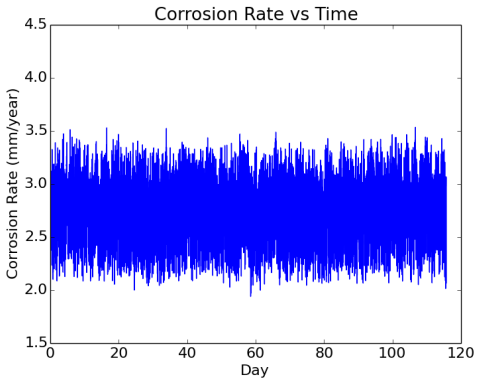

Parameter	Description	Unit	Value
CB	Initial [Fe] in bulk coolant	g/cm^3	1.64^{-9}
$CSatOB$	Initial Fe sol'b at oxide-bulk interface	g/cm^3	1.16^{-7}
$CeOB$	Initial [Fe] at oxide-bulk interface	g/cm^3	1.02^{-7}
$CSatPO$	Initial Fe sol'b at oxide-passivating interface	g/cm^3	3.54^{-7}
$CeOP$	Initial [Fe] at oxide-passivating interface	g/cm^3	3.48^{-7}
$CSatMP$	Initial Fe sol'b at metal-passivating interface	g/cm^3	2.61^{-7}
$CeMP$	Initial [Fe] at metal-passivating interface	g/cm^3	2.18^{-7}
U	Linear velocity of coolant	cm/s	663.15
kd	Dissolution rate constant of magnetite	cm/s	0.15
km	Mass transfer coefficient	cm/s	0.352
ksp	Spalling time constant	–	35
kCR	Chromium content constant	–	1
$Temperature$	Temperature	$^\circ C$	140
$Tkelvin$	Temperature	K	413.15
$DP0$	Diffusivity of iron in passivating layer	cm^2/s	1.065^{-4}
$DFe0$	Diffusivity of Iron in Water	cm^2/s	1.065^{-4}
$f0$	Surface area factor	–	1.73205
$S0$	Supersaturation factor	–	1.1
$DeltaP0$	Passivating layer thickness	g/cm^2	9.78^{-6}
$ChiPO$	Tortuosity of passivating layer	–	1.8
$PhiPO$	Porosity of passivating layer	–	0.2
$RhoPO$	Density of passivating layer	g/cm^3	5.15
$MP0$	Mass fraction of iron in passivating layer	–	1
$RhoH2O0$	Density of Water	g/cm^3	0.92579
$MFe0$	Mass fraction of iron in oxide	–	0.723569
$RhoFe0$	Density of iron	g/cm^3	7.9
$RhoSteel0$	Density of steel	g/cm^3	7.86
$PhiOX0$	Porosity of oxide layer	–	0.09
$ChiOX0$	Tortuosity of oxide	–	2
$RhoOX0$	Density of oxide	g/cm^3	5.2
$DCORs0$	Initial concentration at oxide bulk	g/cm^3	0
$DOXs0$	Initial oxide layer thickness	g/cm^2	1.20^{-5}

Parameter	Description	Unit	Value
$t0$	Time interval for simulation	s	1000
$tstep0$	Number of steps in model run	–	7000
$Paverage0$	Minimum size of oxide particle	cm	1^{-6}
$SDP0$	Maximum size of oxide particle	cm	1^{-5}
$CrContent0$	Chromium content of pipe material	%	0.019
FF	Friction Factor ($f = 0.316Re^{-0.25}$)	–	0.0237
$CH2Coolant0$	Bulk concentration of hydrogen	cm^3/kg	0
$CorrRateExp0$	Experimental corrosion rate	$\mu m/yr$	2750
$iH2_HpOB0$	Current at the oxide-solution interfact	A	1.18^{-12}
$EmixedInitial0$	Initial estimate of mixed potential	V	-0.5
0	Number of electrons transferred	–	2
$F0$	Faraday Constant	C/mol	96485
$R0$	Gas Constant	$J/mol * K$	8.314
$h0$	Planck's Constant	$J * s$	6.63^{-34}
$kboltzman0$	Boltzman Constant	J/K	1.38^{-23}
$Beta0$	Symmetry Factor	–	0.5
$FeMMass0$	$Fe(OH)^2$molar mass	g/mol	90
$H2MMass0$	H_2molar mass	g/mol	2.016
$Ecorrinitial$	Experimental corrosion potential	V	-0.55
$ActEFe_Fe2_MP$	Activation Energy	J/mol	180600
$ActEH2_Hp_MP$	Activation Energy	J/mol	160000
$ActEH2_HpOB$	Activation Energy	J/mol	215000
$ActEFe2p_Fe3O4_OB$	Activation Energy	J/mol	208000
$ActEFe2p_Fe3O4_OP$	Activation Energy	J/mol	173000
$ActEH2_HpOP$	Activation Energy	J/mol	177000
pH	pH at temperature	–	5.88
MU	Dynamic viscosity	cP	0.1955
$probedia$	Probe internal diameter	cm	0.16

B.6 Neutral Chemistry, 140°C, 0.85 LPM, 25% Iron Source, 1.6 mm probe

Parameter	Unit	Predicted Value
FAC Rate	mm/yr	2.669
Oxide Thickness	μm	0.221
Mixed Potential	V	-0.317

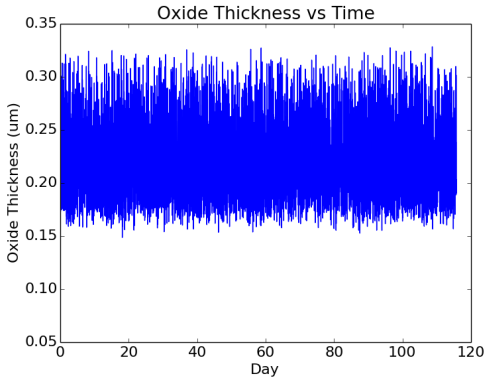

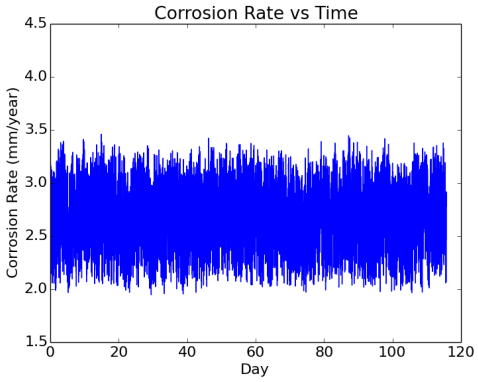

Parameter	Description	Unit	Value
CB	Initial [Fe] in bulk coolant	g/cm^3	1.01^{-8}
$CSatOB$	Initial Fe sol'b at oxide-bulk interface	g/cm^3	1.16^{-7}
$CeOB$	Initial [Fe] at oxide-bulk interface	g/cm^3	1.02^{-7}
$CSatPO$	Initial Fe sol'b at oxide-passivating interface	g/cm^3	3.54^{-7}
$CeOP$	Initial [Fe] at oxide-passivating interface	g/cm^3	3.48^{-7}
$CSatMP$	Initial Fe sol'b at metal-passivating interface	g/cm^3	2.61^{-7}
$CeMP$	Initial [Fe] at metal-passivating interface	g/cm^3	2.18^{-7}
U	Linear velocity of coolant	cm/s	663.15
kd	Dissolution rate constant of magnetite	cm/s	0.15
km	Mass transfer coefficient	cm/s	0.352
ksp	Spalling time constant	–	35
kCR	Chromium content constant	–	1
$Temperature$	Temperature	$^\circ C$	140
$Tkelvin$	Temperature	K	413.15
$DP0$	Diffusivity of iron in passivating layer	cm^2/s	1.065^{-4}
$DFe0$	Diffusivity of Iron in Water	cm^2/s	1.065^{-4}
$f0$	Surface area factor	–	1.73205
$S0$	Supersaturation factor	–	1.1
$DeltaP0$	Passivating layer thickness	g/cm^2	9.78^{-6}
$ChiPO$	Tortuosity of passivating layer	–	1.8
$PhiPO$	Porosity of passivating layer	–	0.2
$RhoPO$	Density of passivating layer	g/cm^3	5.15
$MP0$	Mass fraction of iron in passivating layer	–	1
$RhoH2O0$	Density of Water	g/cm^3	0.92579
$MFe0$	Mass fraction of iron in oxide	–	0.723569
$RhoFe0$	Density of iron	g/cm^3	7.9
$RhoSteel0$	Density of steel	g/cm^3	7.86
$PhiOX0$	Porosity of oxide layer	–	0.09
$ChiOX0$	Tortuosity of oxide	–	2
$RhoOX0$	Density of oxide	g/cm^3	5.2
$DCORs0$	Initial concentration at oxide bulk	g/cm^3	0
$DOXs0$	Initial oxide layer thickness	g/cm^2	1.20^{-5}

Parameter	Description	Unit	Value
$t0$	Time interval for simulation	s	1000
$tstep0$	Number of steps in model run	–	7000
$Paverage0$	Minimum size of oxide particle	cm	1^{-6}
$SDP0$	Maximum size of oxide particle	cm	1^{-5}
$CrContent0$	Chromium content of pipe material	%	0.019
FF	Friction Factor ($f = 0.316Re^{-0.25}$)	–	0.0237
$CH2Coolant0$	Bulk concentration of hydrogen	cm^3/kg	0
$CorrRateExp0$	Experimental corrosion rate	$\mu m/yr$	2750
$iH2_HpOB0$	Current at the oxide-solution interfact	A	1.18^{-12}
$EmixedInitial0$	Initial estimate of mixed potential	V	-0.5
0	Number of electrons transferred	–	2
$F0$	Faraday Constant	C/mol	96485
$R0$	Gas Constant	$J/mol * K$	8.314
$h0$	Planck's Constant	$J * s$	6.63^{-34}
$kboltzman0$	Boltzman Constant	J/K	1.38^{-23}
$Beta0$	Symmetry Factor	–	0.5
$FeMMass0$	$Fe(OH)^2$molar mass	g/mol	90
$H2MMass0$	H_2molar mass	g/mol	2.016
$Ecorrinitial$	Experimental corrosion potential	V	-0.55
$ActEFe_Fe2_MP$	Activation Energy	J/mol	180600
$ActEH2_Hp_MP$	Activation Energy	J/mol	160000
$ActEH2_HpOB$	Activation Energy	J/mol	215000
$ActEFe2p_Fe3O4_OB$	Activation Energy	J/mol	208000
$ActEFe2p_Fe3O4_OP$	Activation Energy	J/mol	173000
$ActEH2_HpOP$	Activation Energy	J/mol	177000
pH	pH at temperature	–	5.88
MU	Dynamic viscosity	cP	0.1955
$probedia$	Probe internal diameter	cm	0.16

B.7 Neutral Chemistry, 140°C, 0.85 LPM, 50% Iron Source, 1.6 mm probe

Parameter	Unit	Predicted Value
FAC Rate	mm/yr	2.157
Oxide Thickness	μm	0.198
Mixed Potential	V	-0.333

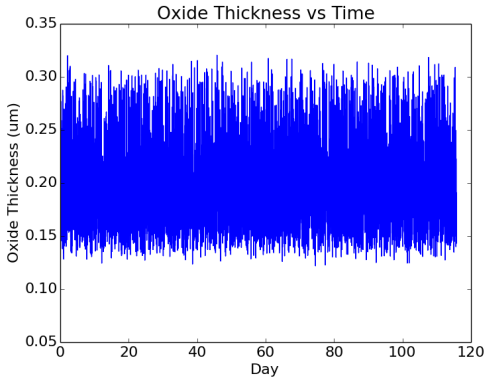

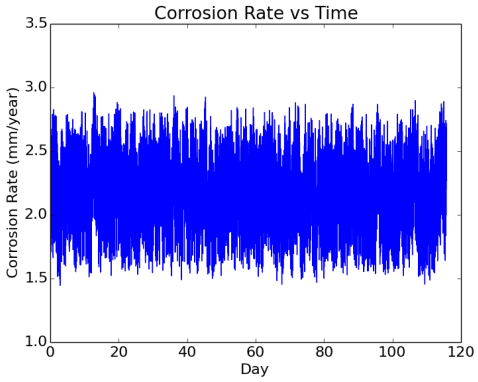

Parameter	Description	Unit	Value
CB	Initial [Fe] in bulk coolant	g/cm^3	6.61^{-8}
$CSatOB$	Initial Fe sol'b at oxide-bulk interface	g/cm^3	1.16^{-7}
$CeOB$	Initial [Fe] at oxide-bulk interface	g/cm^3	1.02^{-7}
$CSatPO$	Initial Fe sol'b at oxide-passivating interface	g/cm^3	3.54^{-7}
$CeOP$	Initial [Fe] at oxide-passivating interface	g/cm^3	3.48^{-7}
$CSatMP$	Initial Fe sol'b at metal-passivating interface	g/cm^3	2.61^{-7}
$CeMP$	Initial [Fe] at metal-passivating interface	g/cm^3	2.18^{-7}
U	Linear velocity of coolant	cm/s	663.15
kd	Dissolution rate constant of magnetite	cm/s	0.15
km	Mass transfer coefficient	cm/s	0.352
ksp	Spalling time constant	–	35
kCR	Chromium content constant	–	1
$Temperature$	Temperature	$^\circ C$	140
$Tkelvin$	Temperature	K	413.15
$DP0$	Diffusivity of iron in passivating layer	cm^2/s	1.065^{-4}
$DFe0$	Diffusivity of Iron in Water	cm^2/s	1.065^{-4}
$f0$	Surface area factor	–	1.73205
$S0$	Supersaturation factor	–	1.1
$DeltaP0$	Passivating layer thickness	g/cm^2	9.78^{-6}
$ChiPO$	Tortuosity of passivating layer	–	1.8
$PhiPO$	Porosity of passivating layer	–	0.2
$RhoPO$	Density of passivating layer	g/cm^3	5.15
$MP0$	Mass fraction of iron in passivating layer	–	1
$RhoH2O0$	Density of Water	g/cm^3	0.92579
$MFe0$	Mass fraction of iron in oxide	–	0.723569
$RhoFe0$	Density of iron	g/cm^3	7.9
$RhoSteel0$	Density of steel	g/cm^3	7.86
$PhiOX0$	Porosity of oxide layer	–	0.09
$ChiOX0$	Tortuosity of oxide	–	2
$RhoOX0$	Density of oxide	g/cm^3	5.2
$DCORs0$	Initial concentration at oxide bulk	g/cm^3	0
$DOXs0$	Initial oxide layer thickness	g/cm^2	1.20^{-5}

Parameter	Description	Unit	Value
$t0$	Time interval for simulation	s	1000
$tstep0$	Number of steps in model run	–	7000
$Paverage0$	Minimum size of oxide particle	cm	1^{-6}
$SDP0$	Maximum size of oxide particle	cm	1^{-5}
$CrContent0$	Chromium content of pipe material	%	0.019
FF	Friction Factor ($f = 0.316Re^{-0.25}$)	–	0.0237
$CH2Coolant0$	Bulk concentration of hydrogen	cm^3/kg	0
$CorrRateExp0$	Experimental corrosion rate	$\mu m/yr$	2750
$iH2_HpOB0$	Current at the oxide-solution interfact	A	1.18^{-12}
$EmixedInitial0$	Initial estimate of mixed potential	V	-0.5
0	Number of electrons transferred	–	2
$F0$	Faraday Constant	C/mol	96485
$R0$	Gas Constant	$J/mol * K$	8.314
$h0$	Planck's Constant	$J * s$	6.63^{-34}
$kboltzman0$	Boltzman Constant	J/K	1.38^{-23}
$Beta0$	Symmetry Factor	–	0.5
$FeMMass0$	$Fe(OH)^2$molar mass	g/mol	90
$H2MMass0$	H_2molar mass	g/mol	2.016
$Ecorrinitial$	Experimental corrosion potential	V	-0.55
$ActEFe_Fe2_MP$	Activation Energy	J/mol	180600
$ActEH2_Hp_MP$	Activation Energy	J/mol	160000
$ActEH2_Hp_OB$	Activation Energy	J/mol	215000
$ActEFe2p_Fe3O4_OB$	Activation Energy	J/mol	208000
$ActEFe2p_Fe3O4_OP$	Activation Energy	J/mol	173000
$ActEH2_Hp_OP$	Activation Energy	J/mol	177000
pH	pH at temperature	–	5.88
MU	Dynamic viscosity	cP	0.1955
$probedia$	Probe internal diameter	cm	0.16

B.8 Neutral Chemistry, 140°C, 0.85 LPM, 100% Iron Source, 1.6 mm probe

Parameter	Unit	Predicted Value
FAC Rate	mm/yr	1.703
Oxide Thickness	μm	0.184
Mixed Potential	V	-0.337

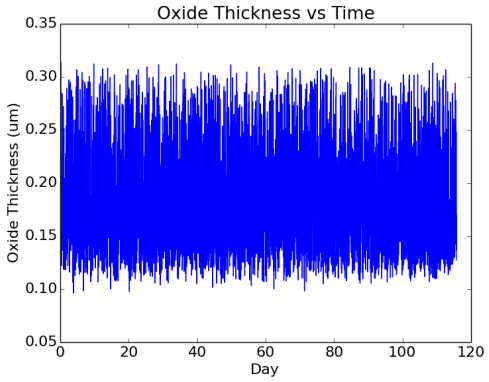

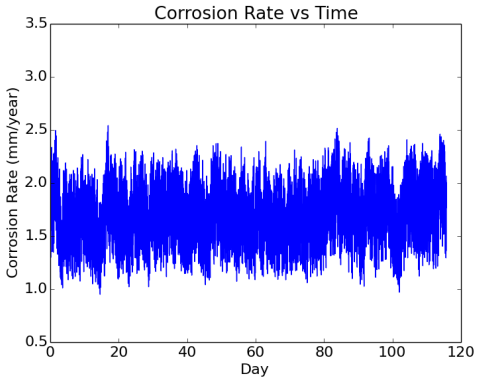

Parameter	Description	Unit	Value
CB	Initial [Fe] in bulk coolant	g/cm^3	1.01^{-7}
$CSatOB$	Initial Fe sol'b at oxide-bulk interface	g/cm^3	1.16^{-7}
$CeOB$	Initial [Fe] at oxide-bulk interface	g/cm^3	1.02^{-7}
$CSatPO$	Initial Fe sol'b at oxide-passivating interface	g/cm^3	3.54^{-7}
$CeOP$	Initial [Fe] at oxide-passivating interface	g/cm^3	3.48^{-7}
$CSatMP$	Initial Fe sol'b at metal-passivating interface	g/cm^3	2.61^{-7}
$CeMP$	Initial [Fe] at metal-passivating interface	g/cm^3	2.18^{-7}
U	Linear velocity of coolant	cm/s	663.15
kd	Dissolution rate constant of magnetite	cm/s	0.15
km	Mass transfer coefficient	cm/s	0.352
ksp	Spalling time constant	–	35
kCR	Chromium content constant	–	1
$Temperature$	Temperature	$^\circ C$	140
$Tkelvin$	Temperature	K	413.15
$DP0$	Diffusivity of iron in passivating layer	cm^2/s	1.065^{-4}
$DFe0$	Diffusivity of Iron in Water	cm^2/s	1.065^{-4}
$f0$	Surface area factor	–	1.73205
$S0$	Supersaturation factor	–	1.1
$DeltaP0$	Passivating layer thickness	g/cm^2	9.78^{-6}
$ChiPO$	Tortuosity of passivating layer	–	1.8
$PhiPO$	Porosity of passivating layer	–	0.2
$RhoPO$	Density of passivating layer	g/cm^3	5.15
$MP0$	Mass fraction of iron in passivating layer	–	1
$RhoH2O0$	Density of Water	g/cm^3	0.92579
$MFe0$	Mass fraction of iron in oxide	–	0.723569
$RhoFe0$	Density of iron	g/cm^3	7.9
$RhoSteel0$	Density of steel	g/cm^3	7.86
$PhiOX0$	Porosity of oxide layer	–	0.09
$ChiOX0$	Tortuosity of oxide	–	2
$RhoOX0$	Density of oxide	g/cm^3	5.2
$DCORs0$	Initial concentration at oxide bulk	g/cm^3	0
$DOXs0$	Initial oxide layer thickness	g/cm^2	1.20^{-5}

Parameter	Description	Unit	Value
$t0$	Time interval for simulation	s	1000
$tstep0$	Number of steps in model run	–	7000
$Paverage0$	Minimum size of oxide particle	cm	1^{-6}
$SDP0$	Maximum size of oxide particle	cm	1^{-5}
$CrContent0$	Chromium content of pipe material	%	0.019
FF	Friction Factor ($f = 0.316Re^{-0.25}$)	–	0.0237
$CH2Coolant0$	Bulk concentration of hydrogen	cm^3/kg	0
$CorrRateExp0$	Experimental corrosion rate	$\mu m/yr$	2750
$iH2_HpOB0$	Current at the oxide-solution interfact	A	1.18^{-12}
$EmixedInitial0$	Initial estimate of mixed potential	V	-0.5
0	Number of electrons transferred	–	2
$F0$	Faraday Constant	C/mol	96485
$R0$	Gas Constant	$J/mol * K$	8.314
$h0$	Planck's Constant	$J * s$	6.63^{-34}
$kboltzman0$	Boltzman Constant	J/K	1.38^{-23}
$Beta0$	Symmetry Factor	–	0.5
$FeMMass0$	$Fe(OH)^2$molar mass	g/mol	90
$H2MMass0$	H_2molar mass	g/mol	2.016
$Ecorrinitial$	Experimental corrosion potential	V	-0.55
$ActEFe_Fe2_MP$	Activation Energy	J/mol	180600
$ActEH2_Hp_MP$	Activation Energy	J/mol	160000
$ActEH2_HpOB$	Activation Energy	J/mol	215000
$ActEFe2p_Fe3O4_OB$	Activation Energy	J/mol	208000
$ActEFe2p_Fe3O4_OP$	Activation Energy	J/mol	173000
$ActEH2_HpOP$	Activation Energy	J/mol	177000
pH	pH at temperature	–	5.88
MU	Dynamic viscosity	cP	0.1955
$probedia$	Probe internal diameter	cm	0.16

B.9 Neutral Chemistry, 200°C, 0.85 LPM, No Iron Source, 1.6 mm probe

Parameter	Unit	Predicted Value
FAC Rate	mm/yr	0.659
Oxide Thickness	μm	3.20
Mixed Potential	V	-0.499

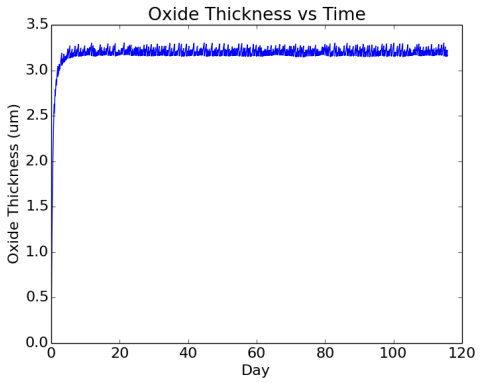

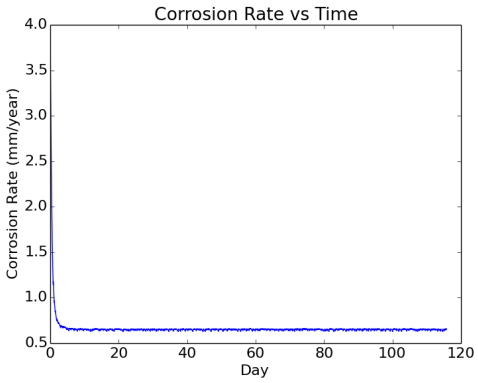

Parameter	Description	Unit	Value
CB	Initial [Fe] in bulk coolant	g/cm^3	1.64^{-9}
$CSatOB$	Initial Fe sol'b at oxide-bulk interface	g/cm^3	6.9^{-8}
$CeOB$	Initial [Fe] at oxide-bulk interface	g/cm^3	6.04^{-8}
$CSatPO$	Initial Fe sol'b at oxide-passivating interface	g/cm^3	2.10^{-7}
$CeOP$	Initial [Fe] at oxide-passivating interface	g/cm^3	2.07^{-7}
$CSatMP$	Initial Fe sol'b at metal-passivating interface	g/cm^3	1.55^{-7}
$CeMP$	Initial [Fe] at metal-passivating interface	g/cm^3	1.29^{-7}
U	Linear velocity of coolant	cm/s	663.15
kd	Dissolution rate constant of magnetite	cm/s	0.05
km	Mass transfer coefficient	cm/s	0.562
ksp	Spalling time constant	–	4600
kCR	Chromium content constant	–	1
$Temperature$	Temperature	$^\circ C$	200
$Tkelvin$	Temperature	K	473.15
$DP0$	Diffusivity of iron in passivating layer	cm^2/s	1.780^{-4}
$DFe0$	Diffusivity of Iron in Water	cm^2/s	1.780^{-4}
$f0$	Surface area factor	–	1.73205
$S0$	Supersaturation factor	–	1.1
$DeltaP0$	Passivating layer thickness	g/cm^2	9.78^{-6}
$ChiPO$	Tortuosity of passivating layer	–	1.8
$PhiPO$	Porosity of passivating layer	–	0.2
$RhoPO$	Density of passivating layer	g/cm^3	5.15
$MP0$	Mass fraction of iron in passivating layer	–	1
$RhoH2O0$	Density of Water	g/cm^3	0.86845
$MFe0$	Mass fraction of iron in oxide	–	0.723569
$RhoFe0$	Density of iron	g/cm^3	7.9
$RhoSteel0$	Density of steel	g/cm^3	7.86
$PhiOX0$	Porosity of oxide layer	–	0.07
$ChiOX0$	Tortuosity of oxide	–	1.5
$RhoOX0$	Density of oxide	g/cm^3	5.2
$DCORs0$	Initial concentration at oxide bulk	g/cm^3	0
$DOXs0$	Initial oxide layer thickness	g/cm^2	1.20^{-5}

Parameter	Description	Unit	Value
$t0$	Time interval for simulation	s	1000
$tstep0$	Number of steps in model run	–	7000
$Paverage0$	Minimum size of oxide particle	cm	1^{-6}
$SDP0$	Maximum size of oxide particle	cm	1^{-5}
$CrContent0$	Chromium content of pipe material	%	0.019
FF	Friction Factor ($f = 0.316Re^{-0.25}$)	–	0.0237
$CH2Coolant0$	Bulk concentration of hydrogen	cm^3/kg	0
$CorrRateExp0$	Experimental corrosion rate	$\mu m/yr$	660
$iH2_HpOB0$	Current at the oxide-solution interfact	A	1.18^{-12}
$EmixedInitial0$	Initial estimate of mixed potential	V	-0.5
0	Number of electrons transferred	–	2
$F0$	Faraday Constant	C/mol	96485
$R0$	Gas Constant	$J/mol * K$	8.314
$h0$	Planck's Constant	$J * s$	6.63^{-34}
$kboltzman0$	Boltzman Constant	J/K	1.38^{-23}
$Beta0$	Symmetry Factor	–	0.5
$FeMMass0$	$Fe(OH)^2$molar mass	g/mol	90
$H2MMass0$	H_2molar mass	g/mol	2.016
$Ecorrinitial$	Experimental corrosion potential	V	-0.55
$ActEFe_Fe2_MP$	Activation Energy	J/mol	180600
$ActEH2_Hp_MP$	Activation Energy	J/mol	160000
$ActEH2_HpOB$	Activation Energy	J/mol	215000
$ActEFe2p_Fe3O4_OB$	Activation Energy	J/mol	208000
$ActEFe2p_Fe3O4_OP$	Activation Energy	J/mol	173000
$ActEH2_HpOP$	Activation Energy	J/mol	177000
pH	pH at temperature	–	6.5
MU	Dynamic viscosity	cP	0.1339
$probedia$	Probe internal diameter	cm	0.16

B.10 Neutral Chemistry, 200°C, 0.5 LPM, No Iron Source, 1.6 mm probe

Parameter	Unit	Predicted Value
FAC Rate	mm/yr	0.496
Oxide Thickness	μm	3.767
Mixed Potential	V	-0.501

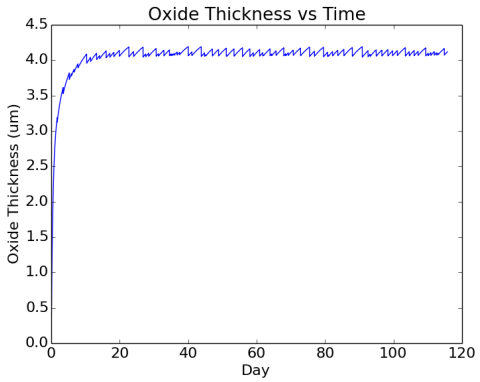

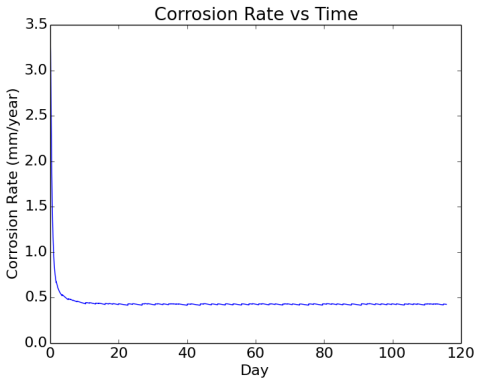

Parameter	Description	Unit	Value
CB	Initial [Fe] in bulk coolant	g/cm^3	1.64^{-9}
$CSatOB$	Initial Fe sol'b at oxide-bulk interface	g/cm^3	6.9^{-8}
$CeOB$	Initial [Fe] at oxide-bulk interface	g/cm^3	6.04^{-8}
$CSatPO$	Initial Fe sol'b at oxide-passivating interface	g/cm^3	2.10^{-7}
$CeOP$	Initial [Fe] at oxide-passivating interface	g/cm^3	2.07^{-7}
$CSatMP$	Initial Fe sol'b at metal-passivating interface	g/cm^3	1.55^{-7}
$CeMP$	Initial [Fe] at metal-passivating interface	g/cm^3	1.29^{-7}
U	Linear velocity of coolant	cm/s	414.15
kd	Dissolution rate constant of magnetite	cm/s	0.05
km	Mass transfer coefficient	cm/s	0.357
ksp	Spalling time constant	–	4600
kCR	Chromium content constant	–	1
$Temperature$	Temperature	$^\circ C$	200
$Tkelvin$	Temperature	K	473.15
$DP0$	Diffusivity of iron in passivating layer	cm^2/s	1.780^{-4}
$DFe0$	Diffusivity of Iron in Water	cm^2/s	1.780^{-4}
$f0$	Surface area factor	–	1.73205
$S0$	Supersaturation factor	–	1.1
$DeltaP0$	Passivating layer thickness	g/cm^2	9.78^{-6}
$ChiPO$	Tortuosity of passivating layer	–	1.8
$PhiPO$	Porosity of passivating layer	–	0.2
$RhoPO$	Density of passivating layer	g/cm^3	5.15
$MP0$	Mass fraction of iron in passivating layer	–	1
$RhoH2O0$	Density of Water	g/cm^3	0.86845
$MFe0$	Mass fraction of iron in oxide	–	0.723569
$RhoFe0$	Density of iron	g/cm^3	7.9
$RhoSteel0$	Density of steel	g/cm^3	7.86
$PhiOX0$	Porosity of oxide layer	–	0.07
$ChiOX0$	Tortuosity of oxide	–	1.5
$RhoOX0$	Density of oxide	g/cm^3	5.2
$DCORs0$	Initial concentration at oxide bulk	g/cm^3	0
$DOXs0$	Initial oxide layer thickness	g/cm^2	1.20^{-5}

Parameter	Description	Unit	Value
$t0$	Time interval for simulation	s	1000
$tstep0$	Number of steps in model run	–	7000
$Paverage0$	Minimum size of oxide particle	cm	1^{-6}
$SDP0$	Maximum size of oxide particle	cm	1^{-5}
$CrContent0$	Chromium content of pipe material	%	0.019
FF	Friction Factor ($f = 0.316Re^{-0.25}$)	–	0.0237
$CH2Coolant0$	Bulk concentration of hydrogen	cm^3/kg	0
$CorrRateExp0$	Experimental corrosion rate	$\mu m/yr$	660
$iH2_HpOB0$	Current at the oxide-solution interfact	A	1.18^{-12}
$EmixedInitial0$	Initial estimate of mixed potential	V	-0.5
0	Number of electrons transferred	–	2
$F0$	Faraday Constant	C/mol	96485
$R0$	Gas Constant	$J/mol * K$	8.314
$h0$	Planck's Constant	$J * s$	6.63^{-34}
$kboltzman0$	Boltzman Constant	J/K	1.38^{-23}
$Beta0$	Symmetry Factor	–	0.5
$FeMMass0$	$Fe(OH)^2$molar mass	g/mol	90
$H2MMass0$	H_2molar mass	g/mol	2.016
$Ecorrinitial$	Experimental corrosion potential	V	-0.55
$ActEFe_Fe2_MP$	Activation Energy	J/mol	180600
$ActEH2_Hp_MP$	Activation Energy	J/mol	160000
$ActEH2_HpOB$	Activation Energy	J/mol	215000
$ActEFe2p_Fe3O4_OB$	Activation Energy	J/mol	208000
$ActEFe2p_Fe3O4_OP$	Activation Energy	J/mol	173000
$ActEH2_HpOP$	Activation Energy	J/mol	177000
pH	pH at temperature	–	6.5
MU	Dynamic viscosity	cP	0.1339
$probedia$	Probe internal diameter	cm	0.16

B.11 pH 9.2 Chemistry, 140°C, 0.85 LPM, No Iron Source, 1.6 mm probe

Parameter	Unit	Predicted Value
FAC Rate	mm/yr	0.440
Oxide Thickness	μm	2.399
Mixed Potential	V	-0.383

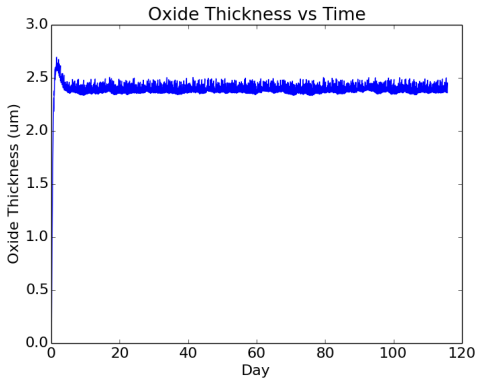

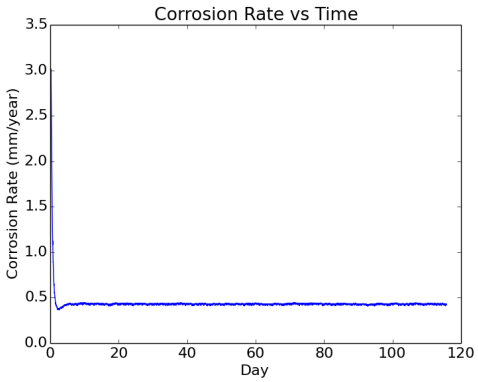

Parameter	Description	Unit	Value
CB	Initial [Fe] in bulk coolant	g/cm^3	1.64^{-9}
$CSatOB$	Initial Fe sol'b at oxide-bulk interface	g/cm^3	1.3^{-8}
$CeOB$	Initial [Fe] at oxide-bulk interface	g/cm^3	1.14^{-8}
$CSatPO$	Initial Fe sol'b at oxide-passivating interface	g/cm^3	3.97^{-8}
$CeOP$	Initial [Fe] at oxide-passivating interface	g/cm^3	3.9^{-8}
$CSatMP$	Initial Fe sol'b at metal-passivating interface	g/cm^3	2.93^{-8}
$CeMP$	Initial [Fe] at metal-passivating interface	g/cm^3	2.44^{-8}
U	Linear velocity of coolant	cm/s	663.15
kd	Dissolution rate constant of magnetite	cm/s	0.02
km	Mass transfer coefficient	cm/s	0.352
ksp	Spalling time constant	–	395
kCR	Chromium content constant	–	1
$Temperature$	Temperature	$^\circ C$	140
$Tkelvin$	Temperature	K	413.15
$DP0$	Diffusivity of iron in passivating layer	cm^2/s	1.065^{-4}
$DFe0$	Diffusivity of Iron in Water	cm^2/s	1.065^{-4}
$f0$	Surface area factor	–	1.73205
$S0$	Supersaturation factor	–	1.1
$DeltaP0$	Passivating layer thickness	g/cm^2	9.78^{-6}
$ChiPO$	Tortuosity of passivating layer	–	1.8
$PhiPO$	Porosity of passivating layer	–	0.2
$RhoPO$	Density of passivating layer	g/cm^3	5.15
$MP0$	Mass fraction of iron in passivating layer	–	1
$RhoH2O0$	Density of Water	g/cm^3	0.86845
$MFe0$	Mass fraction of iron in oxide	–	0.723569
$RhoFe0$	Density of iron	g/cm^3	7.9
$RhoSteel0$	Density of steel	g/cm^3	7.86
$PhiOX0$	Porosity of oxide layer	–	0.09
$ChiOX0$	Tortuosity of oxide	–	2
$RhoOX0$	Density of oxide	g/cm^3	5.2
$DCORs0$	Initial concentration at oxide bulk	g/cm^3	0
$DOXs0$	Initial oxide layer thickness	g/cm^2	1.20^{-5}

Parameter	Description	Unit	Value
$t0$	Time interval for simulation	s	1000
$tstep0$	Number of steps in model run	–	7000
$Paverage0$	Minimum size of oxide particle	cm	1^{-6}
$SDP0$	Maximum size of oxide particle	cm	1^{-5}
$CrContent0$	Chromium content of pipe material	%	0.019
FF	Friction Factor ($f = 0.316Re^{-0.25}$)	–	0.0237
$CH2Coolant0$	Bulk concentration of hydrogen	cm^3/kg	0
$CorrRateExp0$	Experimental corrosion rate	$\mu m/yr$	2750
$iH2_HpOB0$	Current at the oxide-solution interfact	A	1.18^{-12}
$EmixedInitial0$	Initial estimate of mixed potential	V	-0.5
0	Number of electrons transferred	–	2
$F0$	Faraday Constant	C/mol	96485
$R0$	Gas Constant	$J/mol * K$	8.314
$h0$	Planck's Constant	$J * s$	6.63^{-34}
$kboltzman0$	Boltzman Constant	J/K	1.38^{-23}
$Beta0$	Symmetry Factor	–	0.5
$FeMMass0$	$Fe(OH)^2$molar mass	g/mol	90
$H2MMass0$	H_2molar mass	g/mol	2.016
$Ecorrinitial$	Experimental corrosion potential	V	-0.55
$ActEFe_Fe2_MP$	Activation Energy	J/mol	180600
$ActEH2_Hp_MP$	Activation Energy	J/mol	160000
$ActEH2_HpOB$	Activation Energy	J/mol	215000
$ActEFe2p_Fe3O4_OB$	Activation Energy	J/mol	208000
$ActEFe2p_Fe3O4_OP$	Activation Energy	J/mol	173000
$ActEH2_HpOP$	Activation Energy	J/mol	177000
pH	pH at temperature	–	6.88
MU	Dynamic viscosity	cP	0.1995
$probedia$	Probe internal diameter	cm	0.16

B.12 Neutral Chemistry, 140°C, 1.5 LPM, No Iron Source, 1.6 mm probe

Parameter	Unit	Predicted Value
FAC Rate	mm/yr	2.107
Oxide Thickness	μm	0.323
Mixed Potential	V	-0.325

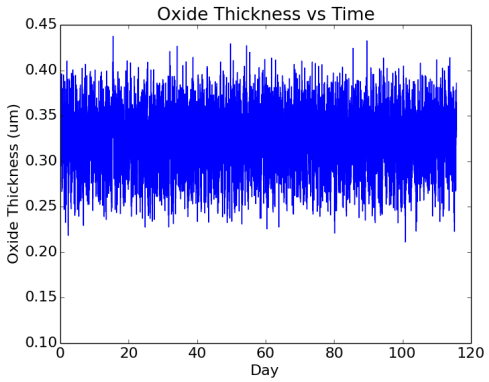

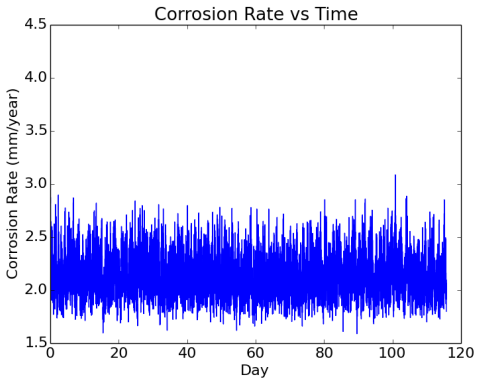

Parameter	Description	Unit	Value
CB	Initial [Fe] in bulk coolant	g/cm^3	1.64^{-9}
$CSatOB$	Initial Fe sol'b at oxide-bulk interface	g/cm^3	1.16^{-7}
$CeOB$	Initial [Fe] at oxide-bulk interface	g/cm^3	1.02^{-7}
$CSatPO$	Initial Fe sol'b at oxide-passivating interface	g/cm^3	3.54^{-7}
$CeOP$	Initial [Fe] at oxide-passivating interface	g/cm^3	3.48^{-7}
$CSatMP$	Initial Fe sol'b at metal-passivating interface	g/cm^3	2.61^{-7}
$CeMP$	Initial [Fe] at metal-passivating interface	g/cm^3	2.18^{-7}
U	Linear velocity of coolant	cm/s	1240
kd	Dissolution rate constant of magnetite	cm/s	0.15
km	Mass transfer coefficient	cm/s	0.636
ksp	Spalling time constant	–	458
kCR	Chromium content constant	–	1
$Temperature$	Temperature	$^\circ C$	140
$Tkelvin$	Temperature	K	413.15
$DP0$	Diffusivity of iron in passivating layer	cm^2/s	1.065^{-4}
$DFe0$	Diffusivity of Iron in Water	cm^2/s	1.065^{-4}
$f0$	Surface area factor	–	1.73205
$S0$	Supersaturation factor	–	1.1
$DeltaP0$	Passivating layer thickness	g/cm^2	9.78^{-6}
$ChiPO$	Tortuosity of passivating layer	–	1.8
$PhiPO$	Porosity of passivating layer	–	0.2
$RhoPO$	Density of passivating layer	g/cm^3	5.15
$MP0$	Mass fraction of iron in passivating layer	–	1
$RhoH2O0$	Density of Water	g/cm^3	0.86845
$MFe0$	Mass fraction of iron in oxide	–	0.723569
$RhoFe0$	Density of iron	g/cm^3	7.9
$RhoSteel0$	Density of steel	g/cm^3	7.86
$PhiOX0$	Porosity of oxide layer	–	0.09
$ChiOX0$	Tortuosity of oxide	–	2
$RhoOX0$	Density of oxide	g/cm^3	5.2
$DCORs0$	Initial concentration at oxide bulk	g/cm^3	0
$DOXs0$	Initial oxide layer thickness	g/cm^2	1.20^{-5}

Parameter	Description	Unit	Value
$t0$	Time interval for simulation	s	1000
$tstep0$	Number of steps in model run	–	7000
$Paverage0$	Minimum size of oxide particle	cm	1^{-6}
$SDP0$	Maximum size of oxide particle	cm	1^{-5}
$CrContent0$	Chromium content of pipe material	%	0.019
FF	Friction Factor ($f = 0.316Re^{-0.25}$)	–	0.0237
$CH2Coolant0$	Bulk concentration of hydrogen	cm^3/kg	0
$CorrRateExp0$	Experimental corrosion rate	$\mu m/yr$	875
$iH2_HpOB0$	Current at the oxide-solution interfact	A	1.18^{-12}
$EmixedInitial0$	Initial estimate of mixed potential	V	-0.5
0	Number of electrons transferred	–	2
$F0$	Faraday Constant	C/mol	96485
$R0$	Gas Constant	$J/mol * K$	8.314
$h0$	Planck's Constant	$J * s$	6.63^{-34}
$kboltzman0$	Boltzman Constant	J/K	1.38^{-23}
$Beta0$	Symmetry Factor	–	0.5
$FeMMass0$	$Fe(OH)^2$molar mass	g/mol	90
$H2MMass0$	H_2molar mass	g/mol	2.016
$Ecorrinitial$	Experimental corrosion potential	V	-0.55
$ActEFe_Fe2_MP$	Activation Energy	J/mol	180600
$ActEH2_Hp_MP$	Activation Energy	J/mol	160000
$ActEH2_HpOB$	Activation Energy	J/mol	215000
$ActEFe2p_Fe3O4_OB$	Activation Energy	J/mol	208000
$ActEFe2p_Fe3O4_OP$	Activation Energy	J/mol	173000
$ActEH2_HpOP$	Activation Energy	J/mol	177000
pH	pH at temperature	–	5.88
MU	Dynamic viscosity	cP	0.1955
$probedia$	Probe internal diameter	cm	0.16

B.13 Neutral Chemistry, 140°C, 1.65 LPM, No Iron Source, 2.4 mm probe

Parameter	Unit	Predicted Value
FAC Rate	mm/yr	0.844
Oxide Thickness	μm	0.476
Mixed Potential	V	-0.363

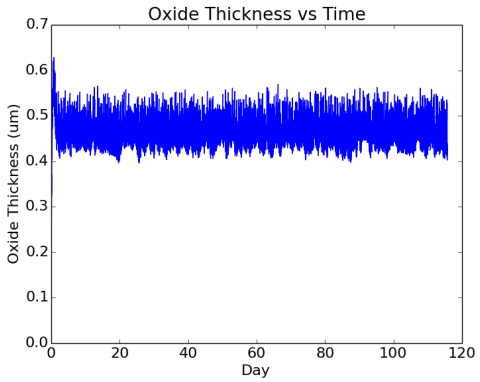

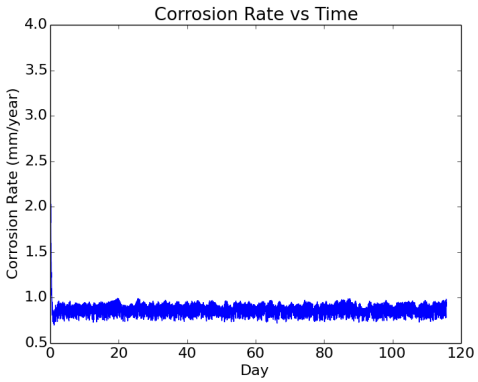

Parameter	Description	Unit	Value
CB	Initial [Fe] in bulk coolant	g/cm^3	1.64^{-9}
$CSatOB$	Initial Fe sol'b at oxide-bulk interface	g/cm^3	1.16^{-7}
$CeOB$	Initial [Fe] at oxide-bulk interface	g/cm^3	1.02^{-7}
$CSatPO$	Initial Fe sol'b at oxide-passivating interface	g/cm^3	3.54^{-7}
$CeOP$	Initial [Fe] at oxide-passivating interface	g/cm^3	3.48^{-7}
$CSatMP$	Initial Fe sol'b at metal-passivating interface	g/cm^3	2.61^{-7}
$CeMP$	Initial [Fe] at metal-passivating interface	g/cm^3	2.18^{-7}
U	Linear velocity of coolant	cm/s	610
kd	Dissolution rate constant of magnetite	cm/s	0.15
km	Mass transfer coefficient	cm/s	0.329
ksp	Spalling time constant	–	1300
kCR	Chromium content constant	–	1
$Temperature$	Temperature	$^{\circ}C$	140
$Tkelvin$	Temperature	K	413.15
$DP0$	Diffusivity of iron in passivating layer	cm^2/s	1.065^{-4}
$DFe0$	Diffusivity of Iron in Water	cm^2/s	1.065^{-4}
$f0$	Surface area factor	–	1.73205
$S0$	Supersaturation factor	–	1.1
$DeltaP0$	Passivating layer thickness	g/cm^2	9.78^{-6}
$ChiPO$	Tortuosity of passivating layer	–	1.8
$PhiPO$	Porosity of passivating layer	–	0.2
$RhoPO$	Density of passivating layer	g/cm^3	5.15
$MP0$	Mass fraction of iron in passivating layer	–	1
$RhoH2O0$	Density of Water	g/cm^3	0.86845
$MFe0$	Mass fraction of iron in oxide	–	0.723569
$RhoFe0$	Density of iron	g/cm^3	7.9
$RhoSteel0$	Density of steel	g/cm^3	7.86
$PhiOX0$	Porosity of oxide layer	–	0.09
$ChiOX0$	Tortuosity of oxide	–	2
$RhoOX0$	Density of oxide	g/cm^3	5.2
$DCORs0$	Initial concentration at oxide bulk	g/cm^3	0
$DOXs0$	Initial oxide layer thickness	g/cm^2	1.20^{-5}

Parameter	Description	Unit	Value
$t0$	Time interval for simulation	s	1000
$tstep0$	Number of steps in model run	–	7000
$Paverage0$	Minimum size of oxide particle	cm	1^{-6}
$SDP0$	Maximum size of oxide particle	cm	1^{-5}
$CrContent0$	Chromium content of pipe material	%	0.019
FF	Friction Factor ($f = 0.316Re^{-0.25}$)	–	0.0237
$CH2Coolant0$	Bulk concentration of hydrogen	cm^3/kg	0
$CorrRateExp0$	Experimental corrosion rate	$\mu m/yr$	875
$iH2_HpOB0$	Current at the oxide-solution interfact	A	1.18^{-12}
$EmixedInitial0$	Initial estimate of mixed potential	V	-0.5
0	Number of electrons transferred	–	2
$F0$	Faraday Constant	C/mol	96485
$R0$	Gas Constant	$J/mol * K$	8.314
$h0$	Planck's Constant	$J * s$	6.63^{-34}
$kboltzman0$	Boltzman Constant	J/K	1.38^{-23}
$Beta0$	Symmetry Factor	–	0.5
$FeMMass0$	$Fe(OH)^2$molar mass	g/mol	90
$H2MMass0$	H_2molar mass	g/mol	2.016
$Ecorrinitial$	Experimental corrosion potential	V	-0.55
$ActEFe_Fe2_MP$	Activation Energy	J/mol	180600
$ActEH2_Hp_MP$	Activation Energy	J/mol	160000
$ActEH2_Hp_OB$	Activation Energy	J/mol	215000
$ActEFe2p_Fe3O4_OB$	Activation Energy	J/mol	208000
$ActEFe2p_Fe3O4_OP$	Activation Energy	J/mol	173000
$ActEH2_Hp_OP$	Activation Energy	J/mol	177000
pH	pH at temperature	–	5.88
MU	Dynamic viscosity	cP	0.1955
$probedia$	Probe internal diameter	cm	0.24

B.14 Neutral Chemistry, 140°C, 1.2 LPM, No Iron Source, 3.2 mm probe

Parameter	Unit	Predicted Value
FAC Rate	mm/yr	0.432
Oxide Thickness	μm	0.561
Mixed Potential	V	-0.385

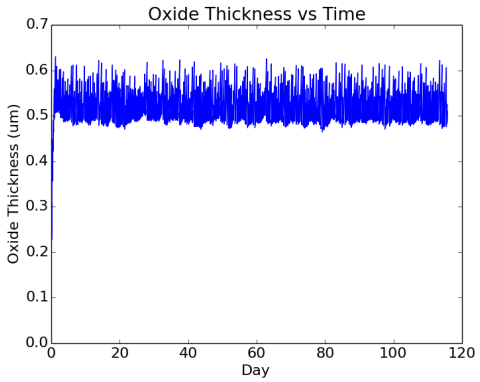

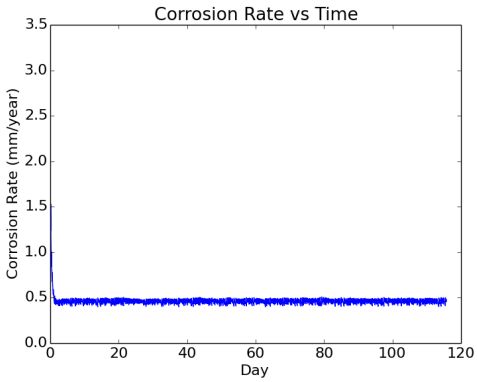

Parameter	Description	Unit	Value
CB	Initial [Fe] in bulk coolant	g/cm^3	1.64^{-9}
$CSatOB$	Initial Fe sol'b at oxide-bulk interface	g/cm^3	1.16^{-7}
$CeOB$	Initial [Fe] at oxide-bulk interface	g/cm^3	1.02^{-7}
$CSatPO$	Initial Fe sol'b at oxide-passivating interface	g/cm^3	3.54^{-7}
$CeOP$	Initial [Fe] at oxide-passivating interface	g/cm^3	3.48^{-7}
$CSatMP$	Initial Fe sol'b at metal-passivating interface	g/cm^3	2.61^{-7}
$CeMP$	Initial [Fe] at metal-passivating interface	g/cm^3	2.18^{-7}
U	Linear velocity of coolant	cm/s	250
kd	Dissolution rate constant of magnetite	cm/s	0.15
km	Mass transfer coefficient	cm/s	0.145
ksp	Spalling time constant	–	2035
kCR	Chromium content constant	–	1
$Temperature$	Temperature	$^\circ C$	140
$Tkelvin$	Temperature	K	413.15
$DP0$	Diffusivity of iron in passivating layer	cm^2/s	1.065^{-4}
$DFe0$	Diffusivity of Iron in Water	cm^2/s	1.065^{-4}
$f0$	Surface area factor	–	1.73205
$S0$	Supersaturation factor	–	1.1
$DeltaP0$	Passivating layer thickness	g/cm^2	9.78^{-6}
$ChiPO$	Tortuosity of passivating layer	–	1.8
$PhiPO$	Porosity of passivating layer	–	0.2
$RhoPO$	Density of passivating layer	g/cm^3	5.15
$MP0$	Mass fraction of iron in passivating layer	–	1
$RhoH2O0$	Density of Water	g/cm^3	0.86845
$MFe0$	Mass fraction of iron in oxide	–	0.723569
$RhoFe0$	Density of iron	g/cm^3	7.9
$RhoSteel0$	Density of steel	g/cm^3	7.86
$PhiOX0$	Porosity of oxide layer	–	0.09
$ChiOX0$	Tortuosity of oxide	–	2
$RhoOX0$	Density of oxide	g/cm^3	5.2
$DCORs0$	Initial concentration at oxide bulk	g/cm^3	0
$DOXs0$	Initial oxide layer thickness	g/cm^2	1.20^{-5}

Parameter	Description	Unit	Value
$t0$	Time interval for simulation	s	1000
$tstep0$	Number of steps in model run	–	7000
$Paverage0$	Minimum size of oxide particle	cm	1^{-6}
$SDP0$	Maximum size of oxide particle	cm	1^{-5}
$CrContent0$	Chromium content of pipe material	%	0.019
FF	Friction Factor ($f = 0.316Re^{-0.25}$)	–	0.0237
$CH2Coolant0$	Bulk concentration of hydrogen	cm^3/kg	0
$CorrRateExp0$	Experimental corrosion rate	$\mu m/yr$	875
$iH2_HpOB0$	Current at the oxide-solution interfact	A	1.18^{-12}
$EmixedInitial0$	Initial estimate of mixed potential	V	-0.5
0	Number of electrons transferred	–	2
$F0$	Faraday Constant	C/mol	96485
$R0$	Gas Constant	$J/mol * K$	8.314
$h0$	Planck's Constant	$J * s$	6.63^{-34}
$kboltzman0$	Boltzman Constant	J/K	1.38^{-23}
$Beta0$	Symmetry Factor	–	0.5
$FeMMass0$	$Fe(OH)^2$molar mass	g/mol	90
$H2MMass0$	H_2molar mass	g/mol	2.016
$Ecorrinitial$	Experimental corrosion potential	V	-0.55
$ActEFe_Fe2_MP$	Activation Energy	J/mol	180600
$ActEH2_Hp_MP$	Activation Energy	J/mol	160000
$ActEH2_HpOB$	Activation Energy	J/mol	215000
$ActEFe2p_Fe3O4_OB$	Activation Energy	J/mol	208000
$ActEFe2p_Fe3O4_OP$	Activation Energy	J/mol	173000
$ActEH2_HpOP$	Activation Energy	J/mol	177000
pH	pH at temperature	–	5.88
MU	Dynamic viscosity	cP	0.1955
$probedia$	Probe internal diameter	cm	0.32

Appendix C

Appendix C - Parametric Study of EPRI Fossil FAC Advisor

The following plots present the results of a parametric study conducted to gauge the response of EPRI's Fossil FAC Advisor (FFA) software package to single variable changes. EPRI technical personnel constructed a database within the FFA system to simulate the CNER Loop 1 facility so that corresponding experimental results from this research program could be directly compared to the outputs from the FFA software.

Without access to the underlying algorithms of the software package, it is difficult to ascertain exactly what the software is doing with each input variable. In general, the software does tend to provide an overall trend that would be expected based on the variable changes imposed.

For example, in Figure C.1, as one would expect, the FAC increases as flow rate increases. The magnitude of the FAC calculated by the FFA software is several times higher than our experimental values, but the software also was not benchmarked against measured data, which is normally required for it's use.

The model response to oxygen concentration is more suspect, as there appears to be a threshold value at around 10 ppb, below which there is no effect of oxygen concentration on FAC rates. At the conditions modeled in Figure C.2, FAC would have stifled long before reaching 10 ppb of oxygen.

The model response to temperature is of particular concern. As can be seen in Figure C.3, the FAC rate increases for a period around 180°C. This does

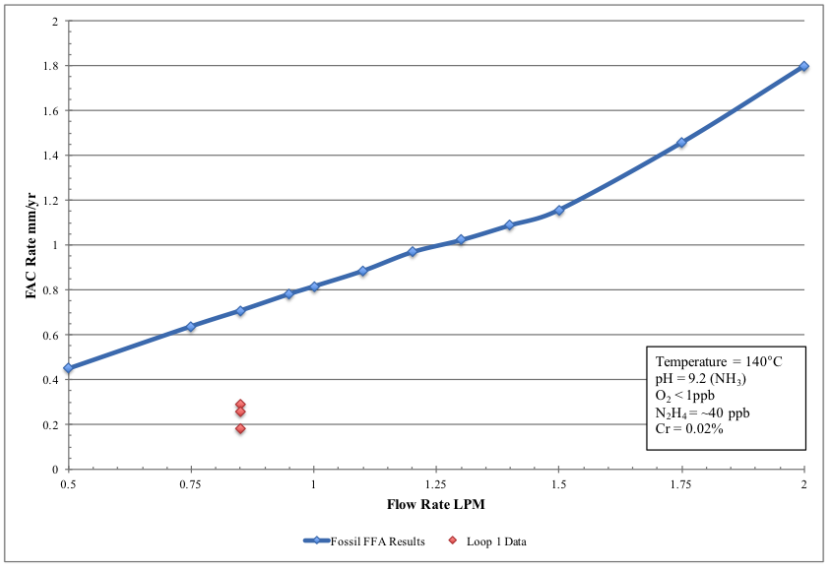

Figure C.1: Variation of FAC rate with changes in flow rate

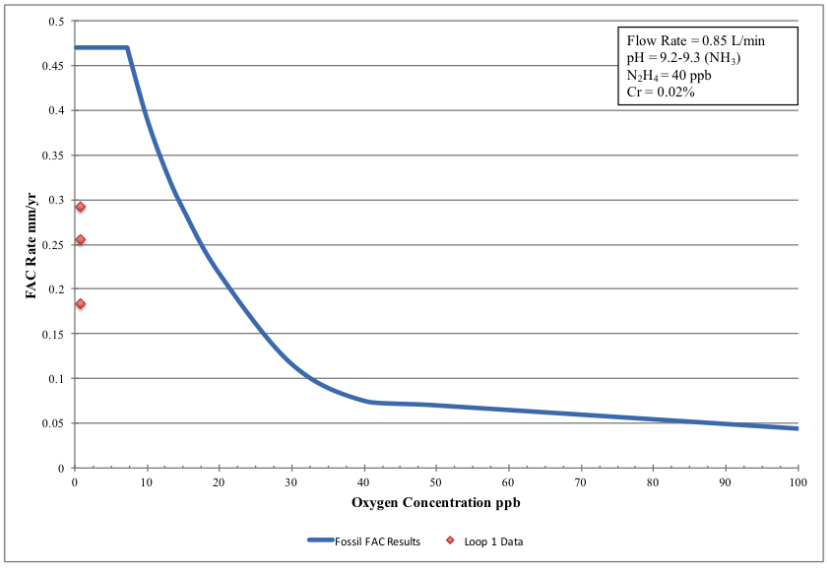

Figure C.2: Variation of FAC rate with changes in $[O_2]$

not happen, and was confirmed by experiment in Loop 1, the result of which is plotted on Figure C.3. It was unclear if this is a result of some issue with the particular model of Loop 1 used, or if this is a systematic problem with the FFA package.

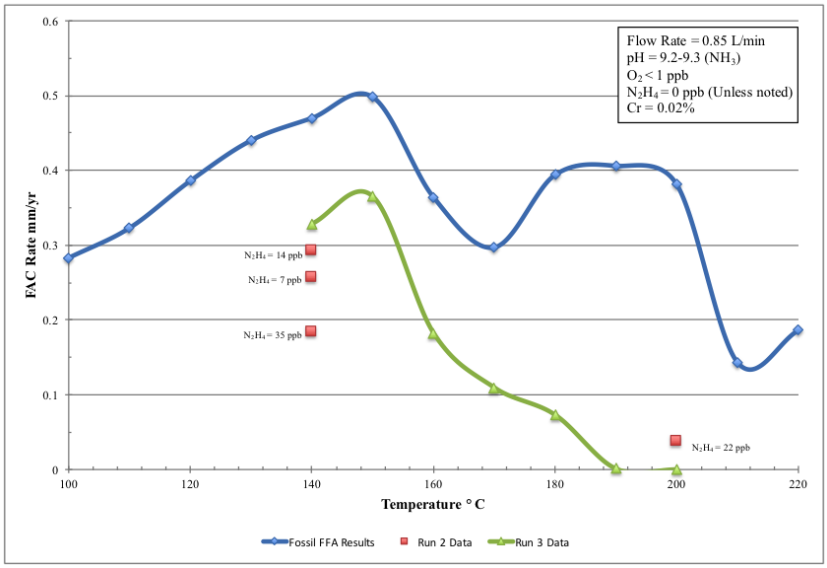

Figure C.3: Variation of FAC rate with changes in temperature

Figure C.4 would indicate that the model responds as would be expected to coolant pH changes, and does predict the magnitude of FAC reasonably well at $pH_{25°C}$ 9.2.

EPRI literature [28] indicates that FFA applies a modified Ducreux correlation to account for chromium content of the steel. The Ducreux correlation places a threshold value for chromium at 0.04%, below which there is said to be no effect on FAC rate, and above which the FAC rate decreases linearly

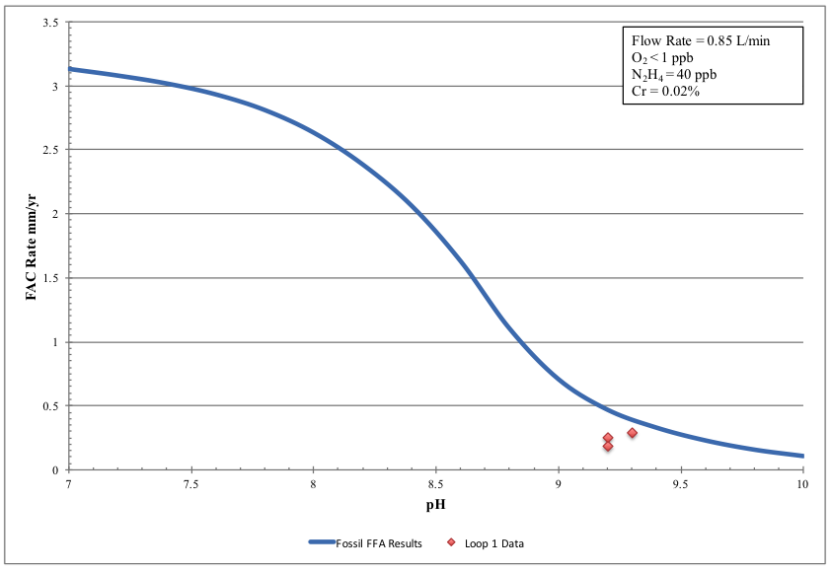

Figure C.4: Variation of FAC rate with changes in $pH^{25^\circ C}$

with chromium content. The experimental work at UNB was completed with chromium contents well below the Durcreux threshold value, so FFA would be unable to reliably predict actual rates.

Curiously, FFA does not appear to account for hydrazine concentration in the coolant, at least not in the response provided in Figure C.6.

Without any indication of what the algorithms are actually doing, and how the individual variables interact within the program (for example, why does the program reasonably predict the magnitude when varying pH, but not at the same pH when varying flow rate?), it is difficult to speculate further on the abilities of the FFA to make FAC rate predictions.

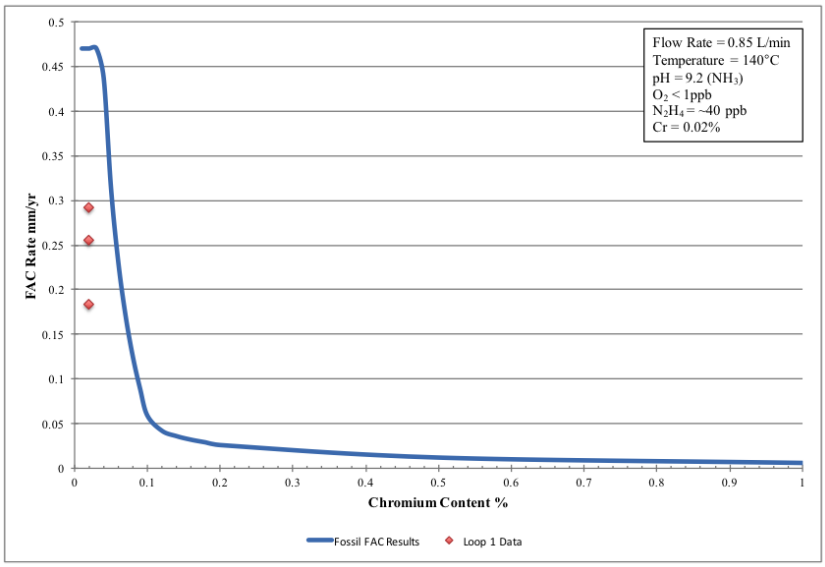

Figure C.5: Variation of FAC rate with changes in chromium content of the steel

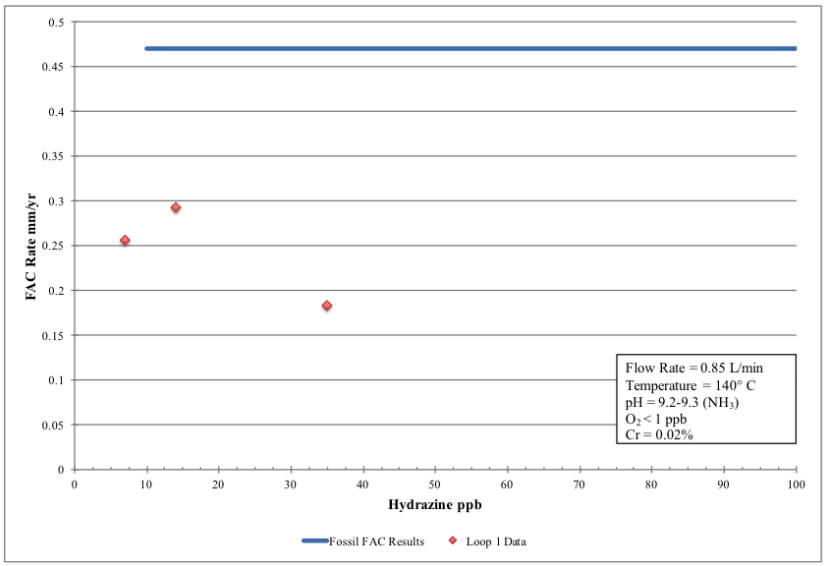

Figure C.6: Variation of FAC rate with changes to $[N_2H_4]$

Vita

Full Name: Michael Alexander Briggs

University of New Brunswick Master of Science in Civil Engineering, 2006

University of New Brunswick Bachelor of Science in Civil Engineering, 2002

Publications:

Development of Tools for Controlling Flow-Accelerated Corrosion, Technical Report, Electric Power Research Institute, December 2015

Behavior of Fibre Reinforced Concrete Beams on Grade, International Journal of Physical Modelling in Geotechnics, (Accepted for publication, 2015)

Conference Presentations:

Mechanistic Modelling of Flow-Accelerated Corrosion, 11th International Conference on Cycle Chemistry in Fossil and Combined Cycle Plants with HRSG, July 2015, St. Louis

Bucking the Trend: Mechanistic Modelling of FAC at UNB Nuclear, CANDU Owners Group (COG) Workshop on FAC, Toronto, December 2013